Search for top-squark pair production with the LHC experiment ATLAS in final states with *b*-quarks and tau leptons

Dissertation der Fakultät für Physik
der
Ludwig-Maximilians-Universität München

vorgelegt von
Balthasar Maria Schachtner
geboren in Gräfelfing

München, den 14. Februar 2018

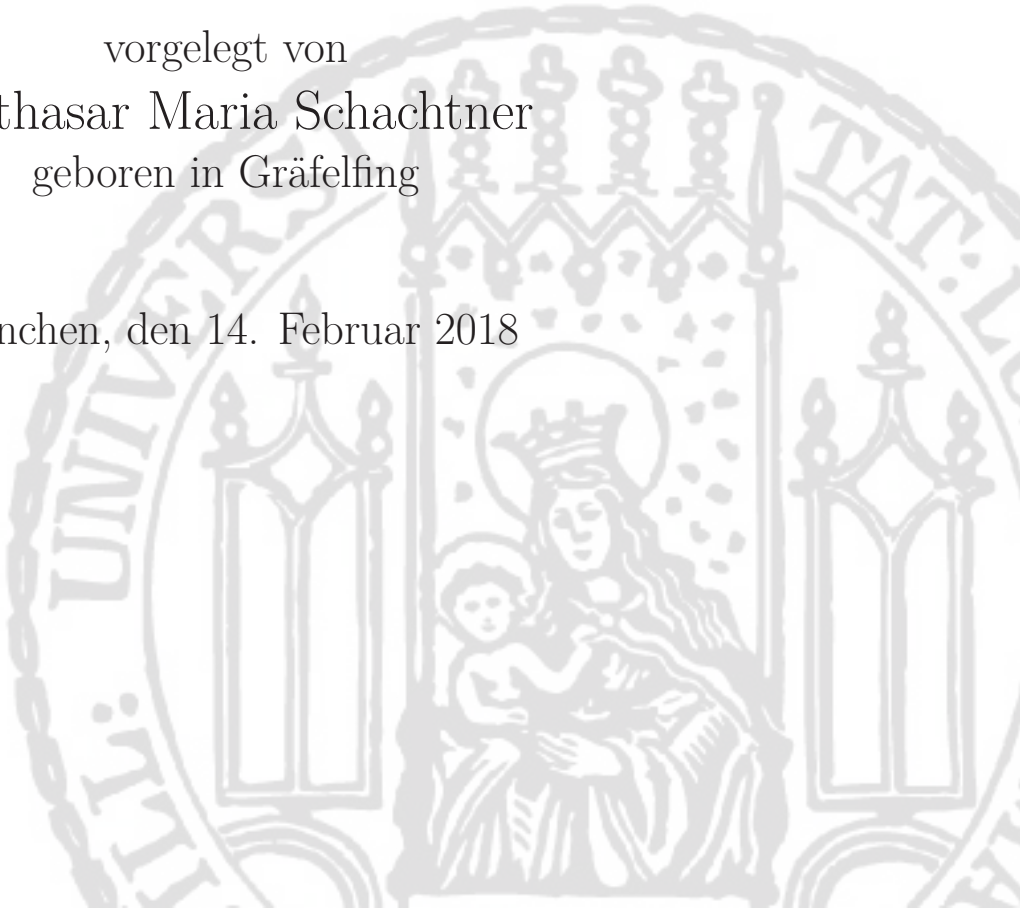

Erstgutachterin: Prof. Dr. Dorothee Schaile
Zweitgutachter: Prof. Dr. Thomas Kuhr
Tag der mündlichen Prüfung: 6. April 2018

Zusammenfassung

Eine Suche nach Supersymmetrie in Endzuständen mit zwei b-Quarks, zwei Tau-Leptonen und schwach wechselwirkenden Teilchen wird vorgestellt. Dazu wird ein Signalmodell mit direkter Produktion eines Top-Squark-Paares, das in Tau-Sleptonen zerfällt, angenommen. Proton–Proton-Kollisionen des Large Hadron Colliders werden in den Jahren 2015 und 2016 bei einer Schwerpunktsenergie von 13 TeV mit dem ATLAS-Experiment aufgezeichnet. Der Datensatz hat eine integrierte Luminosität von 36,1 fb^{-1}.

In Abhängigkeit des Zerfallsmodus des Tau-Leptons werden zwei Kanäle für die Suche definiert: der gemischte Kanal, in dem eines der Tau-Leptonen leptonisch und das andere hadronisch zerfällt, und der hadronische Kanal, in dem beide Tau-Leptonen hadronisch zerfallen. Für die Normierung des Prozesses der Top-Quark-Paarproduktion werden Kontrollregionen entworfen und dazugehörige Validierungsregionen definiert. Dedizierte Kontrollregionen werden für die nachrangigen Prozesse von Paarproduktion massebehafteter Vektorbosonen und Paarproduktion von Top-Quarks in Verbindung mit Z-Bosonen entwickelt.

In keinem der Kanäle wird ein signifikanter Überschuss gegenüber der Erwartung im Rahmen des Standardmodells der Teilchenphysik festgestellt, daher werden Ausschlussgrenzen mithilfe der CL_s-Methodik bestimmt. Auf einem Konfidenzniveau von 95 % können Massen des Top-Squarks (Tau-Sleptons) von bis zu 1,16 TeV (1,00 TeV) ausgeschlossen werden.

Abstract

A search for supersymmetry in final states with two b-quarks, two tau leptons and weakly-interacting particles is presented. The signal model assumes direct production of top-squark pairs decaying to tau sleptons. Proton–proton collisions provided by the Large Hadron Collider in the years 2015 and 2016 at 13 TeV centre-of-mass energy are recorded with the ATLAS experiment. The integrated luminosity of the dataset amounts to 36.1 fb^{-1}.

Depending on the decay of the tau leptons, two search channels are defined: the mixed channel, where one tau lepton decays hadronically and the other one leptonically, and the hadronic channel, where both tau leptons decay hadronically. Control regions to constrain the normalisation of the top-quark pair-production process are designed and corresponding validation regions defined. For the subleading processes of pair production of massive vector bosons and of the top-quark pair production with an associated Z boson, dedicated control regions are developed.

No significant excess over the event yields expected from the Standard Model of particle physics is observed in either of the channels, therefore exclusion limits using the CL_s prescription are set. For the top squark (tau slepton), masses up to 1.16 TeV (1.00 TeV) can be excluded at 95 % confidence level.

Contents

1. Introduction

Elementary particle physics is on the verge of an exciting turning point. On the one hand, the spotlight is undoubtedly on the Standard Model (SM) of particle physics. The mathematical structure of the SM has provided a framework to put the discoveries at high-energy particle-physics experiments into a coherent picture for over half a century. On the other hand, astrophysical and cosmological observations exert increasing pressure on the SM. The observation of dark matter is one of the most compelling arguments which appears to limit the validity of the SM to the energy regimes accessible by current accelerator experiments.

To put this into context, the SM is an incredibly precise and predictive theory. The discovery of the Higgs boson in 2012 marks the completion of the SM, which in itself was a big success. Until today, all measured properties of the Higgs boson match the predictions by the SM, making an even stronger case for the SM. Yet, there is no candidate particle for dark matter in the SM. The high predictivity of the SM provides an outstanding opportunity to search for new physics phenomena not included in the SM and to understand how the astrophysical observations can be reconciled with the observations from accelerator experiments.

Until now, dark matter only manifested itself in observations via its gravitational interaction. The nature of dark matter is thus not well-known and experiments are needed to provide additional evidence. From underground experiments which try to spot rare weak interactions of the dark-matter particles with the detector material, to scans of the sky for gamma rays from dark matter annihilation, to searches for exotic particles like axions which could be potential dark matter candidates, the efforts to understand the nature of dark matter are spread over a wide range of unique approaches.

The analysis presented in the following has to be understood as part of the effort trying to find physics phenomena which go beyond the phenomena described by the SM. While there are many complementary approaches to search for these, pushing the energy frontier is a very promising one. Thanks to concerted international efforts united in the organisation of CERN, the circular Large Hadron Collider (LHC) provides proton–proton collisions at a current maximum centre-of-mass energy of 13 TeV — an unprecedented energy. Data collected with the ATLAS experiment from these collisions in the years 2015 and 2016 is analysed in the following.

There is a plethora of theories for models of new physics beyond the SM. A very elegant subclass of these models arise from the framework of Supersymmetry (SUSY). These models are a logical extension of the framework of the SM and are able to solve a number of its shortcomings. Among other new features, realistic supersymmetric models usually contain a dark-matter candidate. On the downside, SUSY introduces many additional parameters. Even though there are external constraints on these parameters, there is still a huge set of viable models and different signatures. For many of them it is not clear which values of the parameters are preferred. Therefore, in this analysis

the hybrid approach of simplified models is employed, searching for a unique final state inspired by a certain class of SUSY models.

This analysis focuses on a particularly rich final state, which includes b-quarks, tau leptons, and particles invisible to the detector. Only one preceding analysis targeting this signal model was carried out at a centre-of-mass energy of 8 TeV [1]. Two sets of preliminary results have been made public in the context of the analysis presented here [2, 3], and the final results will be submitted to Physical Review D.

The thesis is structured as follows: Key concepts of the theoretical frameworks are illustrated and the signal model considered in this analysis is introduced. An overview over the LHC and the relevant physics processes at high-energy proton–proton collisions is given. Hereafter, the ATLAS detector and the reconstruction of physics objects is elaborated on. Finally, the analysis itself is described, describing the necessary ingredients and illustrating the results. The thesis concludes with a discussion of the results and an outlook.

In the following, "natural units" are adopted. The speed of light c and the reduced Planck constant $\hbar$ are set to 1 and can be re-introduced at any point.

2. Theory Background

This chapter illustrates the basic concepts, motivations, and shortcomings of the SM of particle physics and its popular extension with SUSY. These serve as a basis for the following discussion of the signal model considered and at the end of the chapter complementary searches are shown. This chapter is not meant to be a complete description of the mathematical formalism, but to highlight the important relations and consequences. The mathematical formulation for the SM follows [4] and follows [5] for the theory of SUSY.

Even if the presented search explores if SUSY is realised in nature, it has to be kept in mind that the SM is very well confirmed by current high energy experiments (including data of Run 1 of the LHC). The expected signals in the accessible energy range are relatively small and precise knowledge of the SM is necessary in order to find deviations from the SM.

2.1. Standard Model

The Standard Model of particle physics is a theoretical framework providing a precise and predictive description of the interactions of elementary particles. It has been tested and confirmed to high precision up to the electroweak (EWK) scale at the Large Electron-Positron Collider (LEP). There is a number of awards connected to the SM, showing its great success in predicting and explaining the fundamental interactions. For example, Feynman, Schwinger, and Tomonaga were awarded in 1964 with the Nobel Prize in physics for the development of Quantum Electrodynamics (QED). This quantum field theory convincingly allows calculating fundamental processes such as the measurement of the anomaly of the magnetic moment of the electron to a precision matching to the relative measurement uncertainty of 2.4×10^{-10} [6]. In 1979, the Nobel Prize committee awarded Glashow, Salam, and Weinberg for their work leading to an understanding of the electroweak unification, one of the cornerstones of the SM. Finally, the completion of the SM with the discovery of the Higgs boson led to the Nobel Prize for Englert and Higgs in the year 2013.

It is therefore worth to have a look at the now completed SM in order to understand its phenomenology and to provide a basis for the discussion of the background processes. The known shortcomings of the SM are discussed to give the motivation of SUSY.

2.1.1. Mathematical Description

Formally the SM can be described by a Lagrangian density which can be constructed from symmetry groups, potentials and couplings getting their input from observations. The rules of quantum field theories then yield the appropriate equations from which all kinematics and interactions of elementary particles can be derived.

The action of a Lagrangian in a local quantum field theory can be written as [4]

$$S = \int \mathcal{L}(\phi, \partial_\mu \phi) \mathrm{d}^4 x, \tag{2.1}$$

where $\mathcal{L}$ denotes the Lagrangian (density) and ϕ is one or more fields. Using the principle of least action the Euler-Lagrange equations of motions can be derived as

$$\partial_\mu \left(\frac{\partial \mathcal{L}}{\partial(\partial_\mu \phi)} \right) - \frac{\partial \mathcal{L}}{\partial \phi} = 0, \tag{2.2}$$

containing the evolution of the fields ϕ. The formulation as quantum field theory ensures that the concepts of special relativity are respected.

Symmetries are an essential ingredient in the formulation of the SM. It was famously shown by Noether that for every symmetry there is a conservation law connected to it (cf. e.g. [7]). In classical physics this connects e.g. the invariance of the laws of physics under time translations with energy conservation or the invariance under spatial translations with momentum conversation. But also so-called internal symmetries can give rise to conserved quantities. In QED the invariance of the Lagrangian under phase rotations of the fields gives rise to the conservation of the electric charge. The complete SM can be described by this combination of gauge groups

$$\mathrm{SU}(3)_\mathrm{C} \otimes \mathrm{SU}(2)_\mathrm{L} \otimes \mathrm{U}(1)_\mathrm{Y}, \tag{2.3}$$

where $\mathrm{U}(n)$ ($\mathrm{SU}(n)$) describes (special) unitary groups, i.e. all unitary matrices with dimension $n \times n$ (and a determinant of 1, if special). The implications of the symmetry group chosen will be highlighted in the following sections.

The concept introducing quantum behaviour into the field theory is the promotion of classical fields to quantum fields (historically called the second quantisation). Commutation (anti-commutation) relations are imposed on the fields, such that the excitations of the fields fulfil Bose-Einstein (Fermi-Dirac) statistics. Any quantum field theory automatically contains antiparticles, which have opposite charge-like quantum numbers and can also be interpreted as particles evolving backwards in time. Particles without charge-like quantum numbers are their own antiparticles. In the following the antiparticles are only mentioned explicitly where necessary, otherwise they are silently assumed to be included.

The fermionic fields of the SM Lagrangian are postulated and are motivated from observations. The fermions themselves comprise two major groups (called families): the quarks, which are coloured and charged with respect to $\mathrm{SU}(2)_\mathrm{L} \otimes \mathrm{U}(1)_\mathrm{Y}$ and the leptons, colour-neutral and only charged with respect to $\mathrm{SU}(2)_\mathrm{L} \otimes \mathrm{U}(1)_\mathrm{Y}$. Each of the families has three generations, the second and third generation are heavier copies of the first generation with identical quantum numbers.

For the first generation, quark fields an electroweak $\mathrm{SU}(2)_\mathrm{L}$-doublet

$$Q_L = \begin{pmatrix} u \\ d \end{pmatrix}_L$$

in the fundamental representation of $\mathrm{SU}(3)_\mathrm{C}$ is introduced. The fields in the doublet can be identified with the left-handed u- and d-quark. For the corresponding right-handed

Table 2.1.: Overview of the quark fields and masses in the SM. Masses are taken from [8]. Due to the confinement of quarks, only the top-quark has a directly measured mass. For c- and b-quark the $\overline{\text{MS}}$-mass is quoted, while for the lighter quarks current-quark masses are given.

$\begin{pmatrix} u \\ d \end{pmatrix}_L$	u_R	d_R	$m_u = 2.2$ MeV $m_d = 4.7$ MeV
$\begin{pmatrix} c \\ s \end{pmatrix}_L$	c_R	s_R	$m_c = 1.28$ GeV $m_s = 96$ MeV
$\begin{pmatrix} t \\ b \end{pmatrix}_L$	t_R	b_R	$m_t = 173.1$ GeV $m_b = 4.17$ GeV

Table 2.2.: Lepton fields and their masses in the SM. Masses are listed according to [8], the neutrino masses are omitted, because they are very light and only upper bounds have been measured.

$\begin{pmatrix} e \\ \nu_e \end{pmatrix}_L$	e_R	$m_e = 0.511$ MeV
$\begin{pmatrix} \mu \\ \nu_\mu \end{pmatrix}_L$	μ_R	$m_\mu = 105.7$ MeV
$\begin{pmatrix} \tau \\ \nu_\tau \end{pmatrix}_L$	τ_R	$m_\tau = 1.777$ GeV

quarks, two singlets with respect to SU(2)_L (u_R, d_R) are introduced. The right-handed quark fields are in the fundamental representation of SU(3)_C as well. In Table 2.1 the three generations are listed with the measured masses of the corresponding mass eigenstates.

The leptons have the same SU(2)_L structure but are singlets with respect to SU(3)_C. The three generations are shown in Table 2.2. The doublet of the first generation is

$$E_L = \begin{pmatrix} e \\ \nu_e \end{pmatrix}_L$$

and identified with the electron e and the electron-neutrino ν_e. Since the SM does not include neutrino masses, there is only one right-handed SU(2)_L-singlet e_R.

The bosonic fields of the SM are introduced mostly in the context of the covariant derivative, used to establish local gauge invariance with respect to the SM symmetry group, but the Higgs field with its potential has to be postulated as well. The Higgs field is a complex scalar SU(2)_L-doublet ϕ which has a potential of the form

$$V(\phi) = \mu^2 \phi^\dagger \phi - \lambda (\phi^\dagger \phi)^2 \tag{2.4}$$

and thus allows to initiate the electroweak spontaneous symmetry breaking (SSB).

Given the postulated fields, the Lagrangian constructed from the symmetry group contains all allowed terms. Using short-hand notations, the first part of the Lagrangian

contains terms of the form

$$\mathcal{L}_g = -\frac{1}{4}(F_{\mu\nu})^2, \tag{2.5}$$

with field strength $F^a_{\mu\nu} = \partial_\mu A^a_\nu - \partial_\nu A^a_\mu + g f^{abc} A^b_\mu A\nu^c$ (cf. Equation 16.2 in [4]), giving rise to the kinematics of free gauge fields and their self-interactions.

The free evolution of the fermionic fields and the interactions with the gauge bosons arise from this part of the Lagrangian (terms for the second and third family are constructed analogously)

$$\mathcal{L}_f = \bar{E}_L(i\not{\mathcal{D}})E_L + \bar{e}_R(i\not{\mathcal{D}})e_R + \bar{Q}_L(i\not{\mathcal{D}})Q_L + \bar{u}_R(i\not{\mathcal{D}})u_R + \bar{d}_R(i\not{\mathcal{D}})d_R, \tag{2.6}$$

where the covariant derivative $\mathcal{D}_\mu$ is given by $\mathcal{D}_\mu\psi = (\partial_\mu - ig_s G^b_\mu t^b - igA^a_\mu\tau^a - \frac{i}{2}g'B_\mu)\,\psi$ and the notation of the gauge fields of $\mathrm{SU(3)_C}$ G, $\mathrm{SU(2)_L}$ A, and $\mathrm{U(1)_Y}$ B is used and g_s, g, and g' are the respective couplings. t^b and τ^a are the generators of $\mathrm{SU(3)_C}$ and $\mathrm{SU(2)_L}$. The Einstein summation of the $\mathrm{SU(3)_C}$ indices of the quark fields is suppressed and can be trivially added. The Feynman slash notation $\not{\mathcal{D}} = \gamma^\mu\mathcal{D}_\mu$ is used, where γ^μ describes the Dirac matrices.

The so-called Yukawa terms are introduced as

$$\mathcal{L}_{\text{Yukawa}} = -\lambda_e\bar{E}_L\phi e_R - \lambda_d\bar{Q}_L\phi d_R - \lambda_u\epsilon^{ab}\bar{Q}_{La}\phi^\dagger_b u_R + \text{h.c.}, \tag{2.7}$$

and after the electroweak SSB they give rise to the fermionic mass terms of the SM. λ_e, λ_u, and λ_d are the respective Yukawa couplings (once again the terms for the second and third family can be constructed analogously). These are free parameters and have to be chosen to return the observed fermion masses. Note that also diagonal terms for inter-generational mixing are allowed, which can then be parametrised in the CKM matrix.

The kinetic term of the Higgs field is given by

$$\mathcal{L}_H = |\mathcal{D}_\mu\phi|^2, \tag{2.8}$$

where $\mathcal{D}_\mu\phi = (\partial_\mu - igA^a_\mu\tau^a - \frac{i}{2}g'B_\mu)\,\phi$. After SSB, $\mathcal{L}_H$ gives rise to the equations of motion of the free Higgs field, the mass terms of the massive vector bosons, and the interactions of the Higgs boson with the massive vector bosons. Finally, the Higgs potential in Equation (2.4) establishes the EWK SSB and gives rise to the Higgs mass and the Higgs self-interactions.

Given the complete SM Lagrangian, the formalism of Feynman diagrams and Fermi's Golden Rule can be used to derive differential cross sections for specific processes. It has to be noted that vacuum polarisation (i.e. the creation of virtual particle loops) has an effect on the effective coupling between particles. In the case of QED and the coupling of electrical charges, the exchanged photon will create virtual loops of particles and antiparticles depending on the transferred energy. The virtual loops of charged particles, e.g. electrons, lead to an effective screening, i.e. weaker couplings, at larger distances.

In non-abelian gauge theories, the exchanged particles can carry the charge of the gauge group. In the case of the gluon, in addition to the loops of virtual quark-anti-quark pairs, there are also virtual gluon loops. Due to the high number of colours in

Table 2.3.: Bosons of the SM [8]. Due to the prediction by theory, the masses of γ and g are set to 0.

	spin	el. charge	mass [GeV]
H	0	0	125.09
γ	1	0	0
g	1	0	0
$W^{\pm}$	1	$\pm e$	80.385
Z	1	0	91.1876

comparison to quark generations (cf. β function in non-abelian gauge theories in [4]), the anti-screening effect of the gluons is stronger than the screening of the quarks, therefore the strong interaction gets weaker at small distances or high energies, an effect also called asymptotic freedom. Since vice versa the strong force gets stronger for large distances, there cannot be free colour charges, which is also known as confinement. If one tries to separate a colour-charged particle out of a colour-neutral state, the increasing strong interaction at some point reaches the threshold of quark pair production (usually mesons), resulting in two net-colour-neutral states. This is called hadronisation.

An important aspect of the formalism is that it employs perturbation theory, i.e. in most cases the (infinite number of) diagrams to be calculated can be ordered by their contribution, such that only diagrams with the largest contribution need to be calculated.

2.1.2. Particle Content and Interaction Structure

The presented Lagrangian gives rise to two overall categories of particles, the integer-spin particles (bosons) and the half-integer-spin particles (fermions). Due to the Pauli exclusion principle, the fermions make up matter. The fermions do not couple directly to each other, therefore the bosons are needed to mediate the interactions.

Bosons

In each of the introduced symmetry groups the generators of each group can be identified with massless spin-1 bosons which couple to the respective conserved charge. The bosons of the SM are summarised in Table 2.3.

In the case of the $\mathrm{SU(3)_C}$ group, the conserved charge is colour and the generators are identified with the eight gluons, due to obeying the laws of a Yang-Mill's theory carrying colour themselves.

The remaining two symmetry groups have an additional spin to them. Naively, the construction yields three massless spin-1 bosons associated with the $\mathrm{SU(2)_L}$ (usually called W_1, W_2, W_3) and one boson from the $\mathrm{U(1)_Y}$ (called B). This is not realised in nature. As it turns out, the W bosons are massive, which is achieved by the Higgs mechanism. The SSB in the Higgs potential gives rise to four Goldstone bosons, three of which are eaten by the W bosons, giving them mass as well as an additional degree of freedom realised as longitudinal polarisation. The charged W bosons couple to doublets of $\mathrm{SU(2)_L}$, i.e. the upper and lower component of the doublet. The neutral W boson

and B mix (as parametrised by the Weinberg angle θ_W) to form the massive Z boson and the photon γ. The photon couples proportional to the electric charge Q while the Z boson couples proportional to $T_3 - Q\sin^2(\theta_W)$. T_3 is the third component of the weak isospin and Q the electrical charge.

An additional consequence of the Higgs mechanism is the remaining degree of freedom of the fourth Goldstone boson, which manifests itself as an excitation of the Higgs field, a scalar boson called the Higgs boson. It couples to the W and Z bosons and, due to the Yukawa terms containing couplings proportional to the fermion masses, to all massive fermions.

Fermions

The lightest generation of the quarks is the $\mathrm{SU(2)_L}$ doublet of up- (u) and down- (d) quark, where the up-quark carries an electric charge of $\frac{2}{3}e$ and the down-quark an electric charge of $-\frac{1}{3}e$. They make up the nucleons, protons and neutrons. The other generations are unstable and will decay over time. There is inter-generational mixing in the quark-family from the non-diagonal Yukawa terms, which is commonly described with the CKM matrix. For this analysis, the third generation is of special importance. It has an interesting phenomenology. The top quark is the heaviest particle of the SM and has, due to its Yukawa term, the strongest coupling to the Higgs boson. It is too short-lived to hadronise before it decays, and since it has only small inter-generational mixing, it virtually always decays to a b-quark and a W boson. b-quarks on the other hand hadronise and have a decay length $c\tau$ of about 500 μm.

The leptonic family is significantly different from the quarks. The first charged lepton, the electron, is paired with the electron-neutrino ν_e in a $\mathrm{SU(2)_L}$ doublet. The neutrino being neutral and very light[1], does only interact with the $\mathrm{SU(2)_L}$ gauge bosons. Their interaction is rather weak compared to electromagnetism or the strong force. The neutrinos of all generations behave very similarly, except for the fact that they only couple to the charged particle of their own generation.

The second generation charged lepton, the muon μ, is about 200 times heavier than the electron and has a decay length $c\tau$ of 659 m [8], after which it virtually always decays into an electron. At characteristic momenta of current experiments, it is a minimally ionising particle, able to traverse relatively much material before it is stopped.

The tau lepton takes a special role in the SM, since it is the only lepton heavy enough to decay to hadrons. The tau-lepton decay proceeds via an off-shell W boson under emission of a ν_τ. The W boson itself can decay into a lighter lepton (e/μ, cf. Figure 2.1 (a)) or to a pair of quarks (cf. Figure 2.1 (b)), giving rise to fundamentally different signatures.

2.1.3. Limitations

Despite being very successful in describing processes at high-energy experiments and also predicting new phenomena before their discovery, the SM is known to have several

[1] The SM assumes the neutrinos to be massless, but the observation of neutrino oscillations [9, 10] showed that at least two neutrino generations have to have mass. It is straight-forward to extend the SM with neutrino mass terms, but to maintain consistency with the sources and since they are not relevant for the analysis, they are omitted here.

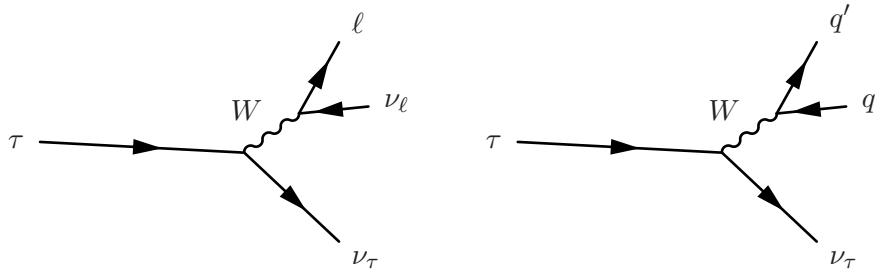

(a) Leptonic decay. (b) Hadronic decay.

Figure 2.1.: The decay modes of the tau lepton.

limitations. These limitations are the motivations to search for "new" physics beyond the SM. Therefore, some of them will be illustrated in the following.

Gravity

One obvious shortcoming of the SM of particle physics is that it doesn't include gravitational interactions. It nevertheless describes the processes at high-energy experiments very well, since gravity is very weak in comparison to the other forces. Gravity is usually observed in bigger accumulations of matter and over larger distances, where the short-range interactions do not contribute and there is no effective electromagnetic force due to the net charge cancelling out. On the other hand, gravity couples proportionally to the energy of particles, therefore the SM is expected to fail to describe processes at extremely high energy scales (M_P[2]). The so-called quantum gravity is supposed to build the bridge to unify the SM with general relativity, but existing ideas either lack experimental verification or are not theoretically robust.

Dark Matter

Astrophysical observations suggest that the Universe does not only consist of the ordinary matter described by the SM but also additional, so-called dark matter. One class of observations are rotation curves of galaxies. With the help of the Doppler effect and knowledge of the observed object, the orbital velocity in dependence of the distance from the centre of the galaxy is measured. As indicated in Figure 2.2 (a), from the luminous matter one would expect a $\frac{1}{\sqrt{R}}$-dependence of the orbital velocity, but observations suggest a much more flat behaviour, which can be explained by additional gravitationally interacting material.

Another observation pointing to dark matter is the bullet cluster. It is a merger of two galaxies which has been observed in the optical and x-ray spectrum, and a weak-lensing analysis was done [12]. Weak-lensing is a method to determine the gravitational matter contribution along the line of sight. Light sources behind a massive object will be distorted according to the formulae of general relativity. Observations of galaxies behind the object to be studied are analysed with respect to the distortions, and a map of the total gravitational matter is derived. The observation in the optical spectrum yields

[2] At latest at the Planck scale ($M_P = 10^{19}$ GeV) quantum gravity has to contribute.

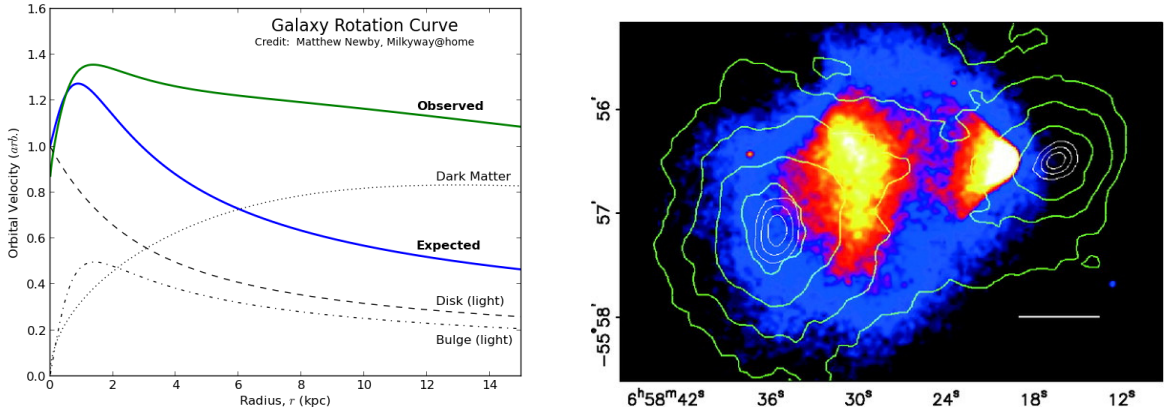

(a) Schematical drawing of the observed and expected rotation curve of a galaxy ([11]). The orbital velocity as a function of the radius of the galaxy is shown. The expected $\frac{1}{\sqrt{R}}$ dependence is shown in blue. In green the dependence of actual observations which can be explained by adding the (dotted) dark matter contribution.

(b) Mass distribution in the bullet cluster [12]. The false-colour image shows the plasma distribution as observed in the x-ray band. The green contours show the distribution of matter inferred from weak lensing.

Figure 2.2.

the luminous matter in the form of stars, which is not interacting during the merger except for the gravitational slow-down, while x-ray observations show the heated intracluster gas which exhibits a strong interaction forming a bow shock. In Figure 2.2 (b) the observations are overlaid. The green contours show the mass distribution according to the weak-lensing observations, the coloured areas show the x-ray observation. The mass inferred from weak lensing is clearly shifted with respect to the gas, and since most of the baryonic matter of the galaxy clusters is contained in the plasma, there has to be a significant amount of non-luminous matter, which is not interacting electromagnetically.

The neutrinos are the only candidates in the SM for a stable particle not interacting strongly or electromagnetically. All other particle would be visible e.g. in the cluster merger of the bullet cluster. According to analyses of structure formation in the Universe, dark matter should be cold in order to allow for galaxy formation, but the SM neutrinos would be too hot for that [8]. There are different candidates for compact dark objects, such as brown dwarfs or black holes, but they are unlikely explanations and strongly constrained by observations. Therefore, there is a strong case to search for new stable weakly-interacting particles not predicted by the SM.

Hierarchy Problem

In the calculation of the amplitudes within the SM, divergences appear which need to be taken care of, in the simplest case in the form of a cut-off energy scale Λ. The procedure developed to achieve that is called renormalisation and interprets the divergences causing the scale-dependence of the interactions as also scale-dependent (so-called physical) masses and couplings. The infinities are "hidden" in counter terms and "bare" quan-

tities. With the help of a proof by 't Hooft and Veltman [13], it was shown that the SM is indeed renormalisable, ensuring that the results of the SM do not depend on the scale Λ.

Nevertheless, it is interesting to look at the quantum corrections being regulated with the renormalisation scheme. The masses of fermions and massive vector bosons are protected from large quantum corrections by chiral symmetry and gauge invariance respectively [5]. The Higgs mass, on the other hand, arising from the only spin-0 field, receives quantum corrections which grow proportionally to the cut-off scale Λ. Figure 2.3 shows the diagrams with one-loop quantum corrections to the higgs mass. Λ has to be identified with the scale where new physics (in the form of new particles or interactions) enters, which in the worst case could be M_P, if the SM would be valid until quantum gravity is setting in. If there is no new physics below that scale, the physical Higgs mass would be sensitive to this scale due to the quantum corrections. It is important to note that the relatively low Higgs mass of the order of 100 GeV would result from the difference of two values of the order of 10^{18} GeV, which have completely different origins and only accidentally almost cancel. This feels very unnatural, therefore this problem is sometimes called finetuning or lack of naturalness.

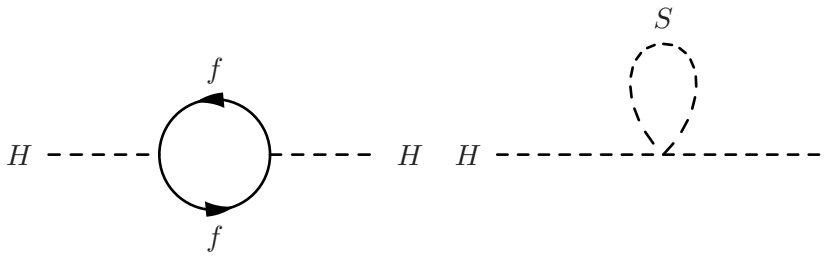

(a) Fermionic quantum correction to the Higgs mass.

(b) Scalar quantum correction to the Higgs mass.

Figure 2.3.: One-loop contributions to the Higgs mass.

Fundamental Theory and Unification

The SM is a closed theory with high predictivity, nevertheless, there are some aspects of the SM which suggest a more fundamental theory. For example, all fermion masses are introduced ad-hoc with Yukawa couplings, which are not determined by the SM, but each of them is a parameter of the theory. A theory predicting the Yukawa couplings and explaining their big spread would, as long it also contains the remaining known phenomenology, be favoured over the SM.

Following the success of the electroweak unification, a valid question is how the SM could be extended to a grand unified theory (GUT). As discussed before, the couplings of the SM depend on the energy transferred with the exchanged particle, which is why they are called running couplings. From a theory point of view, a unification of the running coupling constants would be desirable. As depicted in Figure 2.4 the coupling constants do not meet at a higher scale in the SM, but in the Minimal Supersymmetric Standard Model (MSSM) with new supersymmetric particles at the TeV scale they do.

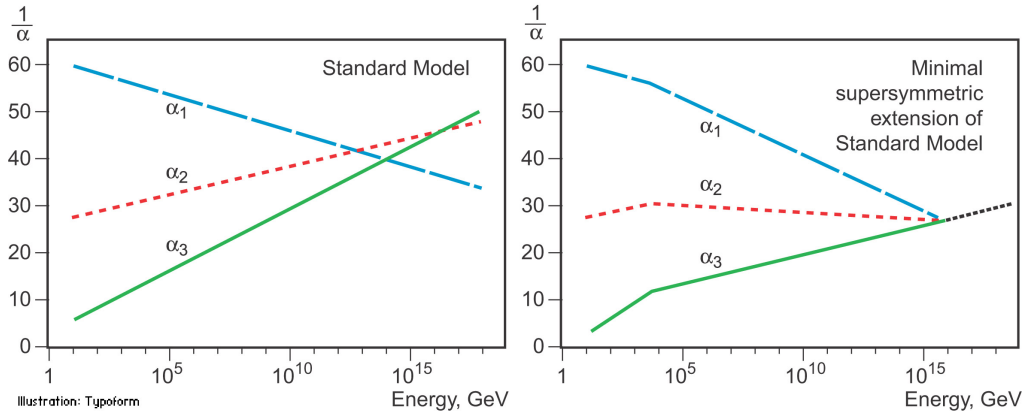

Figure 2.4.: Qualitative evolution of the inverse of the coupling constants of the gauge groups with the energy scale [14]. The evolution in the SM is shown on the left. The couplings do not meet in one point. The evolution in the MSSM, assuming supersymmetric particles at the TeV scale, is shown on the right. There, the couplings meet in one point.

2.2. Supersymmetry

> I'm a fan of supersymmetry, largely because it seems to be the only route by which gravity can be brought into the scheme.
>
> Peter Higgs in an interview with the New Scientist [15]

Given the known shortcomings of the SM it is natural to ask which new theories could take the place of the SM and solve (some of) these problems. SUSY is an appealing idea for an extension of the SM since it can provide solutions to several of the limitations of the SM. SUSY is not a single theory but a framework of theories, therefore in the following, an introduction to the basic concepts of SUSY is given and then the discussion narrowed down to the motivations for the signal model considered.

2.2.1. Superpartners and Interactions

Supersymmetric models share the introduction of an additional space-time symmetry, which assigns to every fermionic degree of freedom a bosonic degree of freedom and vice versa (the corresponding particles are also called superpartners). Out-of-the-box SUSY predicts for each fermion a complex scalar (giving rise to two diagrams) with identical mass. This gives an ad-hoc solution to the hierarchy problem, since for every fermionic diagram (cf. Figure 2.3 (a)) there exist now two bosonic ones (cf. Figure 2.3 (b)) and vice versa. Since they have the same mass running in the loop, these diagrams cancel exactly. Unfortunately, these mass-degenerate superpartners are not observed in nature, therefore SUSY must be a broken symmetry. Usually, a soft, spontaneous breaking is introduced in order to preserve most of the cancellation. The stronger the breaking, the less natural the cancellations become and the finetuning problem returns, but not as drastic as before.

In the formalism of SUSY, the fields are collected conceptually into supermultiplets. There are many possibilities to introduce SUSY. In the following, the discussion will be restricted to the MSSM, introducing the minimal number of additional particles. Each supermultiplet has to contain the same number of bosonic and fermionic degrees of freedom, and the supersymmetry operators transform bosonic into fermionic states and vice versa.

The chiral supermultiplets contain one fermion of the SM each and the corresponding complex scalar fields. The simplified naming convention prepends an "s" to the name of the fermion — the superpartners of the tau lepton are the left or right scalar tau lepton or short "stau" ($\widetilde{\tau}_\mathrm{L}$, $\widetilde{\tau}_\mathrm{R}$). The two scalar states do not carry physical spin, therefore the left (right) labelling is used to discriminate the two distinct physical states and to indicate that they are superpartners of the respective SM particles. Since the quantum numbers of the left- and right-sfermions are identical, both sfermions will mix (depending on the details of the SUSY breaking) and form mass eigenstates, e.g. a light state $\widetilde{\tau}_1$ and a heavy state $\widetilde{\tau}_2$. The mixing can be parameterised with a mixing angle $\theta_{\widetilde{\tau}}$ [16]:

$$\begin{pmatrix} \widetilde{\tau}_1 \\ \widetilde{\tau}_2 \end{pmatrix} = \begin{pmatrix} \cos(\theta_{\widetilde{\tau}}) & -\sin(\theta_{\widetilde{\tau}}) \\ \sin(\theta_{\widetilde{\tau}}) & \cos(\theta_{\widetilde{\tau}}) \end{pmatrix} \begin{pmatrix} \widetilde{\tau}_\mathrm{L} \\ \widetilde{\tau}_\mathrm{R} \end{pmatrix} \tag{2.9}$$

The Higgs sector is extended within the framework of the MSSM to contain two Higgs doublets in order avoid gauge anomalies (cf. also [16]). This gives rise to two additional chiral supermultiplets (usually called H_u and H_d) where the Higgs bosons correspond to the bosonic degrees of freedom, while the superpartners are fermions. For fermionic superpartners the naming convention is to append "-ino" to the name of the corresponding boson, thus the fermionic states are called higgsinos.

The vector supermultiplets contain the SM gauge bosons, which are massless before the electroweak symmetry breaking happens. Their fermionic superpartners are called gauginos. The multiplets relate gluons with gluinos ($\widetilde{g}$), W bosons with winos ($\widetilde{W}$), and B bosons with binos ($\widetilde{B}$). Since the quantum numbers of the higgsinos and gauginos are the same, their mass eigenstates are mixtures of the charged and neutral gauginos and higgsinos. Therefore, the four neutral mass eigenstates are called neutralinos and numbered from the lightest ($\widetilde{\chi}_1^0$) to the heaviest ($\widetilde{\chi}_4^0$), the two charged mass eigenstates are called charginos and labelled $\widetilde{\chi}_1^\pm$ and $\widetilde{\chi}_2^\pm$, respectively.

If supersymmetry is promoted to a local symmetry, the introduction of a spin-2 field is necessary. Conveniently, this is also what is needed for inclusion of the graviton, the hypothetical messenger of gravity, which breaks the renormalisability of the theory. This is generally accepted since the MSSM has to be understood as an effective theory, which is still lacking the implementation of quantum gravity. The superpartner in this multiplet has a spin of $\frac{3}{2}$ and is called gravitino ($\tilde{G}$).

In addition to the SM vertices, the MSSM gives rise to a number of additional interactions (cf. [16]). Figures 2.5 (a)–(c) are the interactions between fermions (scalars) and bosons arising from the covariant derivative, analogously to Equations (2.6,2.8). The most general supersymmetric, gauge invariant Lagrangian can contain terms coupling a fermion to a sfermion and a gaugino (Figures 2.5 (d) and (e)).

The superpotential allows for the addition of Yukawa terms as in Equation (2.7), where now also the scalar sfermions can interact with the SM fermions. Terms coupling

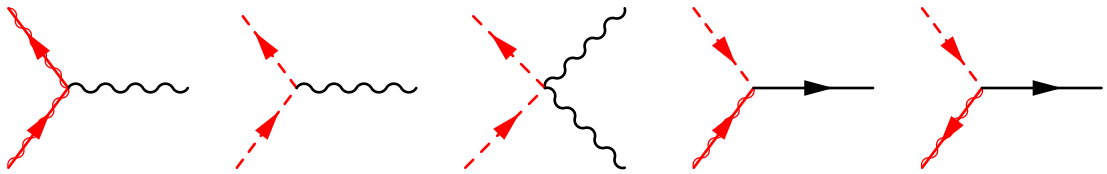

(a) (b) (c) (d) (e)

Figure 2.5.: Additional gauge-boson and gaugino interactions in the MSSM. The red lines indicate superpartners. A solid line overlayed with a wiggly line corresponds to a gaugino or higgsino. The dashed lines indicate the sfermions, i.e. complex scalars. The arrows indicate whether the particle is the superpartner of a particle or anti-particle. For sfermions it can be interpreted as pointing into the direction of the flow of baryon or fermion number.

three or four scalar fields in the same way as for the Higgs potential can be seen in Equation (2.4). Figure 2.6 (a) shows an example for a vertex coupling fermions to a sfermion. Several versions of this vertex exist, but they violate baryon or lepton number [17], and will therefore not be included (cf. Section 2.2.2). Figures 2.6 (b) and (c) show the interactions of three scalar fields and Figure 2.6 (d) finally the quartic scalar interaction.

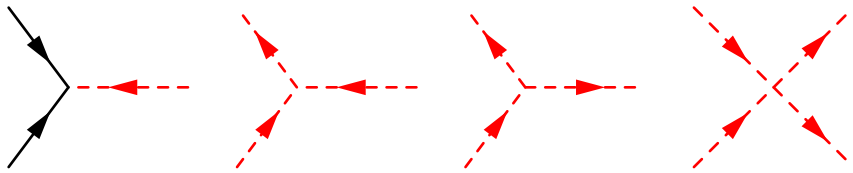

(a) (b) (c) (d)

Figure 2.6.: MSSM interactions arising from the superpotential.

2.2.2. R-Parity Conservation

The Yukawa terms leading to the trilinear vertices, as the example shown in Figure 2.6 (a), can in principle couple different kinds of fermions to a scalar field (the exact vertices are discussed in [18]). Via an intermediate squark the decay of a proton would therefore be possible (cf. Figure 2.7). Protons on the other hand, are known to have a very long lifetime. Recent results by the Super-Kamiokande Collaboration set lower limits on the proton lifetime of 1.6×10^{34} years [19]. Since this suggests that the Yukawa couplings violating baryon and lepton numbers are negligible, the conserved multiplicative quantity R-parity

$$P_R = (-1)^{3(B-L)+2s} \tag{2.10}$$

is introduced, where B (L) is the baryon (lepton) number and s the spin of the particle.

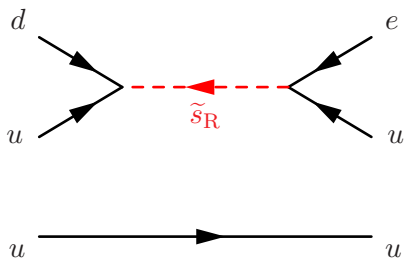

Figure 2.7.: Example of the proton decay $p^+ \to e^+ \pi^0$ in SUSY without R-parity conservation.

Introducing R-parity conservation has immediate consequences for the phenomenology: since the superpartners of SM particles have negative R-parity, while SM particles have positive R-parity, they can only be produced in pairs. Once produced, superpartners can only decay to other superpartners (and additional SM particles) or annihilate with other SUSY particles. Their decays cascade down to the lightest supersymmetric particle (LSP), which is now stable due to the R-parity conservation. This stable LSP gives rise to a potential dark matter candidate if the LSP does not carry electrical or colour charge, as suggested by observations.

2.2.3. SUSY Breaking

Given the fact that there are no observations of superpartners with the same mass as their SM counterparts, SUSY has to be broken. In general, it is possible to add soft SUSY-breaking terms to the superpotential. Since the exact phenomenology of SUSY breaking cannot easily be predicted, it is useful to make simplifying assumptions on the breaking mechanism. In the literature several popular breaking mechanisms are discussed, e.g. gravity- or anomaly-mediated SUSY breaking. The model studied in this analysis is inspired by gauge-mediated SUSY breaking (GMSB), which assumes a local supersymmetry. Therefore, the discussion will focus on the implications of this ansatz.

The general idea of GMSB is that the underlying mechanism introducing the breaking is hidden in a separate sector not yet accessible with experiments. There is a communication with this sector with the help of heavy mediator particles, which have the SM gauge interactions as well as some interaction with the hidden sector. Since the mediator particles obey the SM interactions, no new flavour-violating terms arise.

Since SUSY is broken spontaneously, according to the Goldstone theorem, this gives rise to a Goldstone boson (called Goldstino). This Goldstino will not appear as a physical particle, but is eaten by the spin-$\frac{3}{2}$ gravitino giving it mass as well as a longitudinal component. The fundamental SUSY-breaking scale can be much lower in GMSB than e.g. in gravity-mediated SUSY breaking, which directly gives rise to a light gravitino [5]. Since the gravitino can be a dark-matter candidate, it is commonly assumed to be the LSP of GMSB models.

The gravitino itself has an extremely weak coupling to other particles, therefore it could lead to long-lived to almost stable next-to-lightest supersymmetric particles (NLSPs). It was shown that the S-matrix elements for longitudinally polarised $\tilde{G}$s are equivalent to the S-matrix elements if the longitudinal polarisation of $\tilde{G}$s is replaced by

Goldstinos [20, 21]. As a consequence, it follows that the spin-$\frac{1}{2}$ component of the $\tilde{G}$ will mediate the significantly stronger coupling of the Goldstino, evading the problem of longevity of the NLSPs.

That the experiments at LHC did not observe SUSY within Run 1, could be an indication that there is more than minimal finetuning. For some time already, it has been suggested that one way to create heavier sfermions, while maintaining low finetuning, is that the $\tilde{t}_1$ is the lightest sfermion, because due to the lower Yukawa couplings the other sfermions do not contribute as much [22]. The mass generated from the SUSY breaking in GMSB originates from loop corrections. Due to their colour, squarks have additional loop contributions, therefore they are expected to be heavier than the colourless sleptons [5].

The sleptons themselves are usually mass degenerate within the GMSB. But the $\widetilde{\tau}$ has the largest Yukawa couplings within the sleptons, therefore it can receive larger corrections to its mass (which depend on $\tan(\beta)$), where $\tan(\beta) = v_u/v_d$ is the ratio of the vacuum expectation values of the respective Higgs fields. These corrections can reduce the mass of the $\widetilde{\tau}_1$ and therefore motivate the $\widetilde{\tau}_1$ as a candidate for the NLSP [5] and suggests in combination with the colour-loop argument a mass hierarchy where $m_{\tilde{t}_1} > m_{\widetilde{\tau}_1}$.

2.3. Simplified Models

When designing a search for new physics beyond the SM within the context of the MSSM, there are different options how the signal expectation can be modelled. In principle, all parameters of the MSSM can be set to fixed values (including constraints from observations) to obtain a realistic model. This has the problem that for a certain set of parameters different final states can contribute to the chosen model. For each final state different techniques, e.g. for background estimation, need to be developed. The opposite approach is not to assume a certain signal and to look for excesses beyond the SM in generic distributions as e.g. invariant masses of objects. This has the disadvantage that it cannot exploit the kinematic features of a certain MSSM point.

Both approaches exist in their own right, but in this analysis the less complicated, but still powerful approach of a simplified model is used. It is inspired by a real model, but fixes the branching fractions into a certain final state, such that only this final state needs to be considered. On the technical side an event generator is used which is able to simulate SUSY processes correctly, but works with arbitrary branching fractions, masses, and mixings.

In the analysis presented in the following, the simplified model takes inspiration from the GMSB, by assuming that the $\tilde{G}$ is the LSP and that due to a large $\tan(\beta)$ the $\widetilde{\tau}_1$ is the NLSP. Light top squarks are important to ensure naturalness, therefore we assume that they are within reach of the LHC and for simplicity we assume that no other particles are directly accessible.

The mass hierarchy of the model considered is therefore $m_{\tilde{t}_1} > m_{\widetilde{\tau}_1} > m_{\tilde{G}}$ and has several open decay channels. The decay channels where the $\tilde{t}_1$ decays to a final state with a $\tilde{G}$ are not competitive with the decay via a virtual $\widetilde{\chi}_1^{\pm}$ to the $\widetilde{\tau}_1$, due to the smaller Goldstino couplings.

How the decay mode $\tilde{t}_1 \to b\nu_\tau\tilde{\tau}_1$ can be isolated, shall be motivated with the help of the results of a paper by W. Porod [23]. There, a slightly different model is discussed, instead of using the $\tilde{G}$ as LSP, the $\tilde{\chi}_1^0$ is used and the direct decay of $\tilde{t}_1 \to t\tilde{\chi}_1^0$ is kinematically forbidden. Figure 2.8 shows the branching fractions of the $\tilde{t}_1$ decay as a function of $\tan(\beta)$. The empty squares show the sub-process $\tilde{t}_1 \to b\nu_\tau\tilde{\tau}_1$, which dominates for high values of $\tan(\beta)$ over the subprocesses with sneutrinos or the other sleptons in the final state. The caveat of this model is that, due to the $\tilde{\chi}_1^0$ being the LSP, the decay mode $\tilde{t}_1 \to bW^+\tilde{\chi}_1^0$, which is not shown in the plot, dominates. Since the $\tilde{\chi}_1^0$ is replaced by the $\tilde{G}$ as LSP in GMSB, the corresponding decay $\tilde{t}_1 \to bW^+\tilde{G}$ is much slower, such that $\tilde{t}_1 \to b\nu_\tau\tilde{\tau}_1$ overtakes and dominates for high values of $\tan(\beta)$. The $\tilde{\chi}_1^\pm$ should not be too heavy, such that the decay $\tilde{t}_1 \to t\tilde{G}$ does not get competitive to $\tilde{t}_1 \to b\nu_\tau\tilde{\tau}_1$.

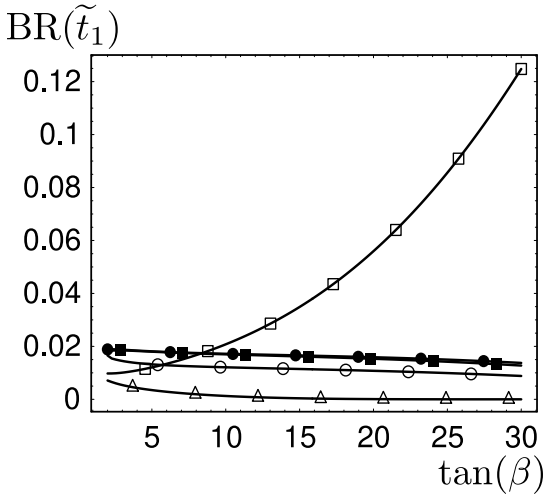

Figure 2.8.: Branching fractions of $\tilde{t}_1$ as a function of $\tan(\beta)$ (taken from [23]). The empty squares correspond to the subprocess $\tilde{t}_1 \to b\nu_\tau\tilde{\tau}_1$, the other symbols correspond to the other subprocesses with sneutrinos or the other sleptons in the final state. Note that the cited paper does not assume GMSB, and therefore the branching fraction is dominated by $\tilde{t}_1 \to bW^+\tilde{\chi}_1^0$ (not shown in the graph), which is suppressed if the LSP is a gravitino instead of a neutralino.

The simplified model considered in the analysis presented allows to study the channel of $\tilde{t}_1$ decaying to $\tilde{\tau}_1$ in detail. The kinematics can be exploited in order to achieve a good signal-to-background discrimination. The interpretation will be done for 100 % branching fraction, but it has to be kept in mind that realistic MSSM models might yield lower branching fractions. On the other hand, this analysis will define search regions with b-jets and tau leptons in kinematic regimes with low SM contributions, therefore the results can also be interpreted in other models with this final state.

2.3.1. Description of the Simplified Model

In the signal model analysed in this thesis, three particles are assumed to be in mass-reach of the LHC. The heaviest of the three is the $\tilde{t}$, the NLSP is the $\tilde{\tau}$ and the $\tilde{G}$ is the LSP. All branching fractions are set to 100 %. The model fixes $m_{\tilde{G}}$ as negligibly small,

while varying $m_{\tilde{t}_1}$ and $m_{\widetilde{\tau}_1}$ independently to cover a large phase space.

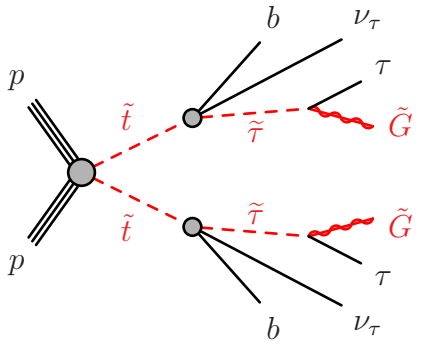

Figure 2.9.: Simplified model considered in this analysis. Direct production of a $\tilde{t}_1$-pair decaying via a three-body decay to b-quark, ν_τ, and $\widetilde{\tau}_1$, where the $\widetilde{\tau}_1$ decays to a SM-τ and a $\tilde{G}$. All branching fractions are assumed to be 100 %.

Figure 2.9 shows a simplified Feynman diagram of the process. The direct production of a $\tilde{t}_1$ pair from proton–proton collisions is assumed, in accordance to having the largest cross section of the three sparticles. The $\tilde{t}_1$ is simulated to be $\tilde{t}_\mathrm{L}$, but since the $\tilde{t}_1$ production cross section to first order only depends on $m_{\tilde{t}_1}$ and not the $\tilde{t}$ mixing [24], it is not expected to have significant impact on the interpretation.

By construction of the simplified model, the $\tilde{t}_1$ decays via a three-body decay via an intermediate virtual chargino to a SM b-quark, a SM ν_τ, and a $\widetilde{\tau}_1$. The $\widetilde{\chi}_1^\pm$ is simulated to be $\widetilde{W}$-like, which has an effect on the following $\widetilde{\tau}_1$ production. In the case that the $\widetilde{\chi}_1^\pm$ is $\widetilde{W}$-like, the $\widetilde{\tau}_1$ will be produced as $\widetilde{\tau}_\mathrm{L}$, since the $\widetilde{W}$ can only couple to the particles of the $\mathrm{SU}(2)_\mathrm{L}$ doublet (cf. Figure 2.10 (a)). If the $\widetilde{\chi}_1^\pm$ on the other hand is $\widetilde{H}$-like, due to lepton-number and charge conservation the neutrinos have to be the same chirality as in the $\widetilde{W}$-like case, but the $\widetilde{\tau}_1$ are now produced as $\widetilde{\tau}_\mathrm{R}$ (cf. Figure 2.10 (b)). The $\tilde{G}$, which couples with its spin-$\frac{1}{2}$ Goldstino-like component, conserves chirality, therefore the final-state tau leptons will both be left-handed in the case of a $\widetilde{W}$-like $\widetilde{\chi}_1^\pm$ and both be right-handed in case of a $\widetilde{H}$-like $\widetilde{\chi}_1^\pm$. If there is significant $\widetilde{\tau}$-mixing, it can dilute this clear picture. The tau lepton polarisation has a direct effect on the momentum spectra of the decay products due to the chiral decay via a W boson. Since the chargino- and stau-mixings are not unambiguously motivated by theory, the tau leptons are assumed to be unpolarised.

The emitted final-state particles are two b-quarks, two ν_τ from the three-body decay, two tau leptons and two gravitinos. The b-jets originating from the b-quarks (cf. Section 5.3) leave a distinct signature in the detector and can be tagged. The tau leptons give rise to three different channels due to their very different decay modes. In the case that both tau leptons decay in a hadronic mode, the channel is called had-had (ca. 42 %). If both tau leptons decay into a light lepton (e or μ) the channel is called lep-lep (ca. 12 %). The lep-had channel, where one tau decays to a light lepton and the other decays hadronically is the most likely one (ca. 46 %). Depending on the decay mode of the tau leptons, two to four additional neutrinos are emitted in this process. Gravitinos and neutrinos are weakly interacting and can therefore not be detected directly. The indirect detection of the escaping particles will be discussed in Section 5.3.

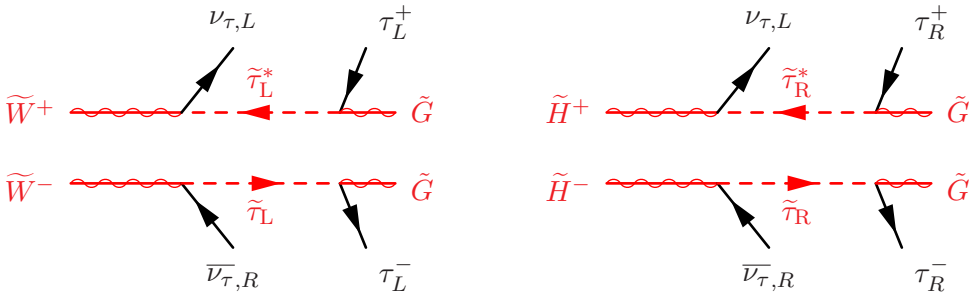

(a) $\widetilde{W}$-like decay. (b) $\widetilde{H}$-like decay.

Figure 2.10.: $\tilde{\chi}_1^{\pm}$ decays, with the chiralities of the particles given explicitly.

2.3.2. Simplified Model in Context

Numerous SUSY searches have already been carried out at high-energy physics experiments, therefore this search is put into the context of other already published results here.

Run-1 Analysis

The presented simplified model targets a phase-space which has only been covered in Run 1 until now. The previous analysis was carried out at 8 TeV centre-of-mass energy with 20 fb^{-1} of data [1] using an equivalent signal model. Figure 2.11 shows the exclusion limits set by this analysis. The overlaid LEP limit will be discussed in the following section. At 95 % CL $\tilde{t}_1$ masses up to 650 GeV and $\tilde{\tau}_1$ masses up to 490 GeV have been excluded.

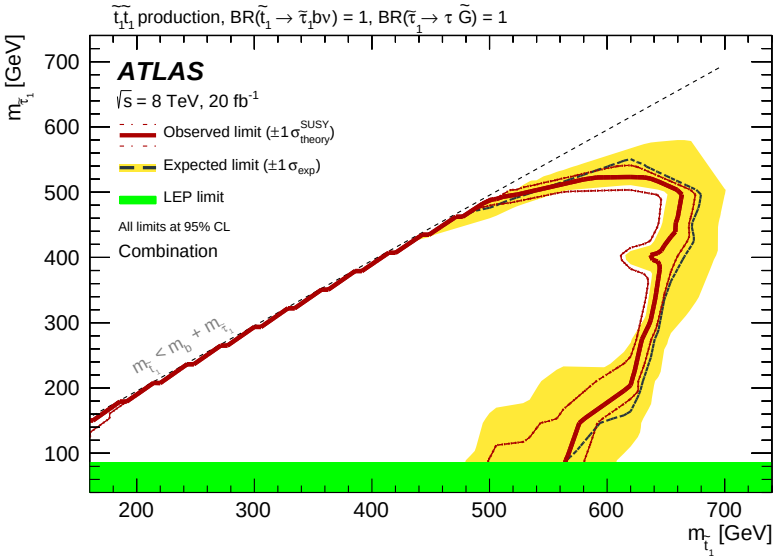

Figure 2.11.: Exclusion limits of the Run 1 analysis targeting an equivalent simplified model [1].

The $\tilde{t}_1$-pair production cross-section calculations for 8 TeV [25] and 13 TeV [26] centre-

of-mass energy are combined in Figure 2.12. It can be seen, that depending on $m_{\tilde{t}_1}$ the production cross-section increases significantly from 8 TeV to 13 TeV. In combination with a higher integrated luminosity and improvements in the particle identification, the sensitivity of the Run 1 analysis is expected to be surpassed.

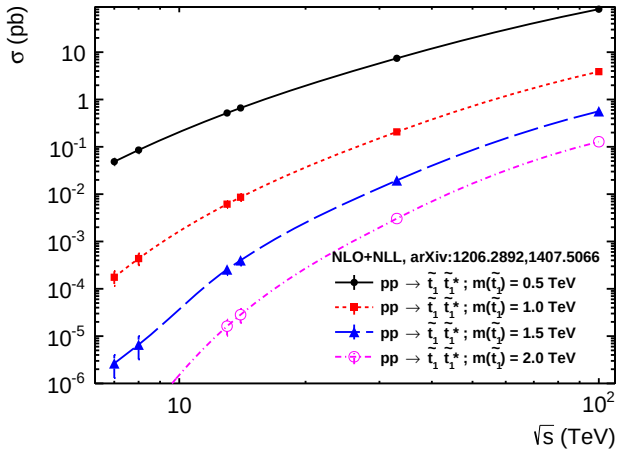

Figure 2.12.: $\tilde{t}_1$ pair-production cross section as a function of the centre-of-mass energy for various $m_{\tilde{t}_1}$ (from the public webpage in [27] following the prescriptions in [25] and [26]).

Limits on Tau Slepton Masses from Direct Production

The experiments at LEP have published combined limits on $m_{\widetilde{\tau}_1}$ from searches for direct production of $\widetilde{\tau}_1$ pairs in e^+e^- collisions [28]. The experiments assumed that the $\widetilde{\chi}_1^0$ is the LSP. Even with this hypothesis, the $m_{\widetilde{\tau}_1}$ limits from the LEP experiments are almost directly applicable to the simplified model discussed here. The expected kinematics is very similar, since both models assume prompt $\widetilde{\tau}_1$ decays and, as discussed before, the longitudinal component of the $\tilde{G}$ interacts like a spin-$\frac{1}{2}$ Goldstino — the same spin as the $\widetilde{\chi}_1^0$. The branching fraction of 100 % for the processes $\widetilde{\tau}_1 \to \tau\widetilde{\chi}_1^0$ and $\widetilde{\tau}_1 \to \tau\tilde{G}$ eliminates the differences of the respective couplings. The limit on $m_{\widetilde{\tau}_1}$ for an almost massless $\widetilde{\chi}_1^0$ is about 90 GeV (cf. Figure 2.13) and can be directly applied to the simplified model presented here.

Searches for direct production of $\widetilde{\tau}_1$ pairs at LHC do almost nowhere reach exclusion potential yet. Analyses at CMS at 8 TeV [29] and 13 TeV [30, 31] do not provide exclusion, while the 8 TeV analysis of ATLAS [32] only excludes one benchmark point at $m_{\widetilde{\tau}_1} = 109$ GeV.

Summary

The simplified model presented here has a unique signature of tau leptons, b-quarks, and detector-invisible particles. Limits on the mass of the NLSP ($\widetilde{\tau}_1$) exist but cover only a small phase space of this simplified model, since higher values of $m_{\widetilde{\tau}_1}$ are accessible due to the much larger cross-section of $\tilde{t}_1$-pair production and the richer final state. If

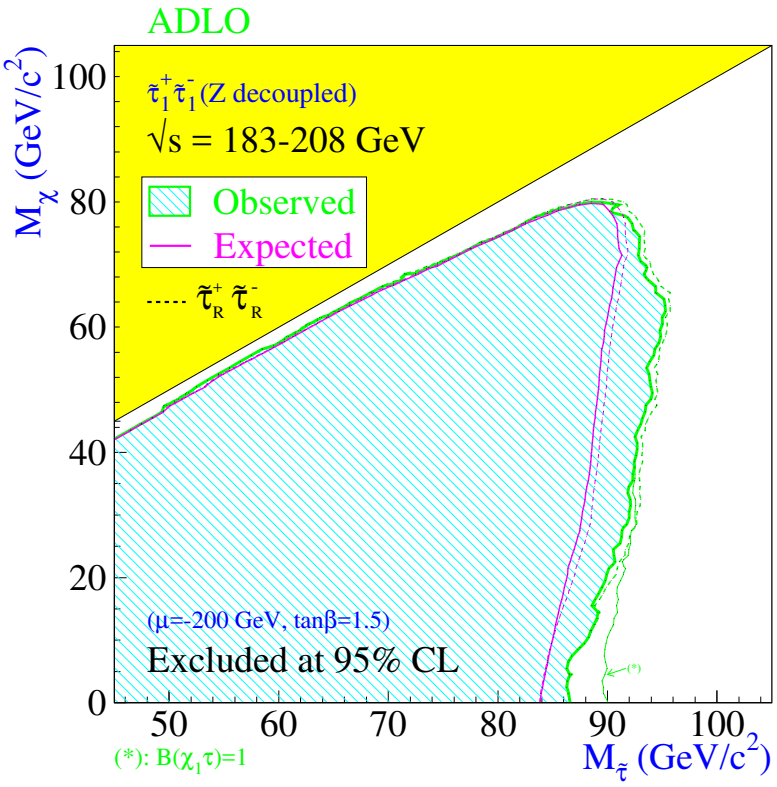

Figure 2.13.: Combined limits on $m_{\widetilde{\tau}_1}$ at 95 % CL by the LEP experiments [28]. The green line marked with an asterisk corresponds to the limit in case of 100 % branching fraction in the process $\widetilde{\tau}_1 \to \tau\widetilde{\chi}_1^0$, corresponding to the assumptions of the simplified model presented here.

the $\tilde{t}_1$ does not decay predominantly into $\widetilde{\tau}_1$, a number of other dedicated analyses are competitive for direct $\tilde{t}_1$ pair production (for ATLAS analyses refer to [33–36], for CMS to [37–39]).

3. The Large Hadron Collider

The LHC is a circular collider designed to collide protons at a centre-of-mass energy of 14 TeV and lead ions at 1150 TeV [40, 41]. It is 27 km in circumference and situated underground in the larger Geneva area close to CERN.

It consists of eight arcs and eight straight sections, where the arcs house the dipole magnets and the straight sections are either used for beam handling or collision points. The superconducting dipole magnets used to keep the beam in the circular orbit within the LHC beam pipes are designed to provide a magnetic field of 8.33 T and are cooled with superfluid helium down to 1.9 K. Four of the straight sections contain special areas for beam cleaning, acceleration, and the ejection system for the beam dump. At the other four straight sections the beams cross and can be brought to collision. The main experiments ATLAS, ALICE, CMS, and LHCb are located there.

Until now LHC has finished its first so-called run in 2012 (Run 1) and is currently in Run 2. These runs are separated by long shutdowns which are used to upgrade the machines and detectors. The most important changes of LHC for Run 2 were the increase in centre-of-mass energy from 8 TeV to 13 TeV, as well as the reduction of the bunch spacing from 50 ns to 25 ns. Both changes increase the production rates for heavy states.

3.1. Proton-Proton Collisions

The LHC can collide different types of ions. Lead ions are used since due to their high mass they can create a quark-gluon plasma, but most of the beam time is devoted to proton-proton collisions. Searches for new particles profit from the higher energy per interacting constituent of the proton-proton collisions, leading to higher production rates of heavy states. In the heavy-ion collisions the ions have a higher total energy, which is distributed on more constituents, leading to a lower maximally accessible centre-of-mass energy. Even non-central interactions usually involve more than one nucleon, making the resolution of the final state difficult.

Acceleration Complex

In order to fill the LHC with high-energetic protons, a multi-stage acceleration process is employed (cf. Figure 3.1 for a schematic of the complex). Protons are ionised from hydrogen gas and accelerated in high-intensity bunches in the linear accelerator LINAC 2 to an energy of 50 MeV. They are collected in the Proton Synchrotron Booster (PSB), accelerated to an energy of 1.4 GeV, and transferred to the Proton Synchrotron (PS).

The bunch structure is created with the radio-frequency acceleration scheme in the PS by splitting the beams using higher harmonics of the revolution frequency [43]. Bunches

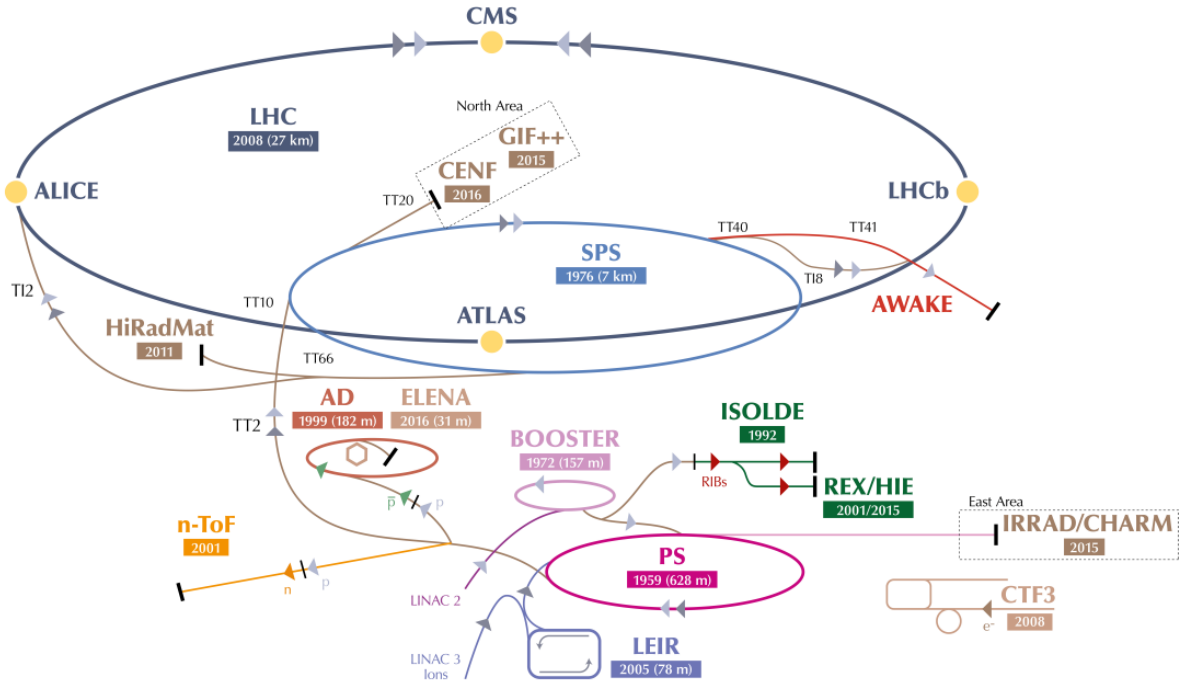

Figure 3.1.: Sketch of the accelerator complex at CERN [42]. The light-grey arrows (starting at LINAC 2) indicate the way protons take until they finally arrive in the LHC, where they are injected clockwise and counterclockwise.

are grouped into so-called trains, in which the bunches are usually spatially separated in the minimal bunch spacing, but between the trains there are gaps to make the transitions between the accelerators possible. The minimal bunch spacing is an important parameter since following bunch crossings can influence each other (cf. also Section 3.3) — in the considered dataset the minimal bunch spacing is 25 ns.

In the PS the protons are accelerated to 25 GeV to be injected into the Super Proton Synchrotron (SPS), where they are accelerated up to 450 GeV. From the SPS the LHC is filled with two transfer beam-lines clockwise and counterclockwise, since it is the first machine in the acceleration chain to have two beam pipes with opposite magnetic dipole fields. The LHC finally does the last acceleration step to currently 13 TeV and delivers the collisions at the dedicated interaction points.

Parton Distribution Functions

Since the proton has a substructure easily resolved at the energies of the LHC, the interaction of interest usually involves one parton of each proton. A parton is one of the constituents of the proton. A proton consists of three so-called valence quarks, two of the up-type, one of the down-type, short-lived gluons exchanging momenta in between the quarks, and so-called sea quarks, short-lived quarks mostly from quark pair production of the gluons.

For the theoretical modelling of the collisions it is important to know which parton is carrying how much momentum. To describe that, the so-called parton distribution functions (PDFs) are measured — the probability density functions to find a certain parton (valence/sea quark or gluon) with a certain momentum fraction of the proton. Figure 3.2 shows an example of the PDFs of a proton at a momentum-transfer scale of $\mu^2 = 10^4$ GeV^2 where the gluons carry a significant momentum fraction.

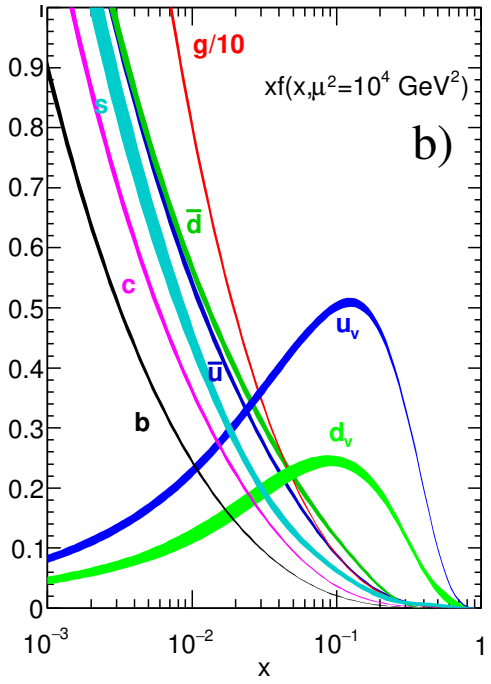

Figure 3.2.: Example for PDFs (NNLO NNPDF3.0) used at the LHC for Run 2 at a momentum scale of $\mu^2 = 10^4$ GeV^2 as a function of the momentum fraction of the proton x [8, 44]. The lines labelled u_v and d_v show the valence quarks, which have a higher probability to carry higher momentum fractions than the remaining sea quarks, while the line labelled "g/10" shows the strong gluon contribution scaled down by a factor of ten.

Since the interacting partons only carry fractions of the momentum of the proton, the energy of the collision and the initial boost of the centre-of-mass frame in beam-direction is not well determined. Therefore, the precise determination of the beam energy is less important than for e.g. electron-positron colliders.

3.2. SM Signatures

There is a number of physics processes relevant in the proton-proton collisions of the LHC. Some of particular interest for this analysis will be highlighted in the following. Figure 3.3 shows the cross-section measurements performed by ATLAS at the different centre-of-mass energies in order to give an overview over the importance of the individual processes.

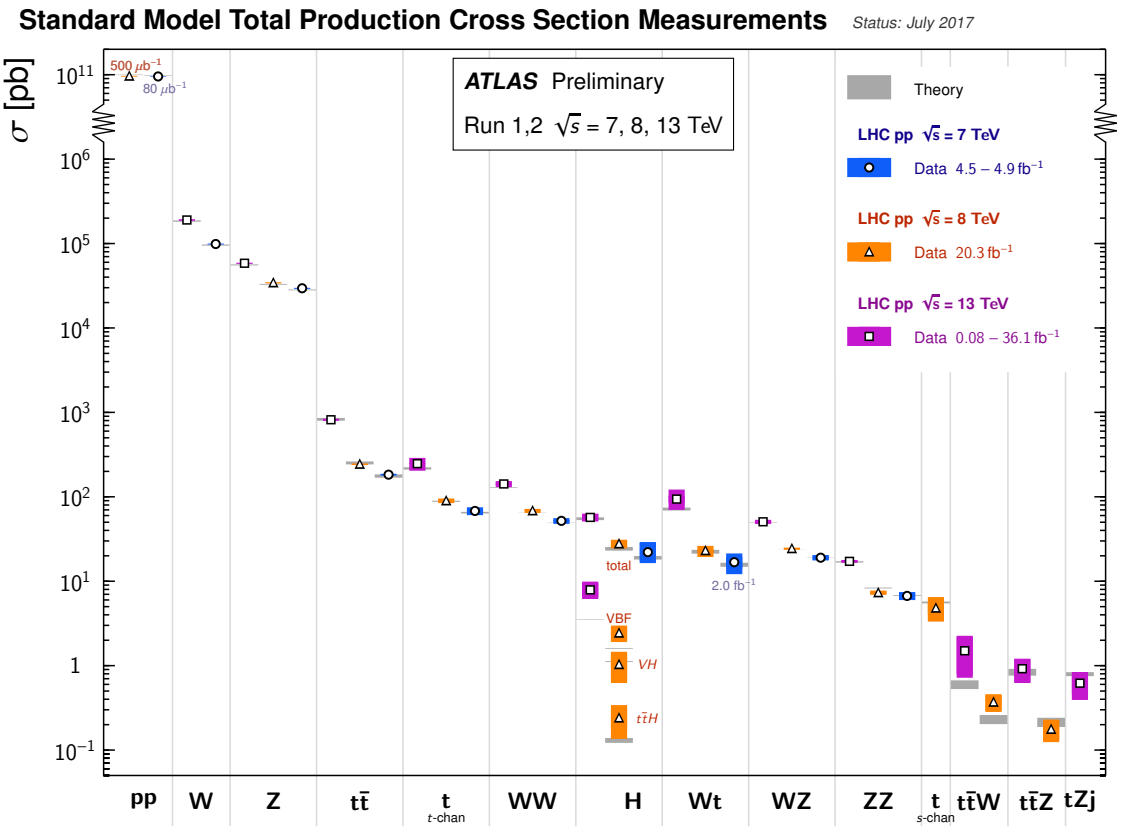

Figure 3.3.: Summary of the SM production cross-section measurements performed by ATLAS at the three different centre-of-mass energies [45]. In the left-most bin the total pp cross section is shown, while in the following bins single sub-processes are shown.

All processes discussed here are primarily identified by a certain hard interaction usually involving at least one heavy particle. It has to be noted that all processes can contain additional initial- and final-state radiation, e.g. a gluon radiated of one of the initial-state partons, or a photon of a charged final-state particle.

Multi-jet

A simple, but due to its large cross section important signature are *multi-jet* events. In this context, multi-jet describes all processes which create final states containing only jets, where jets are the detector signatures of hadrons. More details on the concept of jets are given in Section 4.6. Since the partons carry colour charge, their most likely interaction is the exchange of gluons giving, with potential additional initial- and final-state radiation, rise to two or more jets.

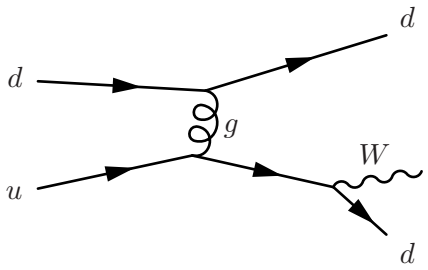

(a) Example for the W+jets process with additional jets in the final state.

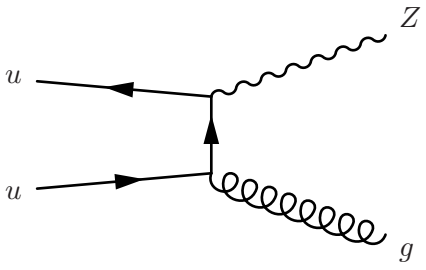

(b) Example for the Z+jets process with additional jets in the final state.

Figure 3.4.: Examples for processes with massive vector bosons and additional jets in the final state.

Massive Vector Bosons + Jets

With relatively large cross sections, the production of massive vector bosons (W, Z) in association with jets in the final state (V+jets) is a dominant signature at LHC. Due to their high mass and their leptonic decay channels the V+jets processes contribute to many final states involving high-energetic leptons. Two examples of possible Feynman diagrams are shown in Figure 3.4, where the W bosons can decay to $\ell\,\nu_\ell$ and the Z bosons can decay to $\ell^+\,\ell^-$, where ℓ can be any charged lepton (e, μ, or τ). Both bosons can also decay hadronically, giving in both cases rise to an all-jet final state. The Z boson can decay to a pair of neutrinos, resulting in an all-jet final state with additional momentum imbalance.

Top-Quark Pair Production

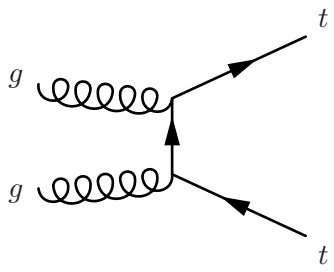

(a) $t\bar{t}$ production process.

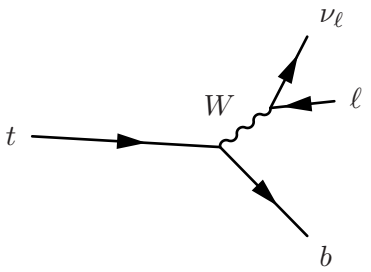

(b) Leptonic decay mode of a top-quark.

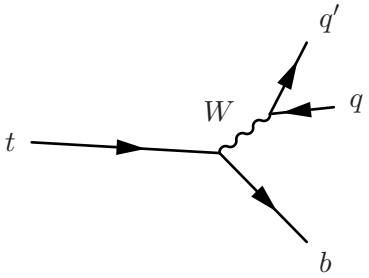

(c) Hadronic decay mode of a top-quark.

Figure 3.5.: The $t\bar{t}$ process with diagrams for production and decay.

A rich variety of final states originates from top-quark pair ($t\bar{t}$) production. A common production diagram is given in Figure 3.5 (a). The top quarks decay virtually always via the emission of a W boson to a b-quark, while the W boson itself decays either to a charged lepton and the corresponding neutrino (Figure 3.5 (b)) or two quarks (Figure 3.5 (c)). The two W bosons decay independently, therefore all combinations of quarks and leptons (including their respective generations) are possible, only the total charges of the branches have to be of opposite sign.

Single Top-Quark production

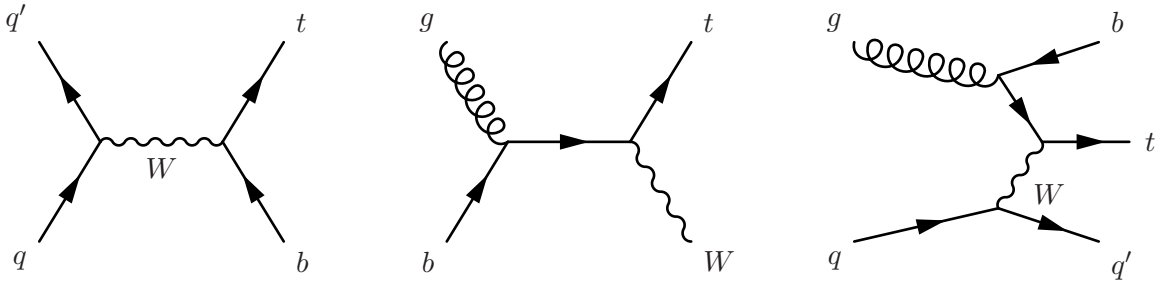

(a) s-channel (b) Wt-channel (c) t-channel

Figure 3.6.: The three single-top processes.

Single top-quark production (single top) has a lower cross section than $t\bar{t}$, since due to the creation of topness in the final state, the direct strong production channel is not open. Therefore, only weak processes contribute but due to the different topology single top can be an important background process.

Three different processes are distinguished (and examples for each of them given): The s-channel, where the W boson is off-shell and carries the final-state momentum (cf. Figure 3.6 (a)), has the smallest cross section. The Wt-channel with a W boson in the final state (cf. Figure 3.6 (b)), has an intermediate cross section. The highest cross section of the three single-top channels has the t-channel, where the W boson is exchanged and interacts with a b-quark from gluon splitting to form a top-quark (cf. Figure 3.6 (c)).

The single-top and $t\bar{t}$ processes are simulated independently. At next-to-leading order (NLO) the final state $WWbb$ has contributions from both processes. Figure 3.7 shows an example for a diagram giving rise to interference. It can be interpreted as a NLO correction to the Wt process, where one of the top-quarks can be off-shell. It is also allowed that both top-quarks are on-shell, but in that case this diagram coincides with the $t\bar{t}$ process as shown in Figure 3.5 (a).

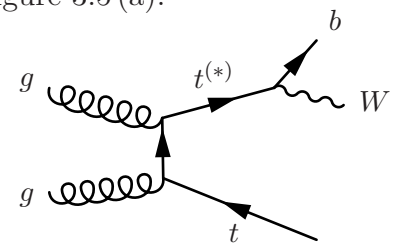

Figure 3.7.: Example for interference of the single-top process in the Wt-channel at NLO with the $t\bar{t}$ process. For the single-top process one of the top-quarks can be off-shell $\left(t^{(*)}\right)$.

Since we try to distinguish the single-top process from the $t\bar{t}$ process by discriminating the weak against the strong production mode, it makes sense to assign the resonant $t\bar{t}$ production, i.e. the process where both top-quarks are on-shell, to the $t\bar{t}$ process. Two approaches are commonly used with the MC@NLO method [46]: the *diagram-removal* scheme removes the diagrams which as e.g. shown in Figure 3.7 are resonant from the

calculation of the single-top NLO amplitude. This is chosen as the baseline approach for the simulation of the Monte Carlo (MC) samples for the Wt channel in this analysis. The alternative scheme is called *diagram subtraction*: it implements a local modification to the differential cross section in the Wt channel, subtracting the contribution of the on-shell $t\bar{t}$ process. Both approaches are only approximately resolving the interference of the two processes, but a sample for the inclusive $pp \to WWbb$ process is not yet available at NLO [47].

Production of Two or More Massive Vector Bosons

Going to even lower cross sections, but still interesting decay signatures, the final states with two massive vector bosons in the final state (VV) are worth mentioning. In order of decreasing cross section the three possible final states are WW, WZ and ZZ, giving rise to up to four leptons, which in the case of ZZ can also all be charged.

Even richer final states at even lower cross sections can be found in events with three massive vector bosons (VVV). They can have a high number of leptons, neutrinos, and jets in the final state.

Associated Top-Quark Production

$t\bar{t}$ and single-top processes with an additional final-state W, Z or Higgs boson are further suppressed by the respective couplings, but can still have large enough cross sections to be relevant in the phase space of interest. As discussed in detail later, especially the $t\bar{t}+Z$ process is worth mentioning, because the $Z \to \nu\nu$ process can give rise to detector-invisible particles on top of the $t\bar{t}$ process. Events with three or more top quarks are very rare, but could potentially be efficiently selected by the signal selection.

Tau-Decay Signatures

Due to its high mass the tau lepton has a number of possible decay channels (cf. Section 2.1.2). The decay length of the tau lepton ($c\tau = 87.03\ \mu\text{m}$)[1] is too short to reliably distinguish the leptonic decay from prompt sources. Therefore, no discrimination of prompt light leptons and light leptons from tau decays is done in this analysis and it is instructive to investigate the contributions of different processes to the studied categories of lep-had and had-had decays.

The tau lepton decays with the following branching fractions to light leptons $\mathcal{B}(\tau_{\text{lep}})$ and hadronic final states $\mathcal{B}(\tau_{\text{had}})$:

$$\mathcal{B}(\tau_{\text{lep}}) = 0.3521,\ \mathcal{B}(\tau_{\text{had}}) = 0.6479$$

Looking at SM background processes containing a W boson the picture changes, since the W boson decays directly to light leptons as well as to tau leptons. The effective W boson branching fraction to light leptons is given by

$$\mathcal{B}(W \to \ell\nu) = \mathcal{B}(W \to e\nu_e) + \mathcal{B}(W \to \mu\nu_\mu) + \mathcal{B}(W \to \tau\nu_\tau) \times \mathcal{B}(\tau_{\text{lep}}) = 0.2535,$$

[1] In the following, the observed values of decay lengths and branching fractions are taken from [8]. Values calculated from these numbers are shown with significant digits according the the rounding scheme described therein.

while in turn the branching fraction to τ_{had} is

$$\mathcal{B}(W \to \tau_{\text{had}}) = \mathcal{B}(W \to \tau\nu_\tau) \times \mathcal{B}(\tau_{\text{had}}) = 0.0737.$$

Considering only the branching fractions of the W bosons, i.e. for processes with only one W boson as W+jets or ZW, these processes contribute with a factor of

$$\frac{\mathcal{B}(W \to \ell\nu)}{\mathcal{B}(W \to \tau_{\text{had}})} = \frac{0.2535}{0.0737} = 3.44$$

more events with one real light lepton than with a real τ_{had}.

In the case of the $t\bar{t}$ process (and all other processes involving two W bosons), the relative difference in contributions to the lep-had and had-had channel can be estimated from the branching fractions:

$$\frac{\mathcal{B}(t\bar{t} \to \ell\nu\,\tau_{\text{had}})}{\mathcal{B}(t\bar{t} \to \tau_{\text{had}}\,\tau_{\text{had}})} = \frac{2 \times \mathcal{B}(W \to \ell\nu) \times \mathcal{B}(W \to \tau_{\text{had}})}{\mathcal{B}(W \to \tau_{\text{had}}) \times \mathcal{B}(W \to \tau_{\text{had}})} = 6.88$$

Processes containing W bosons contribute in general significantly more to the lep-had than to the had-had channel, while processes as Z+jets do only contribute to real tau-lepton pair production.

3.3. Pile-Up

The number of events of interest depends on the number of collisions happening in the data-taking period (for more details cf. Section 3.4). The spacing of bunches in time is on the other hand limited by machine parameters (cf. Section 3.1), therefore multiple collisions are allowed to affect the detector simultaneously. The mean number of interactions per bunch crossing is denoted as μ, and the average over all bunches is referred to as average mean number of interactions per bunch-crossing ($\langle\mu\rangle$) [48]. This is commonly referred to as pile-up and discriminated as in-time and out-of-time pile-up. They are important for analyses, since these additional events will create irreducible overlap with the event of interest.

In-Time Pile-Up

In-time pile-up describes multiple interactions during one bunch-crossing. Partons of every proton of the bunch can potentially interact and the centre-of-mass energy of the interactions can vary a lot (cf. also Section 3.1). Depending on the analysis not all interactions will be of interest. As long as the individual interactions can be resolved by the detector, the interaction of interest can be isolated and studied separately (cf. Section 4.6).

Figure 3.8 (a) shows the peak of the mean number of interactions per bunch-crossing at the start of every run in the year 2016 as a function of time. It can be seen that LHC was increasing the peak number of interactions per bunch-crossing over the year and with that the in-time pile-up. Most of the runs had their peak mean number of interactions per bunch crossing in a range from 20 to 45.

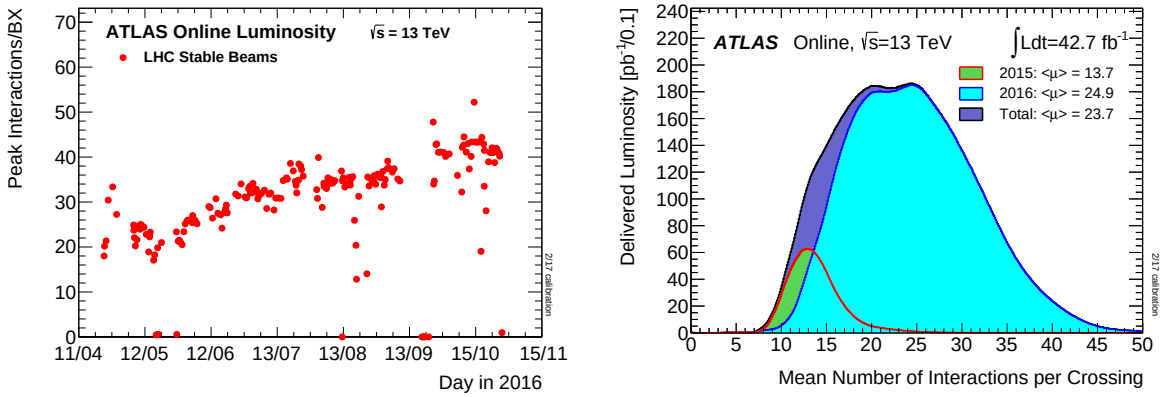

(a) Peak number of interactions per bunch crossing for each run as a function of time in the year 2016.

(b) Mean number of interactions per bunch crossing for 2015 and 2016 (and the combination thereof).

Figure 3.8.: Number of interactions per bunch crossing recorded with ATLAS [49].

Out-Of-Time Pile-Up

The second important source of pile-up is the so-called out-of-time pile-up. It originates from the preceding or following bunch-crossing and influences the detectors due to read-out electronics integrating over a longer time than the 25 ns bunch spacing or detectors being inherently sensitive to several bunch crossings.

Figure 3.8 (b) shows the average mean number of interactions per bunch-crossing. It is used to estimate the contribution of out-of-time pile-up.

3.4. Luminosity

For the evaluation of the performance of a collider in a process-independent way, it is useful to introduce the luminosity $\mathcal{L}$. It is defined as

$$\mathcal{L} = \frac{\mathrm{d}N}{\mathrm{d}t}\frac{1}{\sigma},$$

where σ is the cross section of the process of interest and $\frac{\mathrm{d}N}{\mathrm{d}t}$ the rate of this process [8]. The luminosity can be measured with a suitable process and then applied to other processes.

The instantaneous luminosity can also be expressed in terms of the machine parameters: number of bunches n_b, intensity of the bunches N_1, N_2, the transverse beam sizes σ_x, σ_y, the revolution frequency f_{rev}, and a geometrical correction factor F accounting for the collisions not being head-on:

$$\mathcal{L} = \frac{N_1 N_2 n_b f_{\mathrm{rev}}}{4\pi\,\sigma_x \sigma_y} F \tag{3.1}$$

The total integrated luminosity L is a convenient quantity for expressing the amount

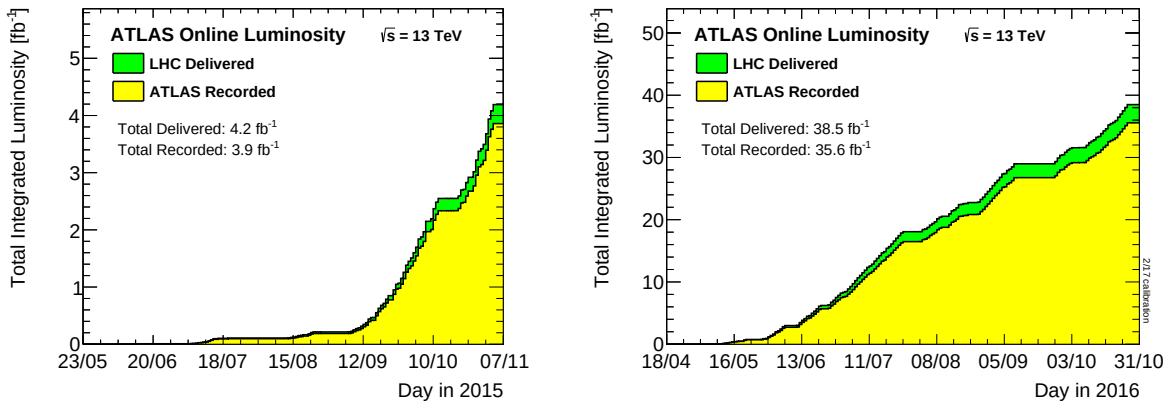

(a) Total integrated luminosity in 2015.

(b) Total integrated luminosity in 2016.

Figure 3.9.: Total integrated luminosity used in the presented analysis [49]. The green diagram shows the measured luminosity as delivered by the LHC. The yellow diagram shows the luminosity actually recorded by ATLAS.

of data produced. It is defined as

$$\mathrm{L} = \int_{\Delta t} \mathcal{L}\,\mathrm{d}t,$$

where Δt is the time interval considered. Figure 3.9 shows the total integrated luminosity produced and recorded by ATLAS in the years 2015 and 2016. The number of events of a certain process with cross section σ_p can be calculated as:

$$N = \mathrm{L}\,\sigma_p$$

In 2016 the LHC went beyond its design luminosity of 10×10^{33} cm^{-2}s^{-1} and delivered a peak luminosity of 13.8×10^{33} cm^{-2}s^{-1} or about 0.05 $\frac{\mathrm{fb}^{-1}}{\mathrm{h}}$ [41, 49].

Measurement

A precise knowledge of the integrated luminosity is needed to determine the normalisation of the SM background processes and to be able to set exclusion limits on the observed cross section. The luminosity is measured with similar methods as described in [50]. The basic principle is to measure the bunch luminosity $\mathcal{L}_b$ (corresponding to the luminosity of two single colliding bunches) given by

$$\mathcal{L}_b = \frac{\mu_{\mathrm{vis}}\, f_{\mathrm{rev}}}{\sigma_{\mathrm{vis}}},$$

where μ_{vis} is the visible fraction of the pile-up parameter μ and σ_{vis} is the corresponding visible cross section.

μ_{vis} can be measured with dedicated detectors, such as the forward Cherenkov-detector LUCID [51]. It is located in the forward directions ($5.6 < |\eta| < 6.0$) and detecting

inelastic proton-proton collisions and has a known model to infer μ_{vis} from the measured hits in the detector (cf. [50]).

In order to measure the luminosity, the visible cross section σ_{vis} needs to be determined. In special van der Meer (vdM) runs, the LHC is operated with well-known machine parameters (e.g. an especially low number of interactions per bunch crossing) and a sophisticated measurement scheme as described in [50] is used to determine the luminosity in a similar manner as sketched in Equation (3.1). Using the vdM scanning routine, σ_{vis} can be determined for the detector used for luminosity determination.

The detectors are calibrated to the absolute luminosity scale using the vdM runs. During regular runs, the measured luminosity is therefore an extrapolation from the vdM runs and the calibration deteriorates over time. The vdM scans used for the luminosity determination were performed in August 2015 and May 2016.

4. ATLAS Detector

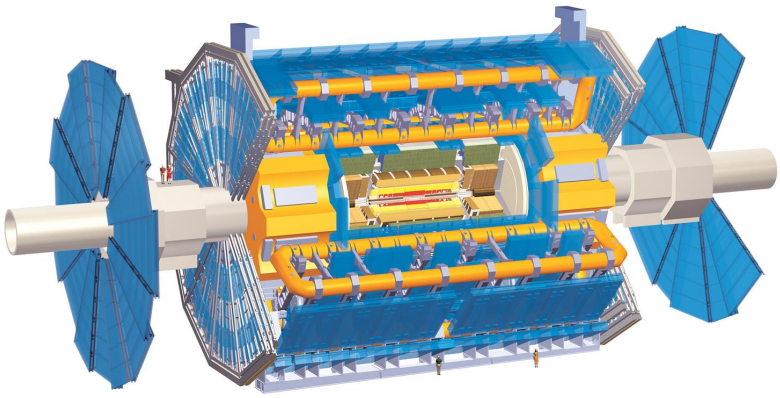

Figure 4.1.: Computer-generated image of the ATLAS detector [52]. The humans in front of the detector are to scale.

4.1. Overview

The ATLAS detector is a multi-purpose particle detector located at the interaction point 1 of the LHC, designed to cover most of the solid angle. Its main purpose is to precisely identify and measure SM particles for a variety of physics cases accessible with the collisions provided by LHC. A full description of the design of ATLAS is given in [51] and details relevant to the analysis are presented here.

In the following, a short introduction into the design and working principle of the detector and the reconstruction of particles and jets is given. The detector consists of three main parts, going from the interaction point (IP) to the outside of the detector: the inner tracking, the calorimeters, and the muon system (MS). The inner tracking detector and the MS are used for momentum measurements, while the calorimeters measure the energy of the particles. The combination of the information of all three parts is the key to particle identification.

The overall structure can be seen in Figure 4.1. The central part (also called barrel) has a cylindrical shape around the beam pipe. The so-called end caps adjoin in both directions of the beam pipe to the barrel.

Coordinate system

The ATLAS detector uses a right-handed coordinate system with the x-axis pointing towards the centre of the LHC, the y-axis pointing upwards to the surface and the z-axis along the beam pipe. The origin of the coordinate system is the nominal IP. The azimuthal angle ϕ is defined in the x-y (transverse) plane, while the polar angle θ indicates the distance from the beam pipe. The rapidity is defined as

$$y = \frac{1}{2} \ln \left(\frac{E + p_z}{E - p_z} \right), \tag{4.1}$$

yielding invariant rapidity differences when performing Lorentz boosts in z-direction [8].

Pseudorapidity (η) is the high-energy ($p \gg m$) approximation of the rapidity and defined as

$$\eta = -\ln \tan \left(\frac{\theta}{2} \right), \tag{4.2}$$

and coincides with the rapidity for (effectively) massless particles. It has the advantage of being independent of the energy and momentum calibration of the objects and gives a one-to-one correspondence to the geometrical angle θ:

$$\sinh \eta = \cot \theta$$

Distances of objects (assuming the same origin) are given in terms of the geometrical distance

$$\Delta \mathrm{R} = \sqrt{(\Delta\eta)^2 + (\Delta\phi)^2}. \tag{4.3}$$

Due to the unknown boost in z-direction, many physics quantities as e.g. energy and momentum are projected on the transverse plane, which is indicated by a sub-script "T" (E_T, p_T). The relation between Cartesian coordinates and the ATLAS coordinate system is given by

$$p = \begin{pmatrix} E \\ \boldsymbol{p} \end{pmatrix} = \begin{pmatrix} E \\ p_x \\ p_y \\ p_z \end{pmatrix} = \begin{pmatrix} \sqrt{\boldsymbol{p}^2 + m^2} \\ p_\mathrm{T} \cos\phi \\ p_\mathrm{T} \sin\phi \\ p_\mathrm{T} \cot(\theta) \end{pmatrix} = \begin{pmatrix} \sqrt{\boldsymbol{p}^2 + m^2} \\ p_\mathrm{T} \cos\phi \\ p_\mathrm{T} \sin\phi \\ p_\mathrm{T} \sinh(\eta) \end{pmatrix}. \tag{4.4}$$

Three-dimensional vectors use a bold font ($\boldsymbol{p}$), while Lorentz vectors are set in regular font (p).

Magnetic Fields

The setup of magnetic fields in the detector is an integral part for the measurement of the momenta of charged particles. If a charged particle moves perpendicular to the field lines of a magnetic field, it is forced on a bent track due to the Lorentz force. Given precision position measurements along the track, the curvature can be measured. From the curvature the charge-to-momentum ratio q/p can be inferred. For the particles of interest for this analysis a hypothesis of $q = \pm 1$ can be applied. Therefore, the two detector parts providing momentum measurements are embedded into magnetic fields.

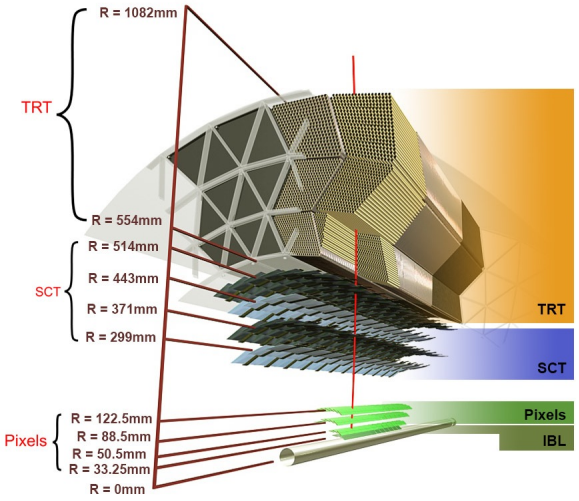

Figure 4.2.: Sketch of the ID of ATLAS [53]. Distances to the centre of the beam pipe are given in mm.

The inner tracking is surrounded by a solenoid magnet providing a magnetic field of 2 T in direction of the beam axis. The solenoid has superconducting windings and is designed to have a low material budget since it is located inside the calorimeters.

Outside of the calorimeters a toroidal magnetic field is provided by super-conducting coils. One system is used for the barrel part and two more are located in the endcaps. They provide the fields necessary to enable the momentum determination in the MS.

4.2. Inner Tracking

The inner detector (ID) consists of three sub-systems. The two innermost systems, the pixel and silicon-strip detectors are tracking detectors with high position resolution, while the Transition Radiation Tracker (TRT) provides additional identification power for electrons. Figure 4.2 shows a cut-away drawing of the ID sliced in the transverse plane to illustrate the dimensions and locations of the sub-detectors.

The silicon pixel detectors are the innermost detector layers particles traverse after exiting the beam pipe. There are — after the inclusion of the Insertable B-Layer (IBL) at the beginning of Run 2 (cf. [54]) — 4 layers of pixel detectors with a position resolution in $r-\phi$ (z) direction of the order of 10 (100) μm [51]. They are cooled to reduce the stochastic noise and designed to endure the high radiation environment close to the interaction point. They are able to cope with the high rates achieved with LHC without significant dead times.

The Semiconductor tracker (SCT) modules are silicon strip detectors with a high resolution orthogonal to the strip direction and a lower resolution parallel to the strips. Two strip detectors are glued back-to-back at a small angle of 20 mrad between the strips to increase the resolution. The accuracy is about 17 (580) μm in $r-\phi$ (z) direction [51].

The largest of the three sub-detectors is the TRT. It consists of drift tubes of 4 mm in diameter, filled with a gas mixture providing a different index of refraction than

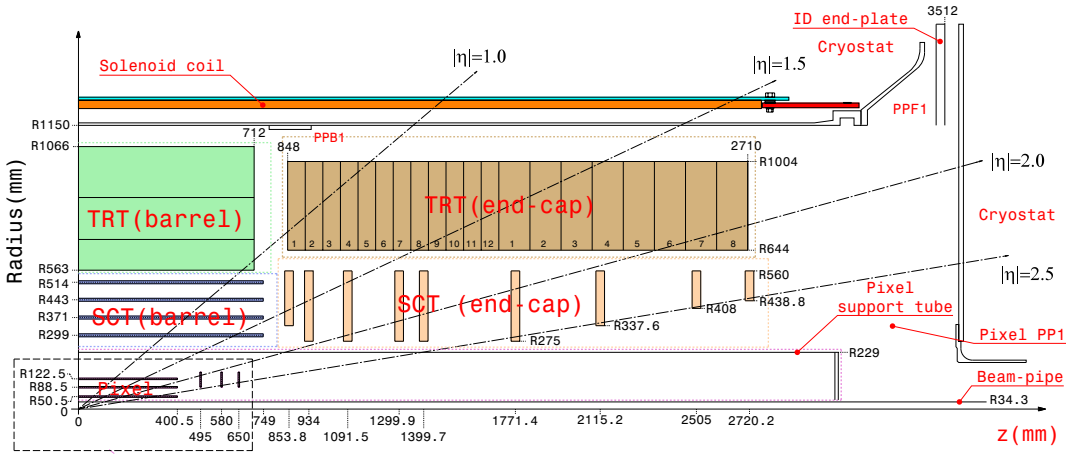

Figure 4.3.: Sketch of one quarter of the ID of ATLAS listing distances and locations of the single sub-detectors [51]. Pseudorapidities as originating from the IP are overlayed to illustrate the coverage.

the surrounding material of the drift tube. Upon traversal, charged particles give rise to transition radiation. The energy losses of a particle due to transition radiation are proportional to the Lorentz factor γ [55]. One of the main purposes of the TRT is to discriminate electrons from pions. For the same momentum pions will have, due to the much higher mass, a lower value of γ and therefore emit less transition radiation. The number of TRT hits recorded and assigned to a track is used as a discriminating variable. It also provides additional track points, which are especially useful for the extrapolation of tracks to the MS.

Each of the three sub-systems provides tracking information in the form of hits located in three-dimensional space. These can be combined to form a track, which, as described above, in combination with the knowledge of the magnetic field gives a momentum and charge measurement. Furthermore, non-prompt decays of particles are an important information for particle identification. High precision track information is therefore essential to find displaced vertices arising from short-lived (order of $c\tau = 100$ μm) particles.

Figure 4.3 shows a schematic map of the ID components in the r-z plane and how the barrel and end-cap tracking detectors overlap to ensure good coverage in pseudorapidity. The coverage of the high-precision tracking detectors extends up to a pseudorapidity of $|\eta| < 2.5$, resulting in the geometrical limit for track-based particle identification.

4.3. Calorimetry

Surrounding the precision tracking and solenoid magnet, the calorimeters are located. Their primary goal is a measurement of the energy of particles by absorbing them completely. ATLAS employs sampling calorimeters, which alternate scintillating with absorbing layers. The absorbing layers let the particles undergo drastic energy losses and force them to build up showers of particles. In case of electromagnetically interacting particles, bremsstrahlung and pair-production processes dominate, while coloured

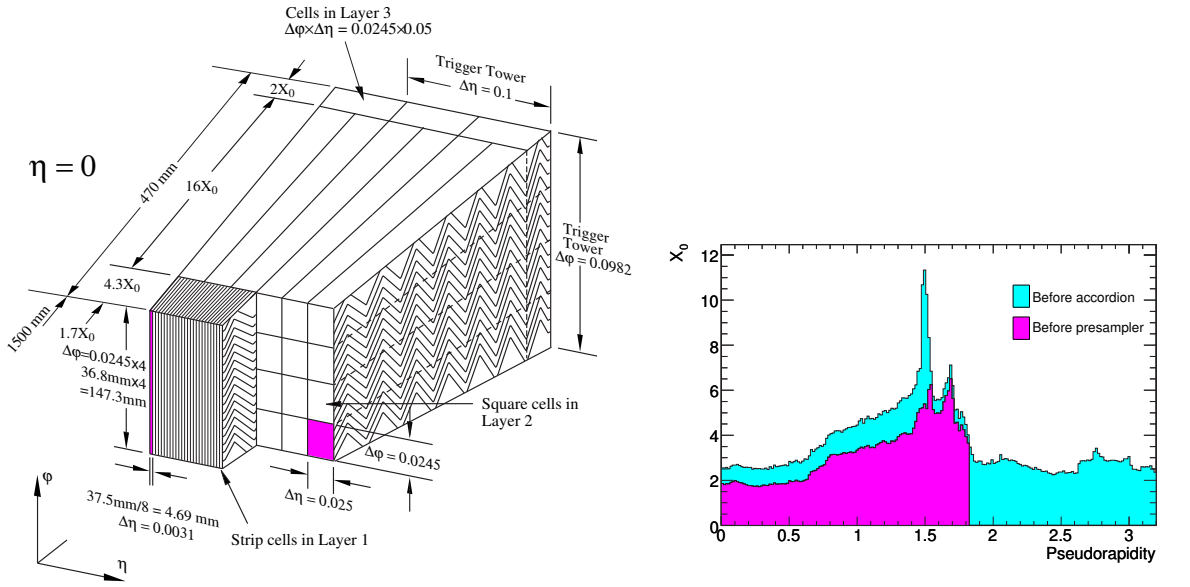

(a) Schematic view of a ECal barrel module with segmentations in η and ϕ nad the corresponding radiation lengths.

(b) Cumulative amount of material in units of radiation lengths in front of the calorimeters in dependence of η.

Figure 4.4.: Properties of the ECal [51].

particles mostly undergo various inelastic processes of the strong interaction. The scintillating layers on the other hand record the intensity and shape of the showers, allowing to reconstruct the energy loss.

Two different calorimetric systems are discriminated in ATLAS: the electromagnetic calorimeter (ECal) and the hadronic calorimeter (HCal). The purpose of the ECal is to absorb light, electromagnetically-interacting particles, while the HCal absorbs the remaining hadronically interacting particles with significantly more material.

The technology used for the ECal is based on liquid argon (LAr) as scintillating material. It fills the gaps of an accordion-shaped array of lead absorbers. A LAr layer, called the presampler, is located in front of the sampling calorimeters. It provides a finely segmented first signal with a position resolution of $\Delta\eta \approx 0.025$ and $\Delta\phi \approx 0.1$. The three layers following in radial direction are organised such that the first one has a fine segmentation in pseudorapidity ($\Delta\eta = 0.0031$) and a coarser segmentation in azimuthal angle ($\Delta\phi = 0.098$), providing a precise measurement of η. The second layer is designed to contain most of the electromagnetic showers. It has the highest number of radiation lengths in depth and is similarly fine segmented in $\Delta\eta$ (0.025) and $\Delta\phi$ (0.0245). The third layer just contains the tails of the showers and is more coarsely segmented ($\Delta\eta = 0.05$, $\Delta\phi = 0.0245$). A sketch of one of the barrel modules is illustrated in Figure 4.4 (a).

A special region worth noting is the so-called transition region between the barrel ECal and the ECals in the end-caps. A high material budget is found in the pseudorapidity region $1.37 < |\eta| < 1.52$. The total material in front of the calorimeter is shown in Figure 4.4 (b). Therefore, this region is excluded for particles relying on very precise

calorimeter measurements and a lower reconstruction efficiency is expected in this region in general.

The HCals are also sampling calorimeters. In the barrel region they employ steel absorbers alternating with scintillating tiles made of doped polystyrene. Their depth is chosen to absorb almost all particles remaining after traversal of the ECal, which mostly are particles carrying colour charge. Muons and neutrinos are the only particles expected to escape the HCal, due to their small (or zero) interaction with the detector material.

In the end-caps the HCal also relies, on LAr as scintillator, but the absorbers are made of copper. The coverage up to $|\eta| < 4.9$ is finally completed with the forward calorimeters.

4.4. Muon Spectrometer

Surrounding the calorimeters, the MS is located within the toroidal magnet field. Precision tracking is used to identify and measure muons.

Figure 4.5 shows the layout of the muon chambers in the r-z plane. The precision tracking information is obtained with Monitored Drift Tube (MDT) chambers. They consist of an array of drift tubes with a dedicated position monitoring yielding an average resolution of about 35 μm per chamber. They cover the pseudorapidity range up to $|\eta| < 2.7$, exception for the innermost layer in the forward region $2.0 < |\eta| < 2.7$, which is equipped with Cathode Strip Chambers (CSCs). CSCs are multiwire proportional chambers, capable of the high rates in this forward region.

ATLAS employs dedicated chambers (Resistive Plate Chambers (RPCs) and Thin Gap Chambers (TGCs)) in the MS to trigger on events containing muons. These will be explained in the next section.

4.5. ATLAS Trigger System

The event rates delivered by LHC are enormous. At a bunch spacing of 25 ns up to 40 million collisions per second can occur, with each event having an average size of about 1.3 MB [51]. This amounts to a data rate of up to 50 TB/s. This is impossible to read out and impossible to permanently save with current technology. Many events produced by LHC collisions are soft hadronic interactions, which are not part of the primary physics case of the LHC programme. Thus, a selection of the events to be read out and recorded needs to be employed, which is called triggering.

Key components of the trigger decision are detectors which can be read out fast and yield the information necessary to do a tentative decision on the selected signature. ATLAS uses a hardware-based trigger system (L1) relying on coarse information of the calorimeters and the dedicated chambers in the MS, which is combined by the central trigger processor.

The MS uses two different technologies for dedicated trigger chambers in order to provide a sufficiently fast identification of bunch crossings of interest. In the barrel region ($|\eta| < 1.05$) RPCs are used. RPCs are gaseous detectors with an operating gas

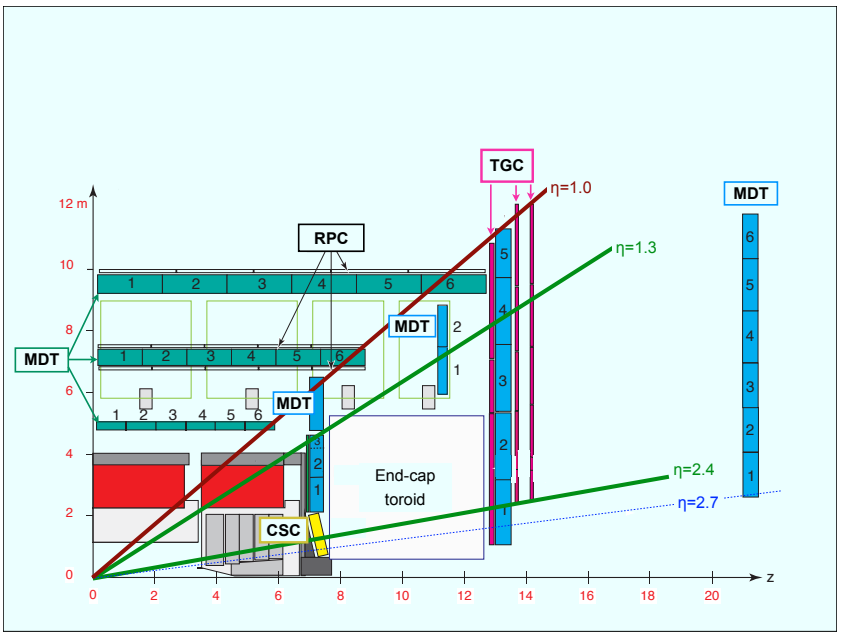

Figure 4.5.: Location of chambers in the MS [56].

mixture confined between two resistive plates, separated 2 mm by insulating spacers. The read-out is achieved with capacitively coupled metallic strips on both resistive plates, one in ϕ-, the other in η-direction. The RPCs are mounted on the MDTs in the barrel as indicated in Figure 4.5.

The end-caps are equipped with three layers of TGCs. These are multi-wire proportional chambers with very good timing information. The wires are aligned in the radial direction to give a good momentum resolution within the toroidal field and the read-out strips add azimuthal information. As shown in Figure 4.5, they are sandwiched on the middle wheels of ATLAS.

After the hardware-based decision, the event information is passed to the High-Level Trigger (HLT), a small server farm. There, the information from all detector components is available and more sophisticated algorithms can be run to get a more precise information on the event.

The triggers relevant for this analysis are lepton triggers and triggers on the momentum imbalance in the transverse plane. Electron triggers use calorimeter information for the L1 decision, which is refined at the HLT with tracking information. Triggers for muons use information from the dedicated chambers described above at L1 and complement that in the HLT with information from the MDTs and the inner tracking [56]. Hadronically-decaying-tau triggers take energy and isolation information for the L1 decision from the calorimeters and run an offline-like selection [57] at the HLT which is described in detail in Sections 4.6 and 5.3. The momentum balance is calculated at L1 from the energy deposited in calorimeter towers [58], i.e. muons are not properly included and can lead to a large imbalance. In the HLT, several algorithms are run to calculate the momentum imbalance. In the analysis presented here, it is calculated as the negative vectorial sum of the sum of the transverse momenta of jets. The algorithm

additionally uses a pile-up subtraction scheme (cf. "mht" in [59]).

4.6. Object Reconstruction

The recorded signals of the detector need to be interpreted in order to be useful for analyses. Candidates for so-called physics objects, which in this analysis comprise electrons, muons, taus, photons, and jets, are reconstructed with specialised algorithms and are preliminarily calibrated. These algorithms are developed using the knowledge of the detector signatures and are improved with the help of simulated samples of well-known physics processes, where the simulated detector signals (cf. Section 5.2) can be compared to the physics objects provided for the simulation. The reconstruction only provides candidates for the physics objects, and the object definitions will be refined with additional identification requirements in Section 5.3.

Primary Vertices

Tracks are combined into vertices during the reconstruction step. Tracks with $p_{\mathrm{T}} > 400$ MeV and $|\eta| < 2.5$ are considered for building a primary vertex (PV) if they fulfil the following quality requirements [60]: at least 9 (11) hits in the silicon tracking in the range of $|\eta| < 1.65$ ($|\eta| > 1.65$) and at least one hit in the IBL and second pixel layer. No holes[1] for the pixel detectors and a maximum of one hole in the SCT. Not more than one shared module, i.e. one shared hit[2] in a pixel module or two shared hits in an SCT module.

Vertices are built using the "Iterative Vertex Finding" approach [61]. The number of primary vertices (N_{PV}) is used to quantify the pile-up within one bunch-crossing (cf. Section 3.3). The leading PV is defined as the vertex with the highest Σp_{T}^2 of all associated tracks. It is assumed to be the centre of the so-called hard interaction.

Jets

Due to their colour charge, quarks and gluons can only traverse the detector in a colourless state by acquiring additional colour-charged particles, the so-called hadronisation. These states react heavily with the detector material giving rise to showers of energy deposits, especially in the calorimeters where the material is most dense. Since single-particle identification would be very challenging and is not feasible with current technology, the notion of jets is introduced: a cluster of calorimeter deposits with corresponding tracks to be further interpreted by the analyses.

Jets are the most basic collection of objects built from tracks and calorimeter deposits. They serve as a detector-level description of quarks and gluons, but are also used as seeds for the reconstruction of electrons and taus. The anti-k_t algorithm [62] is used to cluster calorimeter deposits of jets with a radius paramter of $R = 0.4$. One of its main advantages is that it is an infrared- and collinear-safe algorithm. Infrared safety means

[1] A hole is a missing hit in the extrapolated track, given that the expected hit is in the active material of the detector.

[2] A shared hit is a hit used by more than one reconstructed track.

that the jet definition, i.e. the individual jets which are reconstructed from a certain event, does not change with the addition of a soft emission to one of the final-state particles. Collinear safety on the other hand is the stability of the jet definition when splitting one of the final-state particles into two collinear components. Since these two processes are very hard to model precisely in QCD, the stability of the jet definition with respect to both of them ensures that small changes in the simulation do not significantly change the reconstructed jets.

Topologically connected calorimeter deposits which are significantly above noise threshold are clustered into so-called *topo-clusters* [63]. Tracks are associated to the calorimeter jets using ghost-matching, a procedure where tracks with infinitesimal p_{T} are added to the clustering process, and if they are picked up in the clustering algorithm the track is associated to the jet (cf. also [64]). The ghost-matching is only applied for jets completely contained in the ID ($|\eta| < 2.1$) [65].

To calibrate the jets several steps are executed [66]. A pile-up correction depending on N_{PV}, $\langle\mu\rangle$, and the median p_{T} density of the jets in the event (ρ) is applied. The p_{T} density is defined as p_{T}/A, where the active area A of a jet is determined with the ghost association procedure [64]. The correction is applied to the reconstructed p_{T} ($p_{\mathrm{T}}^{\mathrm{reco}}$) using two parameters α and β determined on MC simulated samples:

$$p_{\mathrm{T}}^{\mathrm{corr}} = p_{\mathrm{T}}^{\mathrm{reco}} - \rho A - \alpha(N_{PV} - 1) - \beta\langle\mu\rangle$$

The jet energy scale is calibrated to match the "true" jet energy, i.e. the energy of a jet simulated with a MC generator. The η direction of the jets is also calibrated to match their "true" value.

Variables sensitive to the calorimeter response of the jets are used in the *global sequential correction* scheme [67]. The corrections account for the non-compensation of the calorimeters[3], in-active or out-of-acceptance areas and the flavour of the parton initiating the jet.

To account for the residual differences between data and MC, an in-situ correction in dependence of p_{T} and η is applied to the p_{T} of each jet.

Muons

As muons of interest are usually in the p_{T} regime of minimal ionisation (cf. chapter 33 in [8]), they are not stopped in the calorimeters and therefore leave tracks in both the ID and the MS. Since they are the only charged particles to reach the MS and to leave tracks there, this gives rise to a unique signature.

Muons are reconstructed from their tracks in the ID and the MS. The ID tracks are built as for all other charged particles, and in the MS, tracks are fitted through all layers of traversed detectors. Two types of track combination schemes are used in this analysis. For so-called "combined muons", the tracks from the independent fits in the ID and MS are combined in a global fit. The "extrapolated muons" only use the MS track and impose a loose requirement on compatibility with originating from the IP.

[3]Non-compensation describes calorimeters responding differently to electromagnetic and hadronic showers.

Electrons

Due to their small mass, electrons are absorbed in the ECal. In combination with their track in the ID, they have a clear signature but still need to be distinguished from other charged particles showering in the calorimeters as e.g. pions.

Electrons are reconstructed from tracks matching energy deposits in the ECal. Starting from the depositions in the ECal, tracks are fitted and tested if they are compatible with the barycentre of the ECal deposits. If a track matching to the ECal depositions is found, an electron candidate is defined and re-fitted with a dedicated algorithm.

Taus

Tau leptons in their hadronic decay modes (τ_{had}) have similar detector signatures with electrons and jets, making them an interesting field of study. Taking away the 35.2 % leptonically decaying tau leptons, the remaining hadronically decaying tau leptons have a rich phenomenology of 1 (3 or 5) charged particles in the decay, also called 1-prong (3- or 5-prong), with total branching fractions of $(50.03 \pm 0.06)\,\%$ ($(15.21 \pm 0.06)\,\%$ or $(0.99 \pm 0.04)\,\%$). Even more possibilities arise when considering additional neutral particles [8]. The sophisticated reconstruction procedure is described in the following.

The jets used as seeds for the reconstruction of τ_{had} are anti-k_t jets contained in the inner tracking ($|\eta| < 2.5$) with a distance parameter of $\Delta\text{R} = 0.4$ and at least 10 GeV of p_{T} [68]. The p_{T} of the seeds is set to the local hadronic calibration scale [69] of the topo-clusters within a cone of $\Delta\text{R} < 0.2$.

For each τ_{had} the corresponding primary vertex (called tau vertex) is determined by summing the p_{T} of the τ_{had} candidate tracks of the jet seed ($\Delta\text{R} < 0.2$) — the PV matching the largest fraction of the p_{T} sum is chosen as the tau vertex. The tau vertex association in combination with impact parameter cuts increases the reconstruction efficiency for low-p_{T} τ_{had} and τ_{had} in events with large pile-up.

An important property of hadronic decays of the tau leptons is the number of charged tracks associated (*prongness*). Reconstruction and identification (as well as mis-identification) of the visible part of the τ_{had} ($\tau_{\text{had-vis}}$) have differing efficiencies in dependence of the prongness. The selection of associated tracks is optimised to maximise the fraction of τ_{had} to be correctly reconstructed in the 1- and 3-prong category, respectively: the tracks have to have at least seven hits in the silicon tracking, of which at least two hits have to be in the pixel detectors. Furthermore, they should be contained in a cone of $\Delta\text{R} < 0.2$ around the $\tau_{\text{had-vis}}$ direction and have a p_{T} of at least 1 GeV. Finally, the impact parameters with respect to the tau vertex should be $|d_0| < 1.0$ mm in the transverse plane and $|\Delta z_0 \sin\theta| < 1.5$ mm in the longitudinal direction.

Figure 4.6 (a) shows the reconstruction efficiency of 1- and 3-prong τ_{had} as a function of their true p_{T}. The main reasons for taus not being reconstructed are the track and vertex selection criteria. Figure 4.6 (b) shows the number of reconstructed tracks associated to a tau candidate for 1- and 3-prong τ_{had}. Tracking inefficiency can lead to an underestimation of the number of reconstructed tracks, while overestimation can originate from photon-conversion tracks passing the track selection criteria.

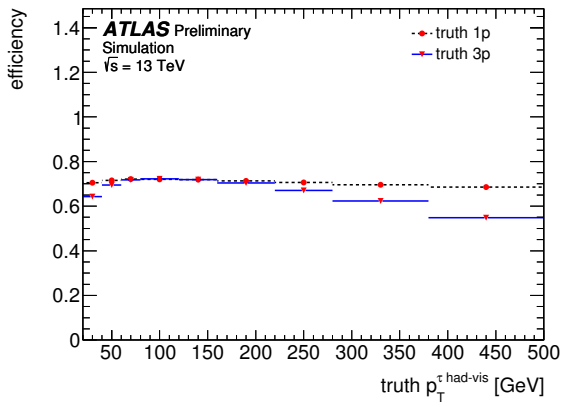

(a) Reconstruction efficiency as a function of the true p_{T} of the $\tau_{\text{had-vis}}$ candidate for 1- and 3-prong taus.

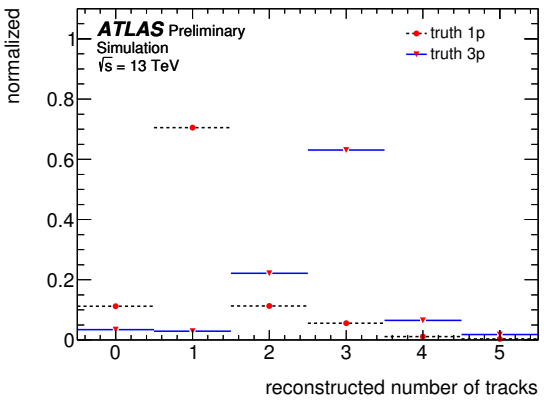

(b) Distribution of the reconstructed number of tracks for 1- and 3-prong taus.

Figure 4.6.: $\tau_{\text{had-vis}}$ reconstruction performance in MC simulation [68].

Photons

Photons are of minor interest for the presented analysis, since they are only used in the calculation of the missing transverse energy ($E_{\mathrm{T}}^{\mathrm{miss}}$) (cf. Section 5.3). Their reconstruction is based on showers in the ECal and either no associated tracks or tracks consistent with a photon conversion to an electron-positron pair in the ID are required [70].

5. Analysis

In the following chapter the analysis to be submitted to Physical Review D will be described. This analysis supersedes preliminary results made public for the ICHEP conference 2016[1] with the dataset collected in the year 2015, but only a part of the dataset collected in the year 2016 [2]. The preliminary ICHEP analysis is only discussed where it is helpful to motivate the analysis strategy, since otherwise the analysis setup has been further developed and the had-had channel has been included. Preliminary results of the analysis presented here have been made public for the SUSY17 conference[2] with the full 2015 and 2016 dataset. The results are described in a conference note [3] and are in preparation for the submission to the journal. As discussed in Section 2.3.2, the simplified model studied here has already been targeted in an analysis carried out with Run 1 data. The Run 1 analysis serves as starting point for the analysis presented here, but the full setup was developed and validated independently.

In the first part of the analysis chapter, the necessary analysis ingredients and the background estimation will be introduced. For the motivation of the design of the regions the plots and tables will not show the observed data. One signal benchmark point will be used in the plots and tables, showing the simulated signal sample at $m_{\tilde{t}_1} = 1100$ GeV and $m_{\widetilde{\tau}_1} = 590$ GeV (with shorthand notation $m_{\tilde{t}_1} = 1100, m_{\widetilde{\tau}_1} = 590$). All signal points considered and the observation will be presented along with the final results in Section 5.9.

5.1. Dataset Recorded

The data for this analysis was recorded with the ATLAS detector in the years 2015 and 2016. As described in Section 4.5, not all collisions are recorded, but events of interest selected with a trigger. Furthermore, basic quality requirements are applied to the dataset.

Trigger

The trigger system in ATLAS allows running triggers which will not cause every event they fired to be written out, but will randomly discard events (pre-scale). In the presented analysis only triggers, which do not cause discarding of events, are used in order to make use of the full dataset and to avoid additional biases. The different triggers are presented in Section 5.5.1 and the impact on the analysis discussed there.

[1] The website of the ICHEP 2016 conference can be found here: `https://www.ichep2016.org/`
[2] The website of the SUSY17 conference is found here: `http://www.tifr.res.in/~susy17/`

Data Collected

If the ATLAS detector is known not to be ready to take data or subdetectors misbehave, the corresponding lumi blocks (parts of a run of the order of a minute) are saved to a list and are later on not used in analyses. Therefore, the total recorded data (as outlined in Section 3.4) is calculated only for the "good" lumi blocks.

Event Cleaning

Data collected with the ATLAS detector needs to fulfil basic quality requirements in order to be considered for physics analyses. The following selection criteria are used:

- If subsystems essential for proper reconstruction are offline or report too many errors, events are not used.
- Events are rejected if one of the reconstructed muons is compatible with originating from a cosmic shower. Muons originating from cosmic showers are identified by requiring them to have a longitudinal impact parameter $|z_0| <$ mm and a transverse impact parameter $|d_0 < 0.2|$ mm with respect to the leading PV.
- If an event has a badly measured muon it is rejected. To assess the quality of the measurement, the magnitude of the relative charge-momentum measurement uncertainty is used:

  $$\sigma^{\text{rel}}_{q/p} = \left| \frac{\sigma(q/p)}{q/p} \right|$$

  If for any muon in the event, the charge-momentum ratio $\sigma^{\text{rel}}_{q/p}$ exceeds 0.2, or the ratios of $\sigma^{\text{rel}}_{q/p}$ from the ID or MS measurement with respect to the combined track measurement are smaller than 0.8, the event is rejected.
- All events are required to have at least one reconstructed PV.
- If an event has jets that do not pass the *loose* working point (WP) as defined in [71], it will be rejected. This WP is designed to reject events with unusually large calorimeter deposits, as e.g. from beam-induced backgrounds from proton interactions upstream of the interaction point, cosmic showers, or noise bursts from the calorimeters themselves.

5.2. Simulated Data

Simulated samples play a crucial role for understanding and interpreting the data collected. The signal and SM expectation can be quantified and data-based background estimations performed. The general procedure for simulating samples is described in the following, whereas the detailed description of the software employed can be found in [72].

Calculation of the Physics Process

In the first step, the matrix elements for the process under consideration are calculated up to a selected order in perturbation theory. Additional quarks and gluons may be included into the matrix elements to get a better description of additional QCD radiation. The resulting amplitudes are then sampled over the whole phase space with MC methods, taking into account the PDF (cf. Section 3.1) of the initial proton–proton collision. Finally, dedicated algorithms (the so-called "showering") are run to semi-empirically model the hadronisation of coloured final-state particles.

Detector Simulation

The previous steps create an intermediate sample containing the predictions by the respective theory and describe the expected final states and the distribution of the corresponding four-momenta. In order to compare these samples with data collected with the ATLAS detector, it is necessary to run a software simulating the detector response. The simulation relies on the software package GEANT4 [73] to simulate the interactions of the particles with the detector. The positions of the subdetectors, the material budget, and the magnetic field strengths are modelled precisely to allow for an accurate simulation of the interactions and paths of the particles. Finally, the simulation output is saved in the form of so-called hits — the information of the energy depositions in the different detector components along with information on position and time [72].

In addition, particles deemed relevant for analyses are retained with their original values from the process generation. They are saved alongside with the simulation information as so-called "truth" information. They allow to assess the reliability of reconstruction and to study the origin of reconstructed physics objects.

In the generation of pseudo-data the detector simulation is the step consuming most of the CPU-time. More than 90 % of the simulation time of an event in the full-simulation setup is spent simulating the calorimeter showers. Therefore, for some samples a fast simulation is used, which does not simulate the calorimeter showers with GEANT4 for every event. Instead, a library of showers for a wide range of momenta and pseudo-rapidities was calculated with GEANT4. The fast simulation uses these showers and significantly improves the time needed to simulate the detector response for one event [74].

Hits of additional interactions can be added to the simulated hard-scatter process in order to emulate the effects of pile-up. These minimum-bias events are generated with PYTHIA 8.186 using the MSTW 2008 PDF set [75] and the A2 tune [76]. Since the exact profile of $\langle\mu\rangle$ in the data observed might not be known at the time of generation of the simulated samples, each sample is reweighted to match the pile-up profile of the dataset considered. Since there is a difference between observation and simulation in the inelastic proton-proton cross-section measurement [77], the reweighting is done on a scaled $\langle\mu\rangle$ distribution. Uncertainties from the pile-up reweighting are derived by variation of this scaling factor.

The digitisation is the final step to make pseudo-data look like real data from the detector. It simulates the individual digital responses of the detectors to the hits provided. Activation thresholds but also the sampling of signal shapes over time is considered in

the digitisation. For each sub-detector dedicated software for digitisation of the hits is run, accounting for the differences of the respective technologies employed for detection and read-out.

Filtering and Reweighting

Simulating the pseudo-data is computationally very expensive. In general, the generators sample the phase space according to the differential cross section of interest. Analyses tend to target parts of the phase space with low contributions from SM-processes, e.g. high $E_{\mathrm{T}}^{\mathrm{miss}}$ or H_{T}. Since the steps after event generation require a lot of CPU-time, events can, based on certain filter criteria, be rejected before the simulation step. The filtering can be used to enrich the statistics in the phase space of interest, or to skip the generation of events irrelevant for the analysis altogether.

All samples are normalised to their predicted cross section, derived either directly from the matrix-element generator or from dedicated higher-order calculations. The effective MC luminosity, i.e. the luminosity where one event in data would on average correspond to one generated event in simulation, is calculated as

$$L_{MC} = \frac{N}{f\,k\,\sigma}, \tag{5.1}$$

where N is the number of generated events, f the efficiency of the potential filters, k higher-order corrections and σ the cross section of the generated process. MC generators may assign weights to individual events to prioritise parts of the phase space or to include higher-order corrections. Instead of the number of events, the sum of the event weights ($\sum w_i$), where w_i is the individual weight of event i, is used. The final, normalised weight is then given by

$$w_i^{\mathrm{norm}} = \frac{L}{L_{MC}} w_i = \frac{L\,w_i\,f\,k\,\sigma}{\sum w_i}, \tag{5.2}$$

where L is the integrated luminosity of the data sample considered.

After applying all these steps, the simulated samples are in an format equivalent to the data recorded by the detector. Simulation can be compared directly to the observation and the following steps, starting with the reconstruction, are run in the same way on the recorded data as on the simulated samples.

5.2.1. Signal Samples

The simplified signal model described in Section 2.3 was implemented to be run with the MadGraph5_aMC@NLO package [78]. It simulates the direct pair production of $\tilde{t}_1$, under consideration of the PDF set NNPDF2.3 LO [79], and the subsequent three-body decay $\tilde{t}_1 \to b\nu_\tau\widetilde{\tau}_1$. It is interfaced with Pythia [80, 81] and the ATLAS 2014 (A14) tune [82] for the remaining decays, hadronisation and parton shower, and the underlying event. Table 5.1 summarises the versions of the programs used for the simulation of the respective samples. Since the mass range covered by the signal grid was extended several times using different releases of the ATLAS software, the versions of the packages change slightly between different signal points.

The simplified model was constructed such that two parameters of interest can be varied independently. Since the branching fractions are set to 100 % and the mass of the $\tilde{G}$ is assumed to be very light, the two remaining parameters are $m_{\tilde{t}_1}$ and $m_{\tilde{\tau}_1}$. As already seen in Figure 2.12, the production cross section for the signal process decreases with increasing $m_{\tilde{t}_1}$. $m_{\tilde{\tau}_1}$ is always kinematically bound from above by $m_{\tilde{t}_1}$ and is varied for each value of $m_{\tilde{t}_1}$ in the range between the LEP limit (cf. Section 2.3.2) and the selected $m_{\tilde{t}_1}$. Figure 5.1 shows the points in the $m_{\tilde{\tau}_1}$-$m_{\tilde{t}_1}$ plane with the corresponding number of MC events generated for the simulated signal samples at each point. For large values of $m_{\tilde{t}_1}$ less events were generated, since due to the smaller cross sections the corresponding effective MC luminosity (cf. Equation (5.1)) is much larger. In addition, the signal selection is more effective at large values of $m_{\tilde{t}_1}$, since the kinematic features of the final-state particles are more pronounced.

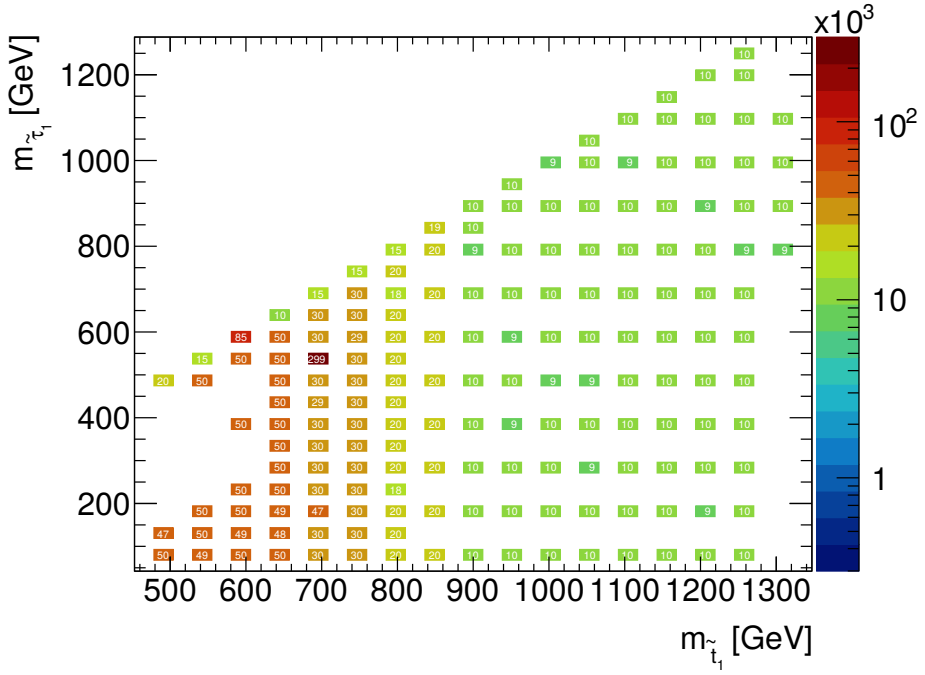

Figure 5.1.: Number of events generated for each sample of the signal process in the $m_{\tilde{\tau}_1}$-$m_{\tilde{t}_1}$ plane. For higher values of $m_{\tilde{t}_1}$ less events were generated. The remaining differences are dedicated points with extra statistics for legacy studies and small fluctuations in the production efficiency. The fluctuations are taken into account by considering the actual number of produced events when calculating the normalisation (cf. Equation (5.2)).

For the signal process, the cross-section calculations from [26] for the direct production of a $\tilde{t}_1$ pair are used and applied in dependence of $m_{\tilde{t}_1}$. They include next-to-leading-order supersymmetric QCD corrections with resummation at next-to-leading-logarithmic accuracy. The uncertainty of the cross-section calculation is derived from variations of the PDF set and the renormalisation and factorisation scale used in the calculation.

Table 5.1.: Versions of the programs used for the generation of the matrix elements and parton showers with the corresponding PDF sets and generator tunes for the simulated samples. SHERPA employs an internal parton shower and tune, therefore its version is only listed once. Table adapted from [3].

Process	Matrix element	PDF set	Parton shower	PDF set	Tune
$t\bar{t}$	POWHEG-BOX v2	CT10	PYTHIA 6.428	CTEQ6L1	Perugia 2012
single top	POWHEG-BOX v1	CT10	PYTHIA 6.428	CTEQ6L1	Perugia 2012
$t\bar{t}H$	MG5aMC 2.2.2	CT10	Herwig++ 2.7.1	CTEQ6L1	UE-EE-5
$t\bar{t}V$	MG5aMC 2.3.3	NNPDF3.0 NLO	PYTHIA 8.210	NNPDF2.3 LO	A14
tWZ	MG5aMC 2.3.2	NNPDF3.0 NLO	PYTHIA 8.210	NNPDF2.3 LO	A14
tZ	MG5aMC 2.2.1	CTEQ6L1	PYTHIA 6.428	CTEQ6L1	Perugia 2012
multi-top	MG5aMC 2.2.2	NNPDF2.3 LO	PYTHIA 8.186	NNPDF2.3 LO	A14
V+jets	SHERPA 2.2.1	NNPDF3.0 NNLO			
VV (1)	SHERPA 2.2.1	NNPDF3.0 NNLO			
VV (2)	SHERPA 2.1.1	CT10			
VVV	SHERPA 2.2.2	NNPDF3.0 NNLO			
SUSY	MG5aMC 2.2.3 and 2.3.3	NNPDF2.3 LO	PYTHIA 8.186, 8.205 or 8.210	NNPDF2.3 LO	A14

5.2.2. Background Samples

The samples for the SM background processes are produced centrally for all ATLAS analyses. An overview over the versions of the packages used for the individual processes is given in Table 5.1. The cross sections are applied in accordance to the recommendations of ATLAS listed in the respective references.

For the $t\bar{t}$ (single-top) process, POWHEG-BOX v2 (POWHEG-BOX v1) [83] is used for the matrix-element generation employing the PDF set CT10 [47, 84]. It is interfaced with PYTHIA 6.428 [85] using the PDF set CTEQ6L1 [86] and the Perugia 2012 tune [87]. The samples are filtered in order to increase the statistics at high $E_{\mathrm{T}}^{\mathrm{miss}}$ and H_{T}.

The associated production of $t\bar{t} + H$ is simulated with MADGRAPH5_aMC@NLO and the CT10 PDF set, interfaced with Herwig 2.7.1 [88, 89] using the CTEQ6L1 PDF set and the UE-EE-5 tune [90]. For the $t\bar{t} + V$ and $t + WZ$ processes MADGRAPH5_aMC@NLO with the NNPDF3.0 PDF set [91] is used and interfaced with PYTHIA 8.210 using the NNPDF2.3 LO PDF set and the A14 tune [92]. The t+Z (multi-top) processes are generated with MADGRAPH5_aMC@NLO as well, use the CTEQ6L1 (NNPDF2.3 LO) PDF set and are interfaced with PYTHIA 6.428 (PYTHIA 8.186) using the CTEQ6L1 (NNPDF2.3 LO) PDF set with the Perugia 2012 (A14) tune. All samples mentioned above contain bottom quarks — their decays are simulated with the EvtGen program [93].

Finally, the samples containing massive vector bosons are all simulated using SHERPA [94] as matrix-element generator which employs its own showering algorithms [95]. Z+jets and W+jets are simulated with SHERPA 2.2.1 and the NNPDF3.0 NNLO PDF set [96], as well as the tree-induced VV processes (VV(1) in Table 5.1). The loop-induced and vector-boson scattering VV processes (VV(2) in Table 5.1) are simulated with SHERPA 2.1.1 and the CT10 PDF set. Finally, the VVV processes use SHERPA 2.2.2

and the NNPDF3.0 NNLO PDF set [97].

5.3. Object Definitions

After the reconstruction procedure (as described in Section 4.6), additional identification criteria are applied for the final selection of the physics objects. These criteria are designed to result in a high identification rate while maintaining a low rate of false positives. Additional requirements ensure the selection of only well-measured objects and the removal of potential doubly reconstructed objects. The object definitions are summarised in Table 5.2 and detailed descriptions for each of them given in the following sections.

Table 5.2.: Summary of the object definitions used in the analysis presented. For τ_{had} the baseline and signal definition coincides.

Electrons	Baseline	Signal
p_{T} threshold	$p_{\text{T}} > 10$ GeV	$p_{\text{T}} > 25$ GeV
geometrical acceptance	$\lvert\eta_{\text{cluster}}\rvert < 2.47$	$\lvert\eta_{\text{cluster}}\rvert < 2.47$
quality	Loose (+b-layer hit)	Tight
isolation	—	`GradientLoose`
tracking cuts		$\lvert d_0/\sigma(d_0)\rvert < 5$
		$\lvert z_0 \sin(\theta)\rvert < 0.5$ mm
Muons	Baseline	Signal
p_{T} threshold	$p_{\text{T}} > 10$ GeV	$p_{\text{T}} > 25$ GeV
geometrical acceptance	$\lvert\eta\rvert < 2.7$	$\lvert\eta\rvert < 2.7$
quality	Medium	Medium
isolation	—	`GradientLoose`
tracking cuts		$\lvert d_0/\sigma(d_0)\rvert < 3$
		$\lvert z_0 \sin(\theta)\rvert < 0.5$ mm
Taus	Baseline/Signal	
p_{T} threshold	$p_{\text{T}} > 20$ GeV	
geometrical acceptance	$\lvert\eta\rvert < 2.5$, crack veto	
prongness	1 or 3	
quality/jet BDT WP	medium	
Jets	Baseline	b-jets
p_{T} threshold	$p_{\text{T}} > 20$ GeV	$p_{\text{T}} > 20$ GeV
geometrical acceptance	$\lvert\eta\rvert < 2.8$	$\lvert\eta\rvert < 2.5$
JVT cut	JVT > 0.59 (unless $p_{\text{T}} > 60$ GeV or $\lvert\eta\rvert > 2.4$)	
b-tag	–	MV2c10 @ 77 % WP

Electrons

The electron candidates from reconstruction are subjected to a likelihood-based multivariate analysis (MVA) [98]. Two working points are used in this analysis to identify electrons: a baseline selection using the "loose" WP and a signal selection using the "tight" WP, both as described in [98] but for the loose WP in addition also requiring a precision hit in the IBL.

Both selections require the electron candidates to be located in the central part of the detector covered by the ID ($|\eta_{\text{cluster}}| < 2.47$). Baseline (signal) electrons are required to have a p_{T} of at least 10 (25) GeV. Figure 5.2 shows the reconstruction and identifications efficiencies for electrons.

Signal electrons additionally have to fulfil the `GradientLoose` isolation requirements (cf. Table 2 in [98]). This isolation WP targets real electrons from hadronic decays as well as hadrons mis-identified as electrons. In both cases, additional tracks and ECal deposits are expected to be found close-by to the electron candidate in contrast to isolated leptons from e.g. a W- or Z-boson decay. There are two types of isolation requirements: the calorimeter-based isolation $E_{\text{T}}^{\text{cone, 0.2}}$ collects the sum of energies of clusters in a cone of $\Delta\text{R} < 0.2$, excluding the barycentre belonging to the electron identified. Track-based isolation $p_{\text{T}}^{\text{varcone, 0.2}}$ on the other hand uses the tracks (satisfying basic quality requirements) in a variable cone of size $\Delta\text{R} = \min(0.2, 10\text{ GeV}/E_{\text{T}})$, excluding the track of the identified electron. In the definition of the `GradientLoose` WP, both isolation requirements are used. The requirements are gradually tightened with E_{T} and p_{T} respectively and have both to fulfil the following isolation efficiencies, ϵ_{iso}, simultaneously:

$$\epsilon_{\text{iso}} \geq 0.057\% \times \frac{E_{\text{T}}(p_{\text{T}})}{\text{GeV}} + 95.57\%.$$

The cut values on $E_{\text{T}}^{\text{cone, 0.2}}$ and $p_{\text{T}}^{\text{varcone, 0.2}}$ are determined independently in bins of E_{T} (p_{T}) and η to meet the required isolation efficiencies up to an efficiency of 99 % while employing the tightest cut possible. Typical values of the electron isolation efficiency are 90 % at $E_{\text{T}} = 25$ GeV and 99 % at $E_{\text{T}} = 60$ GeV [98].

In addition to the isolation, signal electrons also have to fulfil track-to-vertex association (TTVA) cuts: the requirement on the significance of the transverse impact parameter ($d_0/\sigma(d_0)$) is $|d_0/\sigma(d_0)| < 5$, while the longitudinal impact parameter (z_0) has to fulfil $|z_0 \sin(\theta)| < 0.5$ mm.

The calibration procedure for electrons is described in detail in [99, 100] and follows, among others, these steps: In simulated samples an MVA-based training is performed to match the simulated cluster energy to the true electron energy. The longitudinal layers of the ECal (as described in Section 4.3) are inter-calibrated using data to equalise the energy scales of the individual layers. After these steps, the calibration derived on simulation is applied to data as well as to the simulated samples. Scale factors are determined on a large sample of $Z \to e^+e^-$ events to match the observation to the expectation from simulation.

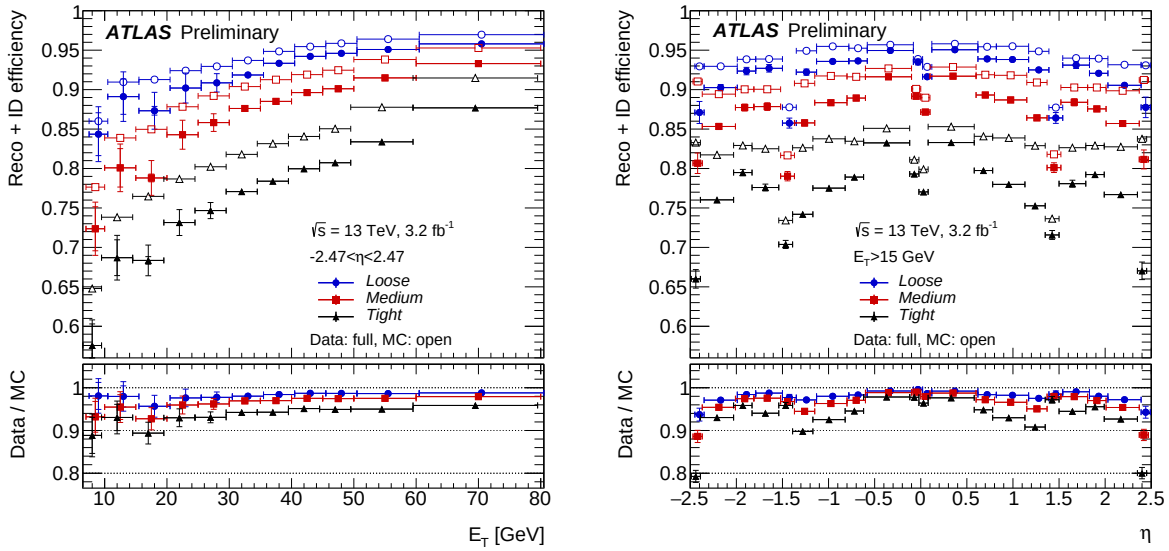

(a) Reconstruction and identification efficiency as a function of E_{T}

(b) Reconstruction and identification efficiency as a function of η

Figure 5.2.: Reconstruction and identification efficiencies of electrons measured in $Z \to e^+e^-$ events on the data collected in 2015 at 13 TeV centre-of-mass energy [98]. The open symbols show the values extracted from MC, while the filled symbols are determined from data. In this analysis the "Loose" (blue) and "Tight" (black) WPs are used. The ratio pad contains the scale factors applied in the analysis.

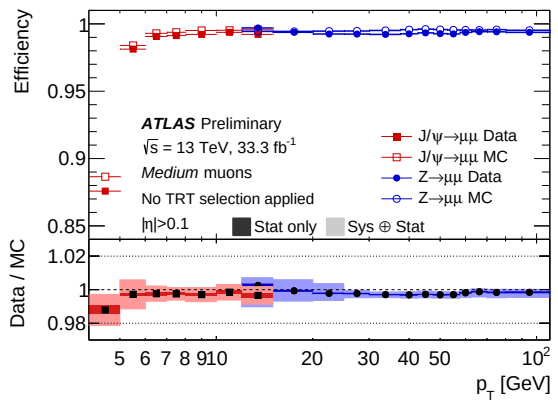

(a) Reconstruction and identification efficiency as a function of p_{T}. The medium identification WP is shown and the central region of $|\eta| < 0.1$ is excluded.

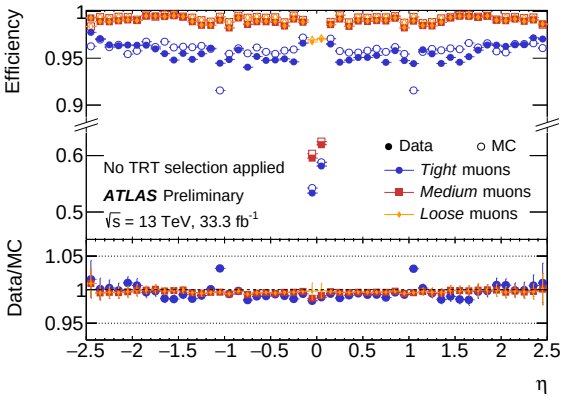

(b) Reconstruction and identification efficiency as a function of η. In this analysis the medium identification WP is used (red). At $\eta \approx 0$ the efficiency is reduced due to service gaps in the MS coverage.

Figure 5.3.: Reconstruction and identification efficiencies of muons measured in $Z \to \mu^+\mu^-$ and $J/\Psi \to \mu^+\mu^-$ events in the data collected in 2016 at a centre-of-mass energy of 13 TeV [102]. The open symbols show the values extracted from simulation, while the filled symbols are determined from data.

Muons

All muons considered in this analysis fulfil the "medium" identification criteria described in [101]. They comprise requirements on the number of tracks in the sub-systems and the quality of the track fits to provide a suppression of mis-identified hadrons. Muons of baseline (signal) quality have to be in the central part of the detector covered by the MS ($|\eta| < 2.7$, cf. Section 4.4) and their p_{T} needs to be at least 10 (25) GeV.

For muons of signal quality, the `GradientLoose` isolation requirement, as described above for the electrons, as well as TTVA cuts are applied: the TTVA cut for the significance of the transverse impact parameter is $|d_0/\sigma(d_0)| < 3$, while a requirement on the longitudinal impact parameter z_0 of $|z_0 \sin(\theta)| < 0.5$ mm is applied. The reconstruction efficiency of muons in MC simulation in the p_{T}-window of 20–100 GeV and $|\eta| < 2.5$ is 96.1 %, whereas the misidentification probability is 0.17 %. Figure 5.3 shows the reconstruction and identification efficiencies as a function of p_{T} and η.

Hadronically Decaying Taus

As mentioned in Section 4.6, the visible part of hadronically decaying tau leptons ($\tau_{\text{had-vis}}$) has a detector signature of jets, demanding a sophisticated identification strategy, making use of kinematics and the substructure of the jets. The associated combined performance group in ATLAS decided to train a boosted decision tree (BDT) for 1- and 3-prong τ_{had} separately using a $Z/\gamma^* \to \tau\tau$ sample as signal and a di-jet sample as background [68].

A total of twelve variables are used as input for the BDT. These variables are con-

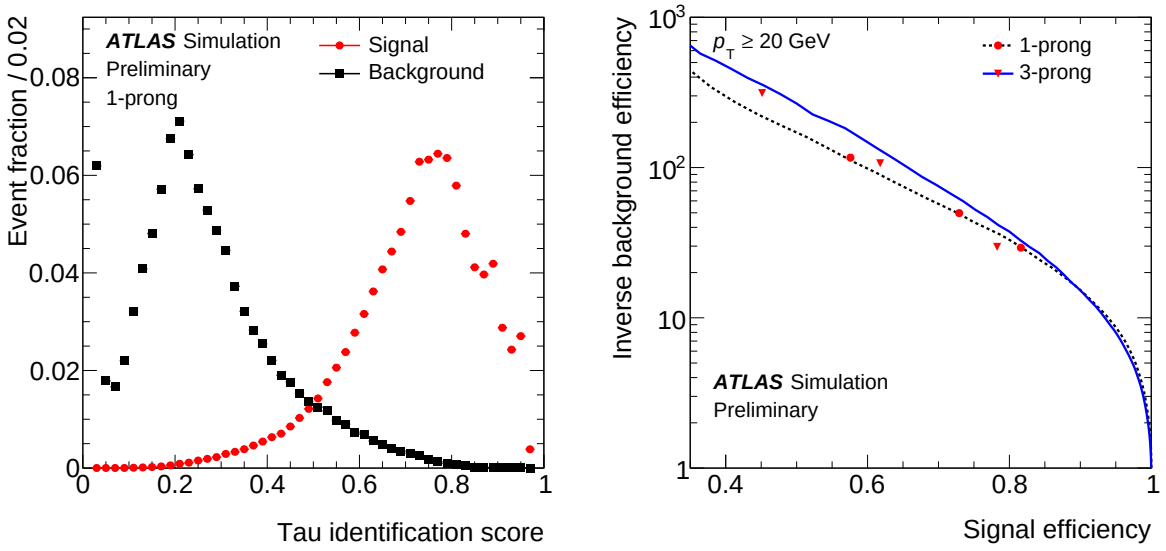

(a) Output of the BDT training for 1-prong τ_{had}. The separation of the signal (red) and background (black) sample is shown.

(b) Background rejection as a function of signal efficiency for 1- and 3-prong taus. The red markers indicate the WPs tight, medium and loose. The curve is derived for a constant BDT cut, but since the WPs employ a p_{T}-flattening the markers do not match the lines exactly.

Figure 5.4.: BDT performance in the identification of $\tau_{\text{had-vis}}$ as determined on simulated samples [68].

structed from information of tracks and calorimeter deposits associated to the $\tau_{\text{had-vis}}$ candidate. Also, higher-level combinations of the variables in the form of ratios and invariant masses are used. The features of tracks and calorimeter depositions are assessed by variables comparing the depositions in a central ($\Delta\text{R} < 0.2$) and an isolation ($0.2 < \Delta\text{R} < 0.4$) cone as well as variables evaluating the distribution of tracks with respect to the reconstructed $\tau_{\text{had-vis}}$ axis. Finally, there are variables sensitive to the track displacement with respect to the determined tau vertex. The details of the definitions of the variables can be found in [68] and the output of the training is shown in Figure 5.4 (a).

The efficiency of the $\tau_{\text{had-vis}}$ reconstruction and identification is summarised in Figures 5.4 and 5.5. The medium WP is a good compromise between high signal efficiency and reasonable background rejection. A second BDT is trained to explicitly reject electrons passing the tau identification criteria.

All $\tau_{\text{had-vis}}$ candidates considered in the analysis have to have at least 20 GeV in p_{T} and be located in the central region ($|\eta| < 2.5$), excluding the crack region ($1.37 < |\eta| < 1.52$). The reconstructed charge has to be $\pm e$, the number of reconstructed charged tracks one or three, and the BDT score of the medium WP fulfilled. Jets of other origin, as e.g. quarks and gluons accidentally passing the identification criteria of $\tau_{\text{had-vis}}$ are called “fake taus” in the following.

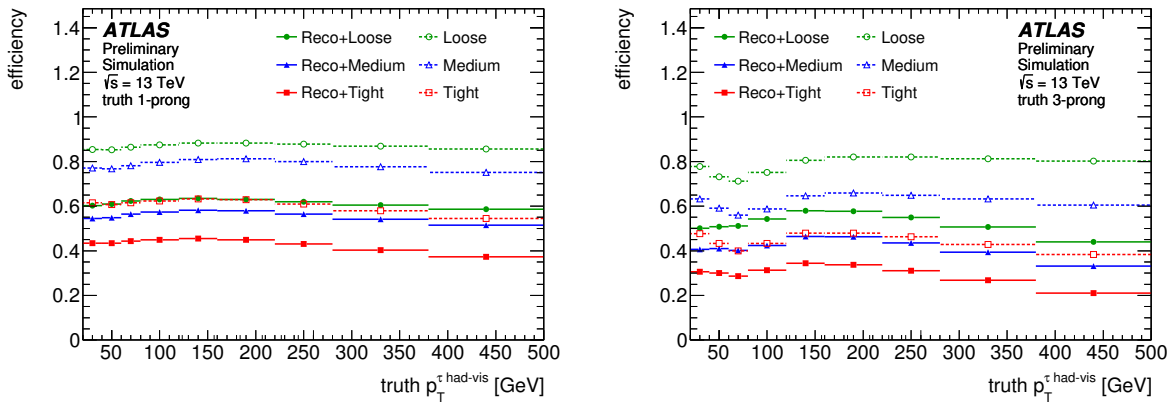

(a) Reconstruction and identification efficiencies for 1-prong taus.

(b) Reconstruction and identification efficiencies for 3-prong taus.

Figure 5.5.: Reconstruction and identification efficiencies for $\tau_{\text{had-vis}}$ as a function of the true $\tau_{\text{had-vis}}$ p_{T} [68]. Both plots show the medium WP in blue. The efficiencies are given as combined efficiencies for reconstruction and identification (e.g. "Reco+Medium") and as single identification efficiency (e.g. "Medium")

Jets

Jets used in this analysis are reconstructed as described in Section 4.6 and further required to be located in the barrel part of the detector ($|\eta| < 2.8$) and to have a calibrated p_{T} of at least 20 GeV.

In order to reject jets from pile-up, i.e. jets not originating from the leading PV, the multivariate jet-vertex-tagger (JVT) variable is constructed [103]. It is a combination of two variables: The first one is the corrected jet vertex fraction (corrJVF). It is the fraction of the scalar sum of the p_{T} of tracks originating from the leading PV (p_{T}^{HS}) with respect to the corrected total p_{T} of the jet considered. The corrected total p_{T} is given by the scalar sum of the p_{T} of tracks originating from other primary vertices (p_{T}^{PU}) corrected for the total number of tracks from these vertices ($N_{\text{track}}^{\text{PU}}$) and added to p_{T}^{HS}. The corrected jet vertex fraction is then given by

$$\text{corrJVF} = \frac{p_{\text{T}}^{\text{HS}}}{p_{\text{T}}^{\text{HS}} + \frac{p_{\text{T}}^{\text{PU}}}{kN_{\text{track}}^{\text{PU}}}}$$

where the discrimination power is independent of the scaling k (set to 0.01).

The second variable is the fraction of p_{T}^{HS} with respect to the fully calibrated jet p_{T}:

$$R_{p_{\text{T}}} = \frac{p_{\text{T}}^{\text{HS}}}{p_{\text{T}}^{\text{jet}}}$$

Both variables are combined into a 2-dimensional likelihood called JVT, and for central ($|\eta| < 2.4$) low-p_{T} (< 60 GeV) jets JVT needs to exceed 0.59.

B-Jets

The identification of jets originating from b-quarks (b-jets) is another important ingredient for the analysis presented here. Additional requirements are applied to the reconstructed jets in order to discriminate them from jets arising from lighter quarks.

The decay lengths of b-hadrons ($c\tau(B^{\pm}) = 491.5$ μm, $c\tau(B^0) = 455.7$ μm [8]) are of a length-scale which can be resolved by the silicon tracking detectors. The identification of b-jets relies on variables sensitive to the displacement of tracks due to the non-negligible lifetime and is implemented in three different complementary algorithms combined in a MVA [104]: impact-parameter based algorithms, secondary-vertex reconstruction and the kinematic fitting of the tracks.

IP2D and IP3D are the impact-parameter-based algorithms [105, 106]. Likelihoods for a track being a b-jet (p^b), c-jet (p^c) or light-jet[3] (p^l) are derived on simulated samples for in total 13 categories depending on the track topology (cf. Table 1 in [107]). The IP2D (IP3D) discriminant is then defined as the sum of the log-likelihood ratios for all N tracks belonging to the jet

$$\mathrm{LLR}(b, l) = \sum_{i=1}^{N} \log \frac{p_i^b}{p_i^l},$$

where transverse (and longitudinal) impact-parameter significances are used. The advantage of this approach is that it is straight-forward to do a discrimination of b-jets and c-jets ($\mathrm{LLR}(b, c)$).

The SV1 algorithm [105] uses an iterative approach to fit a secondary vertex (SV) from the tracks of the jet considered. Vertices from long-lived particles such as Λ or kaons are rejected as well as vertices likely originating from material interactions or photon conversions. If a vertex fulfils certain quality criteria such as e.g. a low χ^2, it is considered as the SV and several variables such as e.g. the signed decay length significance or invariant mass of tracks belonging to the SV are used in the later steps for discrimination.

JetFitter [108] is used as the third algorithm. It explicitly targets the decay cascade of the (displaced) b-hadron decay and the subsequent c-hadron decays, assuming them to be in the flight direction of the b-hadron. Typical outputs of this algorithm are e.g. the number of displaced vertices (in different categories based on the number of tracks), the invariant mass of the displaced vertices, the energy fraction in the individual displaced vertices, or the significance of the average distance of the displaced vertices.

The final discriminating variable is the output of MV2c10 — a BDT trained on the outputs of the basic tagging algorithms mentioned above (listed in detail in Table 2 of [107]). The training is performed on a simulated sample of the $t\bar{t}$ process with b-jets considered as signal and c-jets and light-jets considered as background, where the c-jets make up 7 % of the background sample. The performance of MV2c10 is shown in Figure 5.6.

[3] In the context of flavour tagging the term light-jet refers collectively to jets originating from u, d, s quarks, or gluons.

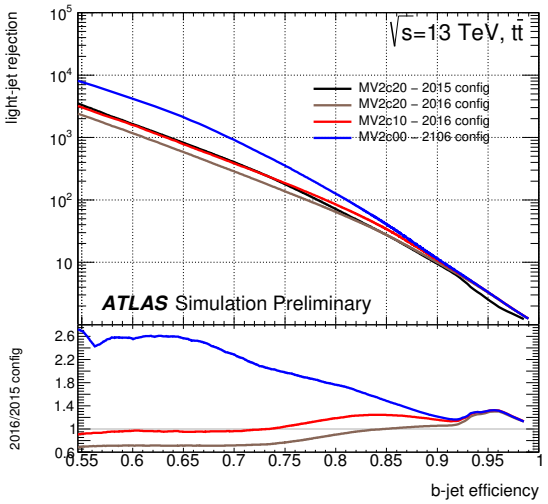

(a) Light-jet rejection as a function of b-jet efficiency.

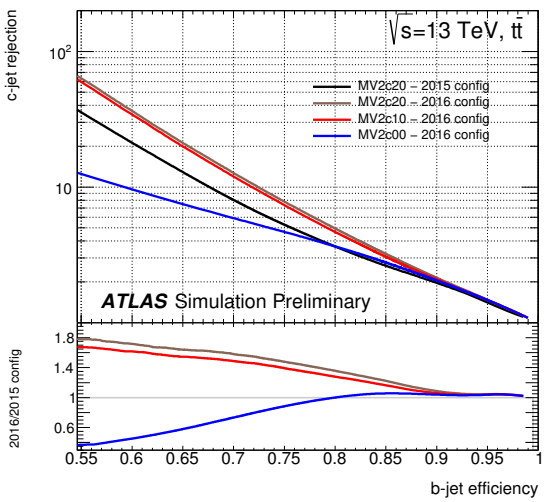

(b) C-jet rejection as a function of b-jet efficiency.

Figure 5.6.: Performance of the different trainings setups of MV2 in the configuration used in 2016 [104]. The red line shows MV2c10, the training configuration used in the analysis.

Photons

Photons (only used for the $E_{\mathrm{T}}^{\mathrm{miss}}$ calculation) are calibrated and identified with the *tight* WP as described in [70]. Photons have to be located in the central part of the detector ($|\eta| < 2.37$) with a p_{T} of at least 25 GeV.

Overlap Removal

The reconstruction of the different physics objects described in Section 4.6 is performed independently in the common ATLAS reconstruction software. In order to avoid using a physical object more than once, an overlap removal (OR) procedure is performed, resulting in the final object selection. The second issue addressed in this step are isolation requirements e.g. rejecting leptons from heavy-flavour decays.

The OR is performed sequentially such that objects which are removed in one step will not show up in the next. All objects of baseline quality are considered in this algorithm. It has to be noted that for jets for the calculation of ΔR the rapidity (cf. Equation (4.1)) of the involved physics objects is used instead of pseudorapidity. Table 5.3 summarises the sequence of steps performed.

In order to resolve the ambiguity of light leptons and $\tau_{\text{had-vis}}$ close to each other ($\Delta\mathrm{R} < 0.2$), the $\tau_{\text{had-vis}}$ are discarded, since light leptons have a lower fake rate. Electrons are removed if they share an ID track with muons, since the physical object most likely is a muon with significant energy loss in the ECal. Jets close ($\Delta\mathrm{R} < 0.2$) to light leptons are removed, since the muons can and the electrons have to also be reconstructed as jets. In the following step, an isolation requirement with respect to the jets is enforced by removing light leptons in a broader cone of $\Delta\mathrm{R} < 0.4$. Since the seeds for the $\tau_{\text{had-vis}}$

Table 5.3.: Sequence of OR steps.
†: Combined muons are only considered if $p_{\mathrm{T}}(\mu) > 50$ GeV.
‡: To be considered here, the jet has to have less than 3 tracks associated with the leading PV.

Object for comparison	Object removed	condition
e	$\tau_{\text{had-vis}}$	$\Delta\mathrm{R} < 0.2$
$\mu^{\dagger}$	$\tau_{\text{had-vis}}$	$\Delta\mathrm{R} < 0.2$
μ	e	shared ID track
e	jet	$\Delta\mathrm{R} < 0.2$
jet	e	$\Delta\mathrm{R} < 0.4$
μ	jet‡	$\Delta\mathrm{R} < 0.2$ or μ ghost matched to jet
jet	μ	$\Delta\mathrm{R} < 0.4$
$\tau_{\text{had-vis}}$	jet	$\Delta\mathrm{R} < 0.4$

are jets themselves, jets in the vicinity of $\tau_{\text{had-vis}}$ are removed.

Missing Transverse Energy

In the analysis presented here, a number of detector-invisible particles is expected from the signal process. SM neutrinos arise from its three-body decay as well as from the tau decays. The LSPs will also escape undetected. The only way to learn about the detector-invisible particles is to sum up the momenta of all visible particles and to deduce the sum of the momenta of all invisible particles from energy-momentum conservation. Since the boost in z-direction is not known (cf. Section 3.1) the momenta of visible and invisible particles will add up to zero only in the transverse plane.

To determine the sum of $\boldsymbol{p}_{\mathrm{T}}$ of the visible objects, the calibrated objects are used in order to achieve the best p_{T} determination possible. The remaining soft contributions which are not associated to any of the reconstructed objects are used as well. The soft contributions are collected by using the tracks from the leading PV not associated to any of the reconstructed hard objects (electrons, muons, τ_{had}, jets, and photons) surviving the OR [109]. In contrast to using calorimeter deposits, this method has the advantage of being more robust with respect to pile-up contributions, but is lacking the contributions of neutral particles. In this analysis mostly the magnitude $E_{\mathrm{T}}^{\text{miss}}$ of the missing transverse momentum ($\boldsymbol{p}_{\mathrm{T}}^{\text{miss}}$) is used.

5.4. Event Kinematics

In the following section an overview over variables sensitive to the event kinematics is given. These variables are used to discriminate the background processes described in Section 3.2 from the signal model (cf. Section 2.3), and between the background processes themselves.

Invariant Mass

The invariant mass m_{inv} is defined as the positive solution to the equation

$$m_{\text{inv}}^2(p_1, p_2) = (p_1 + p_2)^2 = (E_1 + E_2)^2 - (\boldsymbol{p}_1 + \boldsymbol{p}_2)^2, \tag{5.3}$$

with the 4-momenta of two particles (p_1 and p_2), which can be expressed in p_{T}, η, ϕ as described in Section 4.1. If the two particles considered are products of a two-body decay of a parent particle with mass m_p, m_{inv} will coincide with m_p. Since the Z boson decays to a pair of very well measurable particles of same flavour, but opposite sign, m_{inv} is mainly used to target and to reject the Z+jets process.

Transverse Mass

In case of the decay of a parent particle into two child particles, where one of the particles is only weakly interacting and therefore invisible to the detector, as e.g. for a W boson, a variant of m_{inv}, the transverse mass m_{T}, can be calculated. It was first used by the UA1 collaboration [110] and is defined as

$${m_{\text{T}}}^2 = (E_{\text{T},1} + E_{\text{T},2})^2 - \left(\boldsymbol{p}_{\text{T},1} + \boldsymbol{p}_{\text{T},2}\right)^2, \tag{5.4}$$

where only the transverse components of both child particles (1 and 2) enter. In the limit of massless child particles this formula can be simplified to

$${m_{\text{T}}}^2 = 2\, p_{\text{T},1}\, p_{\text{T},2}\, \left(1 - \cos(\Delta\phi)\right), \tag{5.5}$$

where $p_{\text{T},1}$ and $p_{\text{T},2}$ are the magnitudes of the transverse momenta of the child particles and $\Delta\phi$ is their angular separation in the transverse plane.

Due to the missing longitudinal component (which is not measurable for the invisible particle, cf. Section 4.1), m_{T} does only coincide with the mass of the parent particle if the decay products are fully contained in the transverse plane. In the case that the plane of the decay products is inclined or rotated with respect to the transverse plane, m_{T} is smaller than the mass of the parent particle. In any case m_{T} is bounded from above by the mass of the parent particle.

Stransverse Mass

The transverse mass has limited discrimination power if two or more invisible particles are involved, since the invisible particles will appear as a vectorial sum in $\boldsymbol{p}_{\text{T}}^{\text{miss}}$. The individual momenta of the undetected particles are therefore not accessible. Therefore, the calculation of m_{T} will not yield the clear cut-off behaviour any more. The stransverse mass (m_{T2}) provides an alternative to m_{T} in the case that two particles decay into one visible and one invisible particle each. The idea of m_{T2} [111] is to calculate m_{T} for both branches simultaneously by splitting up the available $\boldsymbol{p}_{\text{T}}^{\text{miss}}$ to the two branches corresponding to the two parent particles. The implementation by Lester and Nachmann [112] used in this analysis allows for the calculation of asymmetric branches, but since only the symmetric case is considered here, the discussion is restricted to the symmetric definition.

Two branches are defined by the corresponding visible particles with momenta p_a and p_b. The total missing transverse energy $\boldsymbol{p}_{\mathrm{T}}^{\mathrm{miss}}$ is split into two parts $\boldsymbol{q}_a^{\mathrm{miss}}$ and $\boldsymbol{q}_b^{\mathrm{miss}}$ with the constraint

$$\boldsymbol{p}_{\mathrm{T}}^{\mathrm{miss}} = \boldsymbol{q}_a^{\mathrm{miss}} + \boldsymbol{q}_b^{\mathrm{miss}}$$

and the transverse masses for every splitting of $\boldsymbol{p}_{\mathrm{T}}^{\mathrm{miss}}$ are taken into consideration:

$$m_{\mathrm{T}a} = m_{\mathrm{T}}(\boldsymbol{p}_{\mathrm{T}a}, \boldsymbol{q}_a^{\mathrm{miss}}), \quad m_{\mathrm{T}b} = m_{\mathrm{T}}(\boldsymbol{p}_{\mathrm{T}b}, \boldsymbol{q}_b^{\mathrm{miss}})$$

If the hypothesis of two parent particles with the same mass m_p decaying to one visible and one invisible particle each holds, there will be at least one configuration of $\boldsymbol{q}_a^{\mathrm{miss}}$ and $\boldsymbol{q}_b^{\mathrm{miss}}$ where both $m_{\mathrm{T}a}$ and $m_{\mathrm{T}b}$ are smaller than m_p. One trivial configuration is obtained by setting $\boldsymbol{q}_a^{\mathrm{miss}}$ and $\boldsymbol{q}_b^{\mathrm{miss}}$ to the transverse momenta of the two invisible particles.

The definition of m_{T2} is such that by means of minimisation the configuration where the maximum of $m_{\mathrm{T}a}$ and $m_{\mathrm{T}b}$ is smallest is searched:

$$m_{\mathrm{T2}}(p_a, p_b)^2 = \min_{\boldsymbol{q}_a^{\mathrm{miss}} + \boldsymbol{q}_b^{\mathrm{miss}} = \boldsymbol{p}_{\mathrm{T}}^{\mathrm{miss}}} \left(\max \left[{m_{\mathrm{T}}}^2(\boldsymbol{p}_{\mathrm{T}a}, \boldsymbol{q}_a^{\mathrm{miss}}), {m_{\mathrm{T}}}^2(\boldsymbol{p}_{\mathrm{T}b}, \boldsymbol{q}_b^{\mathrm{miss}}) \right] \right) \tag{5.6}$$

In case the assumptions made above hold, m_{T2} is bounded from above by m_p.

The potential caveat of the concept of m_{T2} is shown in Figure 5.7. The sketches show the distribution of momenta in the transverse plane and illustrate two fundamentally different cases. The sketch on the left (Figure 5.7 (a)) shows a case of the desired behaviour of m_{T2}. The recoil and the $\boldsymbol{p}_{\mathrm{T}}^{\mathrm{miss}}$ are in the opposite direction of the two visible particles. $\boldsymbol{p}_{\mathrm{T}}^{\mathrm{miss}}$ is distributed to both branches and the corresponding values of m_{T} are close to each other with a non-zero value of about 30 % of $p_{\mathrm{T},a} + p_{\mathrm{T},b} + |\boldsymbol{p}_{\mathrm{T}}^{\mathrm{miss}}|$ (cf. Appendix A.2 for the calculation). In the sketch on the right (Figure 5.7 (b)), $\boldsymbol{p}_{\mathrm{T}}^{\mathrm{miss}}$ is located in the same hemisphere and in between the two visible momenta. In this configuration, the $\boldsymbol{p}_{\mathrm{T}}^{\mathrm{miss}}$ can be trivially split up collinearly to the momenta, such that the values of both $m_{\mathrm{T}a}$ and $m_{\mathrm{T}b}$ can be zero and therefore yield a valid (trivial) minimum of $m_{\mathrm{T2}} = 0$. These corner cases have to be considered when using m_{T2} in analyses. It will be shown that, even with this caveat, m_{T2} has a very good performance with respect to the signal-to-background separation.

HT and MET Significance

In the context of the analysis presented, the hadronic activity of an event (H_{T}) is defined as the scalar sum of the transverse momenta of the two jets with largest transverse momentum. $E_{\mathrm{T}}^{\mathrm{miss}}$ is susceptible to mismeasurements of the objects reconstructed. In particular, large hadronic activity can deteriorate the $E_{\mathrm{T}}^{\mathrm{miss}}$ performance.

The stochastic component of the energy resolution of the calorimeters is proportional to $\sqrt{E_{\mathrm{T}}}$ [113]. To suppress the effects of mismeasurements due to high hadronic activity, the $E_{\mathrm{T}}^{\mathrm{miss}}$-significance ($E_{\mathrm{T}}^{\mathrm{miss,\,sig}}$) is defined:

$$E_{\mathrm{T}}^{\mathrm{miss,\,sig}} = \frac{E_{\mathrm{T}}^{\mathrm{miss}}}{\sqrt{H_{\mathrm{T}}}} \tag{5.7}$$

This definition is especially useful for the rejection of background processes without real sources of $E_{\mathrm{T}}^{\mathrm{miss}}$, where high values of $E_{\mathrm{T}}^{\mathrm{miss}}$ mostly arise from large mismeasurements of the hadronic recoil.

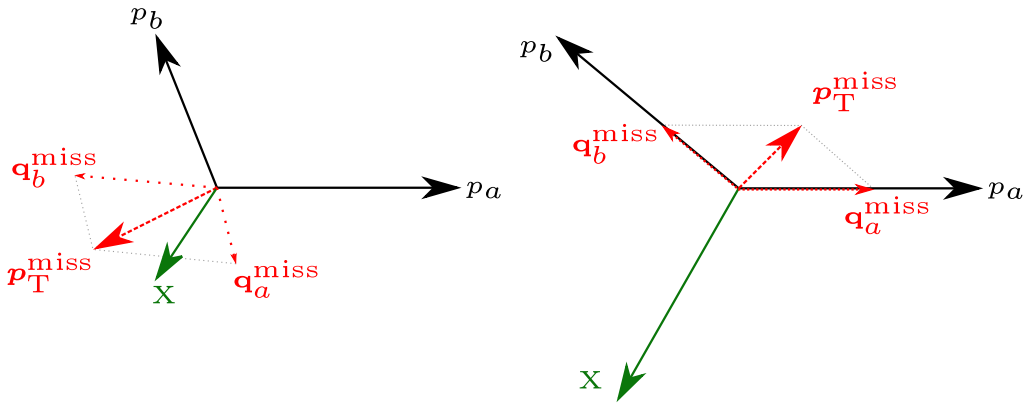

(a) Target case of the m_{T2} variable. The corresponding values of $m_{\text{T}a}$ and $m_{\text{T}b}$ are of similar magnitude.

(b) Trivial minimisation of both branches. This splitting of $\boldsymbol{p}_{\text{T}}^{\text{miss}}$ corresponds to $m_{\text{T}a} = m_{\text{T}b} = 0$.

Figure 5.7.: Two possible results of the m_{T2} calculation. Shown are the momenta in the transverse plane. The momenta of the two visible particles p_a, p_b are shown in black. The big red dashed line shows the total $\boldsymbol{p}_{\text{T}}^{\text{miss}}$ in the event, while the smaller dotted lines show the two components as determined by the m_{T2} algorithm ($\boldsymbol{q}_a^{\text{miss}}$, $\boldsymbol{q}_b^{\text{miss}}$). The green arrow ($X$) shows the remaining momentum, which can be interpreted as the sum of the p_{T} of the visible particles recoiling against the system defined by $\boldsymbol{p}_{\text{T}}^{\text{miss}}$ and the momenta p_a and p_b.

Invariant Mass Compatible with the Mass of the Z Boson

Backgrounds containing Z bosons (most notably $t\bar{t} + Z$ and VV), are contributing significantly to the part of the phase space used in this analysis. In order to efficiently select these backgrounds, a variable called m_Z^{closest} is used.

m_Z^{closest} is an event-level variable, constructed by calculating the invariant masses of all same-flavour, opposite-sign lepton pairs in the event (m_{inv}^i). The invariant mass of the lepton pair which minimises $|m_{\text{inv}}^i - m_Z|$ is defined as m_Z^{closest}. For m_Z the PDG-value of the mass of the Z boson is used.

In this analysis only positive selections on m_Z^{closest} are done, i.e. only events fulfilling the Z boson requirement are selected. The rejection of these events is not considered. Therefore, in case that no candidate lepton pair is found a default value is used, such that these events will not be considered when applying a selection on m_Z^{closest}.

5.5. Event Selection

In this analysis, three different selections are used to define regions of interest in the phase space. The selections include the two search channels (lep-had and had-had channel) and an additional selection in order to constrain the normalisation of two more complicated backgrounds. The lep-had and had-had selections provide the phase space for the definition of control and validation regions for the $t\bar{t}$ process and the corresponding signal regions. The third selection is used for the two shared control regions (CRs) of the $t\bar{t} + Z$ and VV processes.

5.5.1. Trigger Setup

Two different trigger setups are used in this analysis, one to trigger the light-leptonic signatures in the lep-had selection and the two common CRs, the other to target the final state with two τ_{had}. Early studies showed that both signal region (SR) selections will have, besides the isolated leptons, a high $E_{\text{T}}^{\text{miss}}$ requirement, such that triggers for both signatures can be considered.

The two setups have in common that the triggers are required to be fully efficient in the selected phase-space. Since triggers need to make a fast decision, they cannot use the full detector information. On the trigger level some of the identification algorithms for the physics objects are run in a simplified version.

The thresholds for a certain variable at trigger level do not exactly match the calibrated values used in the analysis. This mismatch gives rise to the turn-on region, the region where the trigger efficiency increases as a function of the calibrated value of the variable until reaching the plateau of constant efficiency with respect to the decision of the trigger. In the turn-on region, differences in modelling of data and simulation can lead to large uncertainties, therefore a conservative cut is placed on the variable considered.

To correct for remaining differences between data and simulation, scale factors are derived in tag-and-probe analyses, which are carried out by the respective combined-performance groups [114]. These scale factors require the reconstructed object to be matched to the object firing the trigger, such that the scale factors can be derived in dependence of properties of the object, e.g. p_{T} and η. Uncertainties arising from the measurement of the trigger scale factors are included as described in Section 5.7.1.

Single Light-Lepton Triggers

For the light-leptonic signatures, one of the lowest unprescaled single-lepton triggers is required to have fired. Due to the increase of instantaneous luminosity between the dataset collected in 2015 and 2016, different sets of triggers are used. For each object and year, a combination of several triggers is used. They have different p_{T}, isolation, and identification quality requirements, where with increasing p_{T} thresholds the isolation and identification requirements can be loosened to recover potential inefficiencies of the tighter selections with lower thresholds.

$E_{\text{T}}^{\text{miss}}$-based and combined light-lepton plus τ_{had} triggers were studied (cf. [115]), but showed similar or worse signal efficiency for the lep-had SR. Triggers targeting τ_{had} are prone to accidentally be fired by a jet due to the similarities in signature and the subset of variables available at trigger level, as e.g. the tracking information from the ID. To keep the trigger rates acceptable, the p_{T} thresholds of τ_{had} triggers usually have to be higher than for the light-lepton triggers.

The common CRs are τ_{had}-agnostic, therefore the single-lepton triggers can be used for both selections. Triggers based on $E_{\text{T}}^{\text{miss}}$ have a performance similar to the light-lepton triggers, but reduce the phase space available for background estimation in the lep-had selection as well as in the selection for the common CRs.

The combination of triggers only gives reason to expect minor increases of the signal efficiency for the SR, therefore the simplest trigger setup, the single light-lepton triggers,

was chosen for the analysis. The matched electron (muon) is required to exceed 27 (27.3) GeV in order to be fully efficient.

Two-Tau Triggers

For the final state with two hadronically decaying tau leptons, a combination of triggers is used to maximise the available dataset for the had-had selection. Also here, several options were studied (cf. [116]). Two different triggers with a two-tau signature were available, one with an additional jet required at the hardware level and the other one with an additional $E_{\mathrm{T}}^{\mathrm{miss}}$ requirement [57]. On top of that, also the trigger just requiring $E_{\mathrm{T}}^{\mathrm{miss}}$ was considered. Studies of the signal efficiencies of the different triggers showed that the combined trigger requiring two τ_{had} and $E_{\mathrm{T}}^{\mathrm{miss}}$ is outperformed by each of the other two triggers on their own. The $E_{\mathrm{T}}^{\mathrm{miss}}$-only trigger has high efficiency for large and small splittings between $m_{\tilde{t}_1}$ and $m_{\tilde{\tau}_1}$, while the trigger requiring two τ_{had} with an additional jet is strongest for intermediate mass splittings.

Due to the necessity of having CRs at lower $E_{\mathrm{T}}^{\mathrm{miss}}$, a logical "or" of the $E_{\mathrm{T}}^{\mathrm{miss}}$-only trigger with the combined trigger requiring two τ_{had} and an additional jet is used in the had-had selection. In addition to at least one of the triggers having fired, for the $E_{\mathrm{T}}^{\mathrm{miss}}$-only trigger the fully calibrated $E_{\mathrm{T}}^{\mathrm{miss}}$ has to exceed 180 GeV and for the trigger requiring two τ_{had} with an additional jet, the leading (sub-leading) τ_{had} needs to have at least $p_{\mathrm{T}} > 50$ (40) GeV and an additional jet with $p_{\mathrm{T}} > 80$ GeV has to be present.

5.5.2. Common Preselections

Three preselection requirements are defined for the different selections. They target different parts of the phase space. While the had-had selection is mutually disjoint to the two others, the lep-had selection has a small overlap with the common control-region selection. This overlap is removed with the respective CR definitions. The selection requirements are summarised in Table 5.4.

Table 5.4.: Requirements for the three preselections used in this analysis. If no requirement is applied, the field is marked with "—". $p_{\mathrm{T}}(\mathrm{jet}_2)$ is the p_{T} of the sub-leading jet and $p_{\mathrm{T}}(\tau_{\text{had-vis}})$ refers to the leading $\tau_{\text{had-vis}}$ candidate.

selection	lep-had	common CRs	had-had
Trigger set	light lepton	light lepton	$E_{\mathrm{T}}^{\mathrm{miss}}$ or two τ_{had} with add. jet
No. of light signal leptons	1	—	0
No. of signal leptons	—	≥ 2	—
No. of τ_{had}	1	—	2
Additional baseline leptons	veto	—	veto
No. of b-jets	≥ 1	—	≥ 1
$p_{\mathrm{T}}(\mathrm{jet}_2)$	≥ 26 GeV	≥ 26 GeV	≥ 20 GeV
$p_{\mathrm{T}}(\tau_{\text{had-vis}})$	≥ 70 GeV	—	≥ 70 GeV

Lep-Had Selection

The lep-had selection targets a SR where in the signal process one tau lepton decays hadronically and the other leptonically. The requirements for the single light-lepton triggers are used as discussed in Section 5.5.1. Exactly one light lepton of signal quality and exactly one τ_{had} is allowed, while rejecting events with additional leptons of baseline quality because they do not arise in the lep-had signature of the signal model.

Given the two b-quarks in the signal process, a requirement of at least one b-jet is introduced. The requirement is a compromise between the limited identification efficiency of b-jets (59 % for two b-jets, but 95 % for at least one b-jet) and the rejection of background processes lacking genuine b-quarks. At least two jets exceeding 26 GeV in p_{T} are required. This cut is necessary due to a skimming requirement introduced in the centrally produced data samples, but has negligible impact on the sensitivity of the SR. Finally, the selected $\tau_{\text{had-vis}}$ has to exceed 70 GeV in p_{T}. The $p_{\text{T}}(\tau_{\text{had-vis}})$ requirement is motivated by the good signal-to-background discrimination and will be discussed below.

Had-Had Selection

The SR where both of the taus decay hadronically is targeted by the had-had selection. The combined trigger requirement is used as discussed in Section 5.5.1. Events with exactly two τ_{had} but no additional baseline leptons are selected. At least two jets (with $p_{\text{T}} > 20$ GeV) are required. At least one jet should fulfil the b-jet-identification requirements. The leading $\tau_{\text{had-vis}}$ is required to have at least 70 GeV in p_{T}, as it does in the lep-had selection. The cut on $p_{\text{T}}(\tau_{\text{had-vis}})$ is the same for all regions in which the $t\bar{t}$ process is normalised or the normalisation used, in order to reduce the impact of potential p_{T}-dependent mismodelling in data.

Common Control-Region Selection

The common control regions are special in the sense that they do not target explicitly a τ_{had} signature but only require at least two leptons of signal quality and any number of additional leptons is allowed. They use the single light-lepton based triggers and also require at least two jets with $p_{\text{T}} > 26$ GeV. The trigger requirements imply that at least one of the leptons is a light lepton.

5.5.3. Signal Regions

SRs are regions in phase space that are enriched in events of the signal process, while maintaining a relatively small contribution of events from SM processes. These SRs are used to compare the observation with the theory predictions and data-driven estimates. The observation allows to either find evidence for the targeted signal model or to establish the absence of it.

Signal regions in the lep-had (SR LH) and had-had (SR HH) selections are designed to maximise the discovery sensitivity. The `BinomialExpZ` function of the RooStats package [117] is used for the optimisation procedure, since it allows a fast evaluation of the expected sensitivity of a selection. The experiences from the Run 1 analysis as well as new ideas are considered in the design of the regions. A set of variables

with significant discrimination power is assembled and exhaustive sensitivity scans over possible cut combinations in this set of variables are performed. The resulting cuts, which are applied on top of the corresponding basic selections, are summarised in Table 5.5 and explained in more detail in the following subsections. The number of events remaining after each selection step can be found in Table 5.6 for both SRs.

Table 5.5.: Selection criteria for the lep-had and had-had SRs.

lep-had SR	had-had SR
opposite sign between ℓ, τ	opposite sign between τ_1, τ_2
$n_{b\text{-jets}} \geq 1$	$n_{b\text{-jets}} \geq 1$
$E_{\mathrm{T}}^{\mathrm{miss}} > 230$ GeV	$E_{\mathrm{T}}^{\mathrm{miss}} > 200$ GeV
$m_{\mathrm{T2}}(\ell, \tau) > 100$ GeV	$m_{\mathrm{T2}}(\tau_1, \tau_2) > 80$ GeV

Table 5.6.: Number of events of the signal benchmark point at $m_{\tilde{t}_1} = 1100$ GeV, $m_{\tilde{\tau}_1} = 590$ GeV passing each selection step. The lep-had SR is shown on the left, the had-had SR on the right. The raw number of MC events generated as well as the effective estimated event yields weighted to 36.1 fb^{-1} are given.

Selection step (LH)	raw number	weighted	Selection step (HH)	raw number	weighted
No selection	10000	110.90	No selection	10000	110.90
Preselection	813	9.21	Preselection	789	9.38
$p_{\mathrm{T}}(\tau) > 70$ GeV	686	7.86	$p_{\mathrm{T}}(\tau_1) > 70$ GeV	773	9.20
at least one b-jet	648	7.35	at least one b-jet	725	8.55
opposite sign	640	7.28	opposite sign	708	8.35
$m_{\mathrm{T2}}(\ell, \tau) > 100$ GeV	365	4.22	$m_{\mathrm{T2}}(\tau_1, \tau_2) > 80$ GeV	455	5.34
$E_{\mathrm{T}}^{\mathrm{miss}} > 230$ GeV	281	3.26	$E_{\mathrm{T}}^{\mathrm{miss}} > 200$ GeV	394	4.70

Lep-Had Signal Region

The lep-had channel has a final-state signature of one light lepton, one τ_{had}, two b-jets, and $E_{\mathrm{T}}^{\mathrm{miss}}$ from the five neutrinos and the two $\tilde{G}$.

Due to the production of a $\tilde{t}_1\tilde{t}_1^*$ pair, the two tau leptons in the final state will have opposite signs. The charge identification of the light lepton and the τ_{had} is good enough to use an opposite-sign requirement without rejecting a significant amount of events of the signal process. The opposite sign requirement mostly targets background processes containing a real light lepton and a fake τ_{had}, e.g. the W+jets process. For the $t\bar{t}$ process, where one of the W bosons decays leptonically and the other one to a jet, the opposite sign selection can suppress its contribution as well. The direct hadronic decay of a W boson gives rise to two jets from quarks, where the jets only have fractional net charges. The charge identification of the $\tau_{\text{had-vis}}$ reconstruction is optimised for real $\tau_{\text{had-vis}}$, therefore jets accidentally reconstructed as $\tau_{\text{had-vis}}$ are more likely to be assigned the wrong charge.

Figure 5.8 (a) shows the N-1 plot[4] for the opposite sign selection. The signal process virtually always has the correct charge assignment. A significant part of the $t\bar{t}$ process with events containing fake τ_{had}, and other backgrounds with lower contributions, are rejected. This cut is therefore useful to suppress fake contributions while maintaining a very high signal efficiency.

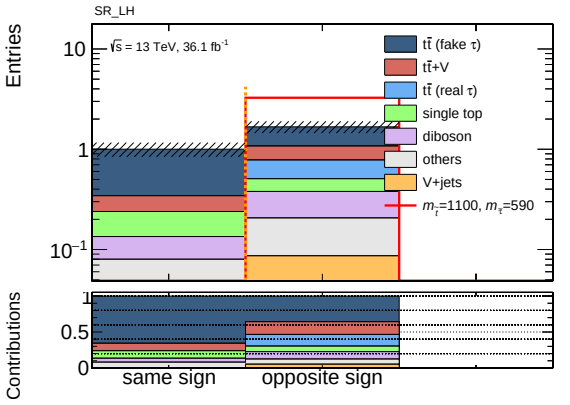

(a) Opposite-sign selection.

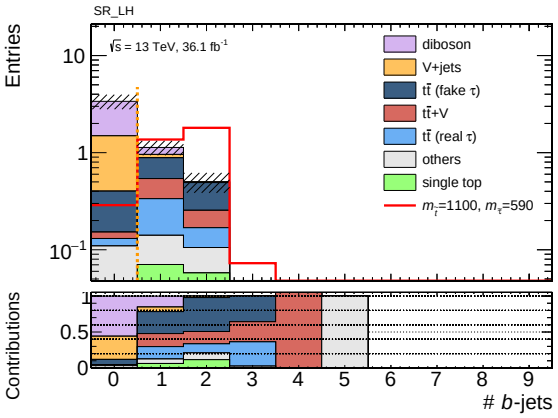

(b) Number of b-jets per event.

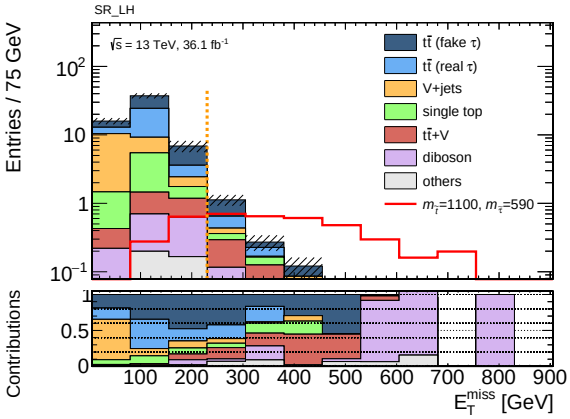

(c) $E_{\text{T}}^{\text{miss}}$ distribution.

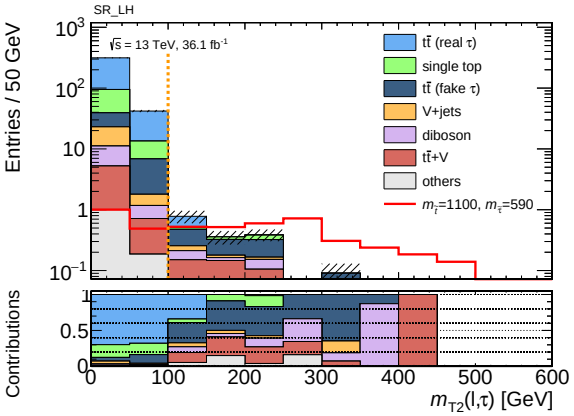

(d) $m_{\text{T2}}(\ell, \tau)$ distribution.

Figure 5.8.: N-1 plots for the lep-had SR. All processes are scaled to the collected integrated luminosity of 36.1 fb^{-1}. The relative contribution of each SM process per bin is given in the bottom pad. The normalisations of the processes are taken directly from theory. Fake contributions are taken from simulation and explicitly shown for the $t\bar{t}$ process. The hatched band indicates the statistical uncertainty of the MC estimation.

The impact of the b-jet requirement can be seen in Figure 5.8 (b). All other cuts being applied, this cut mostly rejects the remaining contributions from the VV and the V+jets processes — both of the processes lack genuine b-jets in their tree-level diagrams. The b-jet requirement efficiently selects all processes involving top-quarks including the signal process.

[4] An N-1 plot shows the distribution of a variable used in the selection of a region, with all cuts but the cut on this variable applied.

For the SM background processes, the only particles escaping undetected are neutrinos. The parent particles producing the neutrinos are lighter than the superpartners considered in this analysis. Therefore, the neutrinos originating from SM processes will have less energy. Figure 5.8 (c) shows the distribution of $E_{\mathrm{T}}^{\mathrm{miss}}$ with all other cuts applied. Most of the SM background processes have significantly lower $E_{\mathrm{T}}^{\mathrm{miss}}$ than events of the signal process. Especially the Z+jets process, which does not have genuine sources of $E_{\mathrm{T}}^{\mathrm{miss}}$, is efficiently rejected by the cut at 230 GeV.

Finally, the main discriminating variable in the lep-had channel is $m_{\mathrm{T2}}(\ell, \tau)$ (cf. Figure 5.8 (d)). The simulated signal at the benchmark mass points has a rather flat distribution in $m_{\mathrm{T2}}(\ell, \tau)$. On the one hand, the signal process has a light lepton and a τ_{had} originating from heavy parent particles leading to large m_{T} on both branches considered by m_{T2}. On the other hand, it has additional sources of $E_{\mathrm{T}}^{\mathrm{miss}}$, in the form of neutrinos and $\tilde{G}$s, which can deteriorate the performance of m_{T2}. The $t\bar{t}$ process with a real τ_{had} in principle has a cutoff of $m_{\mathrm{T2}}(\ell, \tau)$ at m_W, since both leptons originate from W bosons, which satisfies the previously discussed assumptions of m_{T2}. Events can nevertheless exceed a $m_{\mathrm{T2}}(\ell, \tau)$ value of m_W due to detector-resolution effects, due to the additional neutrinos in the leptonic τ decay, or simply due to the selection of the wrong objects.

The main contribution from the $t\bar{t}$ process is not from the sub-process with a real τ_{had}. Most of the remaining events from the $t\bar{t}$ process after applying the $m_{\mathrm{T2}}(\ell, \tau)$ cut have a tau which is faked by a jet that does not necessarily need to originate from the decay products of the W boson. If the wrong object, in that case the fake τ_{had}, is used in the calculation of $m_{\mathrm{T2}}(\ell, \tau)$, the basic assumption breaks down and $m_{\mathrm{T2}}(\ell, \tau)$ is not bounded from above by m_W any more. The lowest bin in $m_{\mathrm{T2}}(\ell, \tau)$ contains a significant amount of events from all processes, which can be explained by the trivial minimisation discussed in Section 5.4.

The estimated contribution of signal and background processes, based solely on the expectation from simulated samples, is summarised in Table 5.7. Major contributions arise from the $t\bar{t}$ process as well as from the $t\bar{t} + V$ and VV processes. The events contributing to the VV process mostly have two (in about $\frac{2}{3}$ of the events) or three (in about $\frac{1}{3}$ of the events) charged leptons in the final state. The dominant contribution of the $t\bar{t} + V$ process are events where the massive vector boson is a Z boson decaying to a pair of neutrinos ($t\bar{t} + [Z \to \nu\nu]$), giving rise to additional $E_{\mathrm{T}}^{\mathrm{miss}}$ and thus mimicking the signal process.

Had-Had Signal Region

The had-had SR targets the final state of the signal process where both tau leptons decay hadronically. The selection criteria are optimised with a similar approach as used in the lep-had channel. In the computation of m_{T2} and the opposite sign requirement, the light lepton is replaced by the sub-leading τ_{had} (τ_2).

The lep-had and had-had channels have comparable branching fractions (cf. Section 2.3), therefore the expected signal yields are roughly the same for both channels. As discussed in Section 3.2, the had-had channel has significantly smaller contributions of the W+jets and $t\bar{t}$ processes in comparison to the lep-had channel allowing to design a looser set of requirements, while maintaining the same level of signal-to-background

Table 5.7.: Expected yields in the lep-had (left) and had-had (right) SRs. All processes are scaled to the collected integrated luminosity of 36.1 fb^{-1}. The normalisations of the processes are taken directly from theory. Only the statistical uncertainties from the MC estimation are quoted here.

	SR_LH		SR_HH	
	exp. events	(contr.)	exp. events	(contr.)
$m_{\tilde{t}} = 1100, m_{\tilde{\tau}} = 590$	3.26 ± 0.24	195 %	4.70 ± 0.27	$(2.6) \times 10^2$ %
diboson	0.17 ± 0.06	10.4 %	0.29 ± 0.07	16 %
V+jets	0.09 ± 0.04	5.2 %	0.26 ± 0.12	14 %
others	0.119 ± 0.031	7.1 %	0.09 ± 0.07	5 %
single top	0.13 ± 0.04	7.7 %	0.13 ± 0.05	7.3 %
$t\bar{t} + V$	0.30 ± 0.08	18 %	0.19 ± 0.07	10 %
$t\bar{t}$ (fake τ)	0.60 ± 0.14	36 %	0.50 ± 0.17	28 %
$t\bar{t}$ (real τ)	0.27 ± 0.13	16 %	0.35 ± 0.18	19 %
total background	1.67 ± 0.23		1.81 ± 0.30	

separation.

Figure 5.9 (a) shows the opposite sign requirement of the two τ_{had}, mostly rejecting events from the $t\bar{t}$ process with at least one fake τ_{had}. Due to the high $E_{\text{T}}^{\text{miss}}$ requirement already being applied, the V+jets process mostly contains events from the W+jets process. In these events at least one of the τ_{had} is faked by a jet.

The b-jet signature in the had-had channel is the same as in the lep-had channel, therefore the optimisation procedure also yielded a requirement on the number of b-jets of at least one. Figure 5.9 (b) shows the distribution of events as a function of the number of b-jets, where the VV and Z+jets processes are efficiently rejected, while top-related background processes, including the signal process, are retained.

The $E_{\text{T}}^{\text{miss}}$ cut in the had-had channel is placed at 200 GeV, making the selection looser than in the lep-had channel. Figure 5.9 (c) shows the $E_{\text{T}}^{\text{miss}}$ distribution for the SM background processes and a benchmark point for the signal process, where the signal process tends to have higher values of $E_{\text{T}}^{\text{miss}}$, while the SM background processes are mostly located at lower values.

Given that the background contributions are lower than in the lep-had channel, also a looser cut on $m_{\text{T2}}(\tau_1, \tau_2)$ is used. The suppression of most of the SM processes can be seen in Figure 5.9 (d). While rejecting a large part of the contribution from the signal process, the cut on $m_{\text{T2}}(\tau_1, \tau_2)$ still outperforms the other cuts in terms of background rejection.

The summary of the expected contributions of signal and background processes is given in Table 5.7. The dominant contribution to the events from background processes are events from the $t\bar{t}$ process with at least one faked τ_{had}. Further important background processes are the $t\bar{t}$ process with real τ_{had}, the VV process (about $\frac{1}{3}$ of the events with two and $\frac{2}{3}$ with three charged leptons), and the $t\bar{t} + V$ process, where the main contribution is also $t\bar{t} + [Z \to \nu\nu]$.

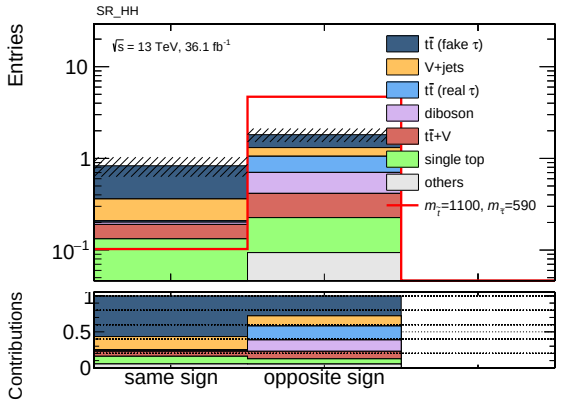

(a) Opposite-sign selection.

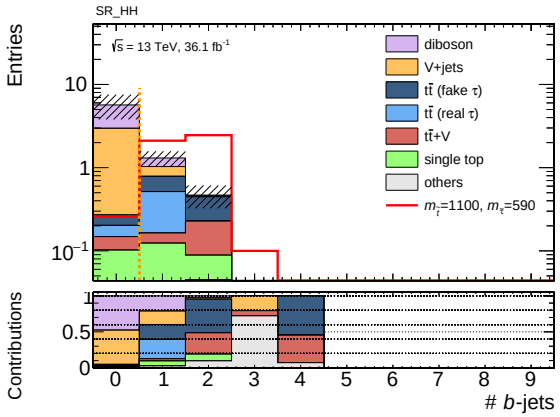

(b) Number of b-jets per event.

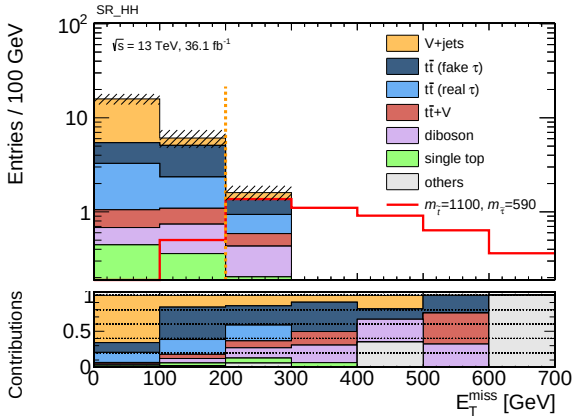

(c) $E_{\mathrm{T}}^{\mathrm{miss}}$ distribution.

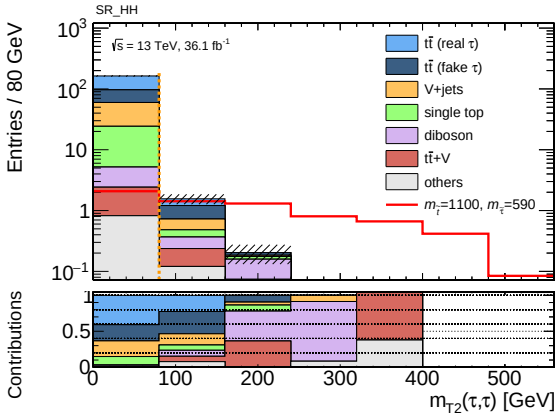

(d) $m_{\mathrm{T2}}(\tau_1, \tau_2)$ distribution.

Figure 5.9.: N-1 plots for the had-had SR. All processes are scaled to the collected integrated luminosity of 36.1 fb^{-1}. The relative contribution of each SM process per bin is given in the bottom pad. The normalisations of the processes are taken directly from theory. Fake contributions are taken from simulation and explicitly shown for the $t\bar{t}$ process. The hatched band indicates the statistical uncertainty of the MC estimation.

5.6. Background Estimation

In order to improve the estimation of background processes with major contributions to the SRs, CRs are defined in all three selections. As discussed in the last section, in the SRs the $t\bar{t}$ process is efficiently suppressed by the m_{T2} requirements. Therefore, the CRs for the $t\bar{t}$ process are defined in the same selections as the SRs by inverting the m_{T2} requirements. For the lep-had channel, the contributions of processes containing fake τ_{had} are estimated with a dedicated, data-driven fake-factor method (FFM). Validation regions (VRs) for the $t\bar{t}$ estimation as well as the fake-τ_{had} estimation are defined for both SRs in the respective selections.

Finding a pure[5] selection with sufficient statistics for the VV and $t\bar{t}+Z$ processes is

[5]In this context the purity is defined as the ratio of events of the process targeted with respect to the total

more challenging. Therefore, the dedicated common-CR selection was developed. Since the lep-had as well as the had-had selections contain b-jet requirements, the contribution of the VV process is significantly suppressed. Lifting the b-jet requirement and employing additional cuts in a leptonic selection targeted on this process allows to design a CR. For the $t\bar{t}+V$ process, the main contribution to the SRs is the associated production with $Z \to \nu\nu$. Due to the undetected neutrinos, this is inherently hard to select, therefore the CR selection for the $t\bar{t}+Z$ process targets a final state with the Z boson decaying to charged leptons to determine the $t\bar{t}+Z$ normalisation.

In the following, the general strategy of the background estimations employed in this analysis is given and the estimation of the multi-jet contribution is discussed. Afterwards, the definitions of the CRs and VRs are explained in more detail, and the description of the FFM follows.

5.6.1. General Strategy

The major background processes are normalised in dedicated CRs, optimised for high purity, while being kinematically as close to the SRs as possible. All CRs, VRs, and SRs were kept blinded during the development of the background estimation strategy and were unblinded in this order.

The CRs have to have a mutually disjoint selection with respect to all other regions in order to be statistically independent.[6] Furthermore, mutually disjoint VRs are used to verify that the extrapolation of the variables inverted with respect to the SR is valid. The VRs are therefore located in the phase space between the CR and the corresponding SR. In the VRs, the normalised background process to be validated should have a significant contribution and the signal contamination should not be too large. The VRs are unblinded after the background-estimation strategy is fixed and do not contribute in the final statistical evaluation.

Another important aspect of the background estimation strategy is the special treatment of fake contributions. In the context of this analysis, processes, especially $t\bar{t}$, can be split into a *fake* and a *real* component. The real component (e.g. $t\bar{t}$ with real τ_{had}) contains all events where the selected τ_{had} (one in the lep-had and two in the had-had channel) are all real, i.e. the reconstructed object is matched to a true τ_{had}. The fake component (e.g. $t\bar{t}$ with fake τ_{had}) contains the remaining events where at least one τ_{had} is not matched to a true τ_{had}. Therefore, this discrimination can only be done on simulated samples. For the discrimination of fake and real τ_{had}, the source of the fake τ_{had} (mostly jets) is not considered.

5.6.2. Multi-jet Contribution

As discussed in Section 3.2, the multi-jet process has a large cross section at the LHC. Therefore, it was verified that its contribution to the relevant selections is negligible. In previous studies, data-driven approaches were used for the lep-had as well as the had-had selection to estimate the multi-jet contribution [115, 116]. The method is outlined shortly in the following.

expectation from all SM processes

[6] The details of the treatment of all regions in the statistical evaluation will be given in Section 5.8.

Multi-jet events enter the lep-had or had-had selections due to jets faking τ_{had}. The reconstructed charge of the fake τ_{had} is assumed to be mostly independent of the other object (ℓ or τ_{had}), which is consistent with the findings using a di-jet MC sample in a very loose selection. Therefore, when selecting the two objects ($\ell + \tau_{\text{had}}$ or $\tau_{\text{had}} + \tau_{\text{had}}$) of the respective channels, the multi-jet contribution should be about the same for the opposite- and the same-sign selection. Using the MC estimation for all other background processes in the same-sign selection (N_{SS}^{MC}) and the number of observed data events in the same selection (N_{SS}^{data}), one can estimate the multi-jet contribution in the opposite-sign region (N_{OS}^{mj}) with

$$N_{OS}^{\text{mj}} \approx N_{SS}^{\text{mj}} = N_{SS}^{\text{data}} - N_{SS}^{\text{MC}}$$

and determine a closure with the number of observed opposite-sign data events (N_{OS}^{data}) and the corresponding other MC-based background processes (N_{OS}^{MC})

$$N_{OS}^{\text{mj}} = N_{OS}^{\text{data}} - N_{OS}^{\text{MC}}.$$

For both the lep-had and the had-had selection, studies were carried out using this method. Both studies show closure and negligible contributions to the phase-space used in this analysis — even at pre-selection level. Multi-jet events do not contain significant genuine sources of $E_{\text{T}}^{\text{miss}}$, and the b-jet contribution is expected to be rather small. Events with high jet momenta are also rare, therefore the number of events with high p_{T} of the fake τ_{had} will be small. The combination of these requirements cause strong rejection of the multi-jet contribution already at the preselection level. Therefore, in the following the multi-jet contribution is neglected and only mentioned in case of very loose selections.

5.6.3. Control and Validation Regions in the Lep-had Channel

The lep-had selection, which is used as baseline for the lep-had SR, is naturally enriched in $t\bar{t}$ events. The requirement to have a light lepton of signal quality, a τ_{had}, and a b-jet not only fulfils the signal signature, but is also a possible final state of the $t\bar{t}$ process. Therefore, it seems natural to estimate the $t\bar{t}$ process in this selection. A schematic overview of the setup of the different regions discussed in the following can be found in Figure 5.10. The regions are described in detail in the following.

The two variables $m_{\text{T2}}(\ell, \tau)$ and $m_{\text{T}}(\ell)$ are especially important for the design of these regions. Figure 5.11 shows both variables in the lep-had selection with an additional $E_{\text{T}}^{\text{miss}}$ requirement. $m_{\text{T2}}(\ell, \tau)$ is used to ensure that control, validation, and signal regions are mutually disjoint. Since the signal region is located at high $m_{\text{T2}}(\ell, \tau)$, a control region can be placed at low values and the extrapolation validated in the phase space in between.

$m_{\text{T}}(\ell)$ on the other hand, is found to be a variable discriminating events with fake and real τ_{had} in the $t\bar{t}$ process. The construction of $m_{\text{T}}(\ell)$ is based on the p_{T} of the light lepton and the $E_{\text{T}}^{\text{miss}}$, and therefore only indirectly affected by the decay of the other W boson. For the $t\bar{t}$ process the expected cut-off for W bosons, as discussed in Section 5.4, is only fulfilled in events where one W boson decays promptly to a light lepton and the other decays hadronically, i.e. $t\bar{t}$ events with fake τ_{had}. Events involving decays of W bosons to tau leptons introduce additional neutrinos, which in turn deteriorate the $m_{\text{T}}(\ell)$ performance, resulting in a distribution of the $t\bar{t}$ contribution with real τ_{had} spread out far beyond the cut-off at m_W.

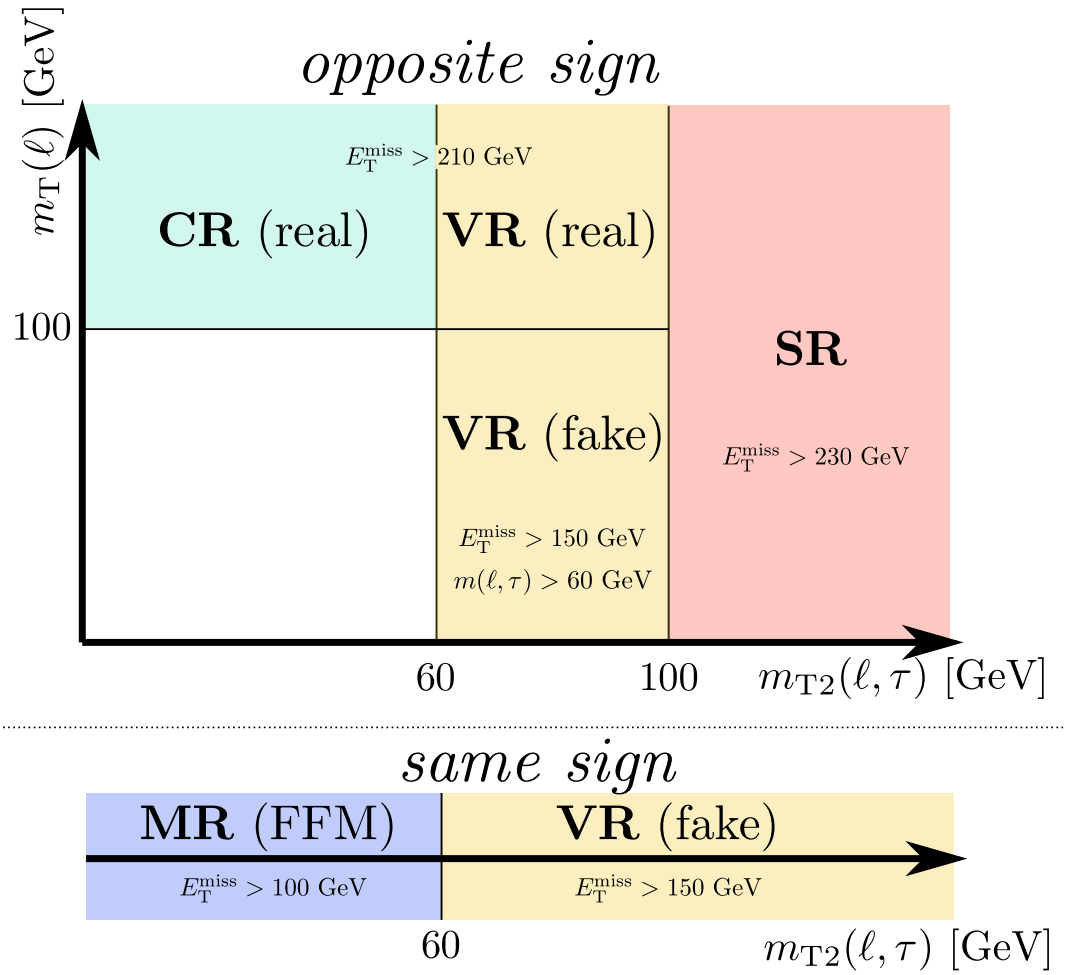

Figure 5.10.: Schematic drawing of the setup of the CRs and VRs for the $t\bar{t}$ process, the measurement region for the fake-factor method and the SR in the lep-had channel. The opposite-sign selection is shown at the top, while the same-sign selection is given at the bottom. On the horizontal axis, the regions have increasing requirements on $m_{\mathrm{T2}}(\ell,\tau)$. In the opposite-sign selection the requirements on $m_{\mathrm{T}}(\ell)$ increase on the vertical axis. The cut on $E_{\mathrm{T}}^{\mathrm{miss}}$ and $m(\ell,\tau)$ is optimised individually for each region and displayed in the drawing.

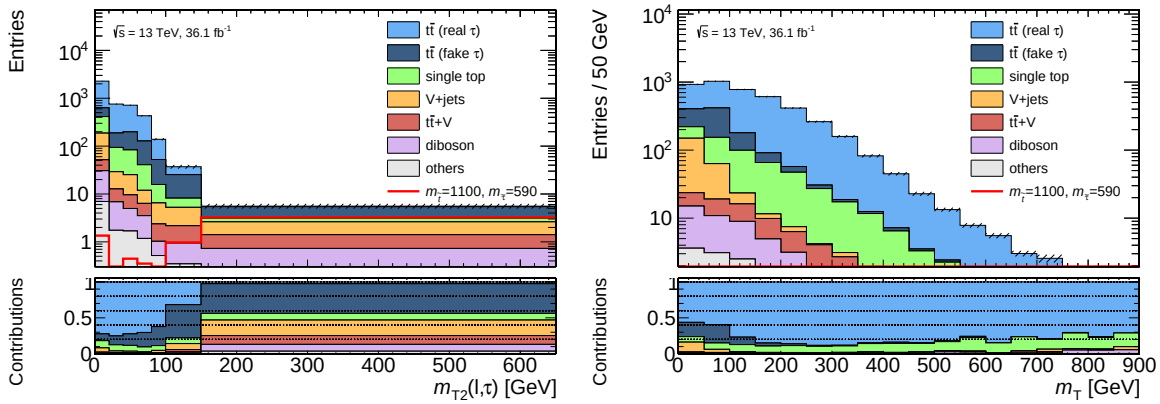

Figure 5.11.: $m_{\mathrm{T2}}(\ell,\tau)$ (left) and $m_{\mathrm{T}}(\ell)$ (right) distribution in the lep-had selection with an additional requirement of $E_{\mathrm{T}}^{\mathrm{miss}} > 100$ GeV. All processes are scaled to the collected integrated luminosity of 36.1 fb^{-1}. The relative contribution of each SM process per bin is given in the bottom pad. The normalisations of the processes are taken directly from theory. Fake contributions are taken from simulation and explicitly shown for the $t\bar{t}$ process. The hatched band indicates the statistical uncertainty of the MC estimation.

Control Regions

A CR for $t\bar{t}$ events with real τ_{had} (CR LH $t\bar{t}$-real) is defined at $m_{\mathrm{T2}}(\ell,\tau) < 60$ GeV. The $E_{\mathrm{T}}^{\mathrm{miss}}$ requirement is loosened with respect to the SR to 210 GeV, in order to get sufficient statistics (cf. Figure 5.12 (a)). As in the SR, an opposite sign requirement is imposed to reject contributions with fake τ_{had}. To further increase the purity of $t\bar{t}$ events with real τ_{had}, a requirement on $m_{\mathrm{T}}(\ell)$ of at least 100 GeV is introduced, as can be seen in Figure 5.12 (b).

The left-hand column in Table 5.8 shows the expected contributions of the considered SM processes and a benchmark point of the signal process. The contribution of the process of interest, $t\bar{t}$ with real τ_{had}, is 77.0 %, with the sub-dominant contribution from the single top processes yielding about 19 % of the total expected SM events. The contributions of the other processes are of the order of a few percents. The expected number of events of the process targeted is 214, ensuring a low statistical uncertainty on the normalisation factor.

At low values of $m_{\mathrm{T}}(\ell)$, a CR enriched in $t\bar{t}$ events with fake τ_{had} could be placed. This CR was used for the preliminary results [2]. Due to the estimation of the fake contribution with the FFM, this region is not needed any more and therefore left blank in Figure 5.10.

Validation Regions

In total, three VRs target the $t\bar{t}$ process in the lep-had selection. One of them validates the extrapolation of the component of the $t\bar{t}$ process with real τ_{had} (VR LH $t\bar{t}$-real), the other two are enriched in fake τ_{had} and make use of the opposite- (VR LH $t\bar{t}$-fake (OS)) and same-sign (VR LH $t\bar{t}$-fake (SS)) selection.

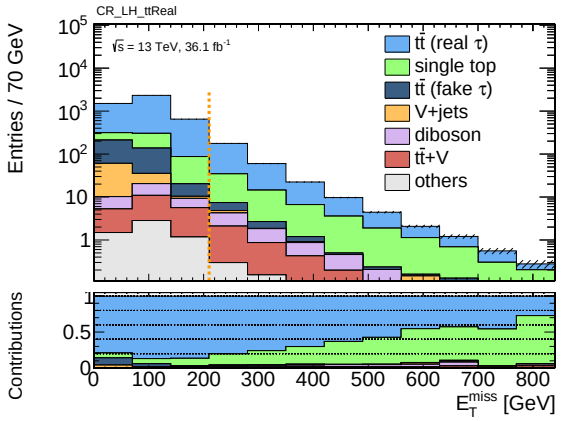

(a) $E_{\mathrm{T}}^{\mathrm{miss}}$ distribution.

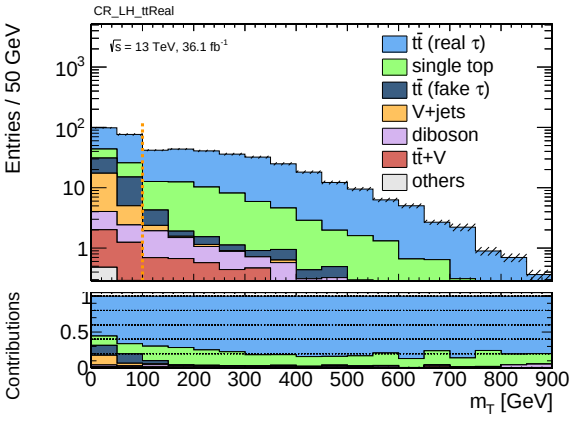

(b) m_{T} distribution.

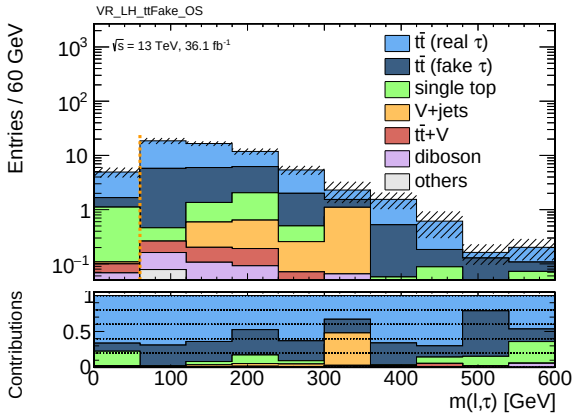

(c) $m(\ell, \tau)$ distribution in the opposite-sign selection.

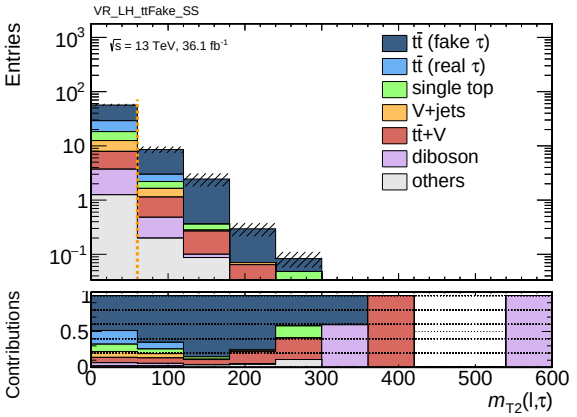

(d) $m_{\mathrm{T2}}(\ell, \tau)$ distribution in the same-sign selection.

Figure 5.12.: N-1 plots for the lep-had $t\bar{t}$ CR (top) and the VRs for $t\bar{t}$ events with fake τ_{had} (bottom). All processes are scaled to the collected integrated luminosity of 36.1 fb^{-1}. The relative contribution of each SM process per bin is given in the bottom pad. The normalisations of the processes are taken directly from theory. Fake contributions are taken from simulation and explicitly shown for the $t\bar{t}$ process. The hatched band indicates the statistical uncertainty of the MC estimation.

Table 5.8.: Expected yields of the lep-had CR and VR for $t\bar{t}$ events with a real τ_{had}. All processes are scaled to the collected integrated luminosity of 36.1 fb^{-1}. The normalisations of the processes are taken directly from theory. Only the statistical uncertainties from the MC estimation are quoted here.

	CR_LH_ttReal		VR_LH_ttReal	
	exp. events	(contr.)	exp. events	(contr.)
$m_{\tilde{t}} = 1100, m_{\tilde{\tau}} = 590$	0.73 ± 0.11	0.26 %	0.25 ± 0.06	1.27 %
diboson	4.12 ± 0.26	1.48 %	0.27 ± 0.06	1.40 %
V+jets	0.7 ± 0.4	0.25 %	0.12 ± 0.09	0.6 %
others	0.61 ± 0.07	0.219 %	0.100 ± 0.024	0.52 %
single top	51.7 ± 1.3	18.6 %	3.3 ± 0.4	16.8 %
$t\bar{t} + V$	3.16 ± 0.23	1.13 %	0.30 ± 0.07	1.5 %
$t\bar{t}$ (fake τ)	3.8 ± 0.7	1.37 %	0.63 ± 0.17	3.3 %
$t\bar{t}$ (real τ)	214 ± 4	77.0 %	14.7 ± 1.3	75.8 %
total background	278 ± 4		19.3 ± 1.4	

The VR for $t\bar{t}$ events with real τ_{had} has the same cuts as the CR, but the $m_{\text{T2}}(\ell, \tau)$ requirement is placed in the window of 60–100 GeV. As $m_{\text{T2}}(\ell, \tau)$ falls steeply in that range, the statistics of this VR is very small. About 15 events of the target process $t\bar{t}$ with real τ_{had} are expected before normalisation, yielding a predicted purity of 76 %. The expected yields of all processes simulated are summarised in Table 5.8.

Complementary to the VR for real τ_{had}, a VR for the fake estimate is designed in the opposite-sign selection at low $m_{\text{T}}(\ell)$ ($m_{\text{T}}(\ell) < 100$ GeV). A small gain in purity is achieved using a cut on $m(\ell, \tau)$ at 60 GeV (cf. Figure 5.12 (c)). The $E_{\text{T}}^{\text{miss}}$ requirement is relaxed to 150 GeV in order to increase the available statistics. In this region about 17 events of the targeted process, $t\bar{t}$ with fake τ_{had}, are expected from the simulated samples (cf. also Table 5.9). The purity of about 30 % is very poor. Most of the contamination of this VR originates from $t\bar{t}$ events with real τ_{had}. This VR is called "fake" VR due to the process targeted, but can be used to validate events with real as well as fake τ_{had} simultaneously.

In order to obtain a VR with higher purity, an additional same-sign VR is defined. Since the SR is mutually disjoint to the VR due to the same-sign requirement, an inclusive cut on $m_{\text{T2}}(\ell, \tau) > 60$ GeV is chosen (cf. Figure 5.12 (d)). This cut makes the VR at the same time mutually disjoint to the measurement region of the FFM. As in the opposite-sign VR, the $E_{\text{T}}^{\text{miss}}$ requirement is loosened to 150 GeV in order to get reasonable statistics. Table 5.9 shows the yields expected from the simulated samples on the right. This VR has a high purity of about 70 % events from the $t\bar{t}$ process with fake τ_{had}, while the contamination from other processes is small.

5.6.4. Control and Validation Regions in the Had-had Channel

The overall approach for the had-had channel is similar to the lep-had channel. Since the light lepton effectively is replaced by the second τ_{had}, some differences arise. For

Table 5.9.: Expected yields of the lep-had VRs for $t\bar{t}$ events with fake τ_{had} (left: opposite-sign region, right: same-sign region). All processes are scaled to the collected integrated luminosity of 36.1 fb^{-1}. The normalisations of the processes are taken directly from theory. Only the statistical uncertainties from the MC estimation are quoted here.

	VR_LH_ttFake_OS		VR_LH_ttFake_SS	
	exp. events	(contr.)	exp. events	(contr.)
$m_{\tilde{t}} = 1100, m_{\tilde{\tau}} = 590$	0.22 ± 0.06	0.38 %	0.037 ± 0.018	0.32 %
diboson	0.35 ± 0.07	0.61 %	0.34 ± 0.11	3.0 %
V+jets	1.3 ± 1.3	2.2 %	0.52 ± 0.26	4.6 %
others	0.19 ± 0.07	0.33 %	0.31 ± 0.06	2.7 %
single top	3.2 ± 0.9	5.6 %	0.65 ± 0.13	5.7 %
$t\bar{t} + V$	0.36 ± 0.08	0.63 %	0.90 ± 0.11	7.8 %
$t\bar{t}$ (fake τ)	17.2 ± 1.8	29.7 %	7.9 ± 1.2	69 %
$t\bar{t}$ (real τ)	35.2 ± 2.7	60.9 %	0.8 ± 0.6	7 %
total background	58 ± 4		11.5 ± 1.3	

the discrimination of control, validation and signal regions $m_{\text{T2}}(\tau_1, \tau_2)$ is used, where the light lepton is replaced by the second τ_{had}. The introduction of the second τ_{had} makes m_{T} ambiguous, therefore the τ_{had} with the higher p_{T} is used ($m_{\text{T}}(\tau_1)$). The individual cuts are optimised independently of the lep-had channel and therefore differ. The performance of the discriminating variables changes, on the one hand the ambiguities of the τ_{had} are introduced, but on the other hand there are only two neutrinos from the two τ_{had} decays, while in the lep-had mode of the two tau leptons, there are three neutrinos. The cut values are in general looser due to the significantly reduced contribution of the $t\bar{t}$ process. Figure 5.13 summarises the cuts applied in the had-had regions in a schematic drawing.

Control Regions

Since the had-had channel does not apply the FFM, a CR for $t\bar{t}$ events with fake τ_{had} (CR HH $t\bar{t}$-fake) and one CR for events with only real τ_{had} (CR HH $t\bar{t}$-real) is defined. Two separate normalisations are derived for the fake and the real τ_{had} component of the $t\bar{t}$ process.

The CR for $t\bar{t}$ events with real τ_{had} has an upper cut on $m_{\text{T2}}(\tau_1, \tau_2)$ at 30 GeV to achieve a mutually disjoint selection with respect to the signal region. To increase the contribution of events with real τ_{had}, analogously to the lep-had channel, a requirement of $m_{\text{T}}(\tau_1) > 70$ GeV (cf. Figure 5.14 (a)) and an opposite-sign cut is used. In order to increase the statistics of the CR, the $E_{\text{T}}^{\text{miss}}$ requirement is relaxed with respect to the SR to 120 GeV. A minimum requirement on $m(\tau_1, \tau_2)$ of 70 GeV is used to reject events from the Z+jets process (cf. Figure 5.14 (b)). Table 5.10 (left column) shows the expected contributions to the CR. The purity of events with real τ_{had} in the $t\bar{t}$ process is about 68 %, with the main contamination from events with fake τ_{had}.

To select $t\bar{t}$ events with fake τ_{had}, $m_{\text{T}}(\tau_1)$ is inverted with respect to the selection of the

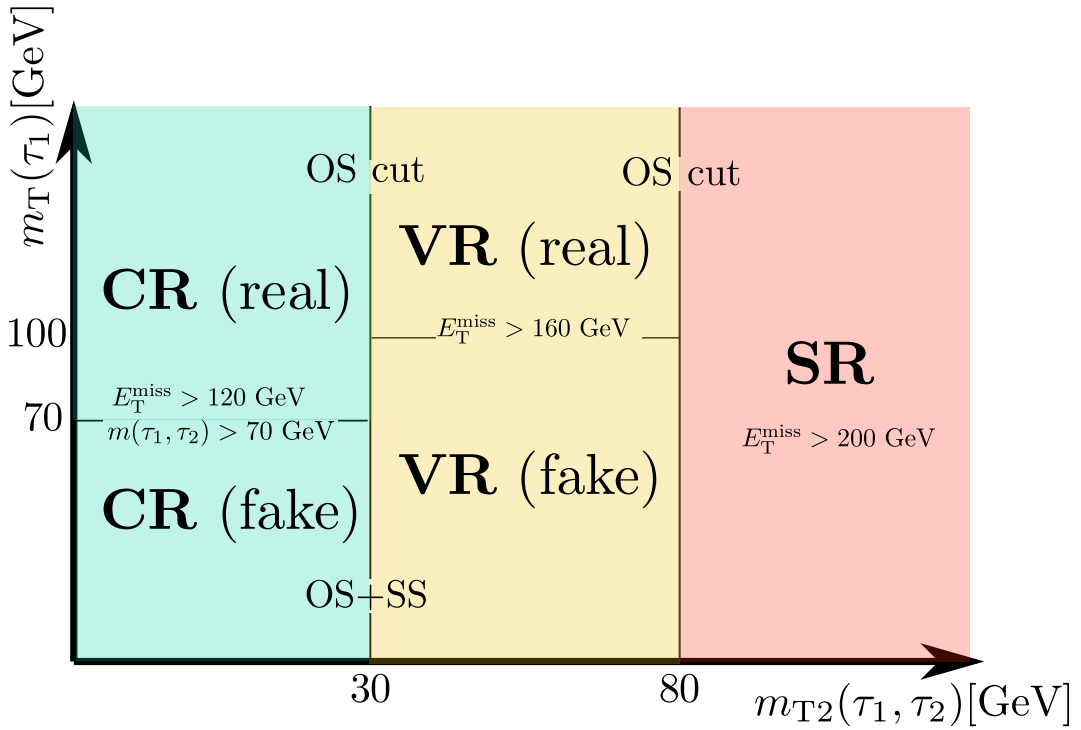

Figure 5.13.: Schematic drawing of the setup of the CRs and VRs for the $t\bar{t}$ process and the SR in the had-had selection. On the horizontal axis, $m_{\mathrm{T2}}(\tau_1, \tau_2)$ is separating control, validation and signal region. $m_{\mathrm{T}}(\tau_1)$ separates on the vertical axis fake from the real τ_{had} control and validation regions. The two regions for the $t\bar{t}$ process with fake τ_{had} are agnostic about the relative signs of the charges of the two τ_{had}.

Table 5.10.: Expected yields of the had-had CRs for $t\bar{t}$ events with real (left) and fake (right) τ_{had}. All processes are scaled to the collected integrated luminosity of 36.1 fb^{-1}. The normalisations of the processes are taken directly from theory. Only the statistical uncertainties from the MC estimation are quoted here.

	CR_HH_ttReal		CR_HH_ttFake	
	exp. events	(contr.)	exp. events	(contr.)
$m_{\tilde{t}} = 1100, m_{\tilde{\tau}} = 590$	1.49 ± 0.16	1.11 %	0.33 ± 0.07	0.25 %
diboson	1.41 ± 0.25	1.05 %	1.33 ± 0.27	0.99 %
V+jets	5.9 ± 2.0	4.4 %	21.2 ± 2.2	15.9 %
others	0.28 ± 0.08	0.20 %	0.69 ± 0.13	0.52 %
single top	12.4 ± 1.3	9.2 %	18.4 ± 1.4	13.8 %
$t\bar{t} + V$	1.00 ± 0.13	0.74 %	1.37 ± 0.17	1.03 %
$t\bar{t}$ (fake τ)	21.7 ± 2.4	16.1 %	46.7 ± 2.7	35.0 %
$t\bar{t}$ (real τ)	92 ± 6	68.3 %	43.8 ± 3.1	32.8 %
total background	135 ± 7		134 ± 5	

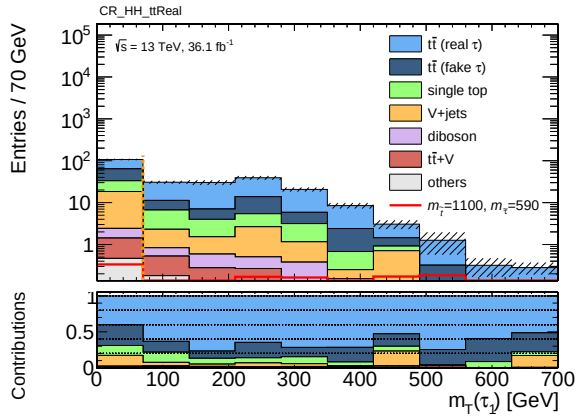

(a) $m_{\mathrm{T}}(\tau_1)$ distribution.

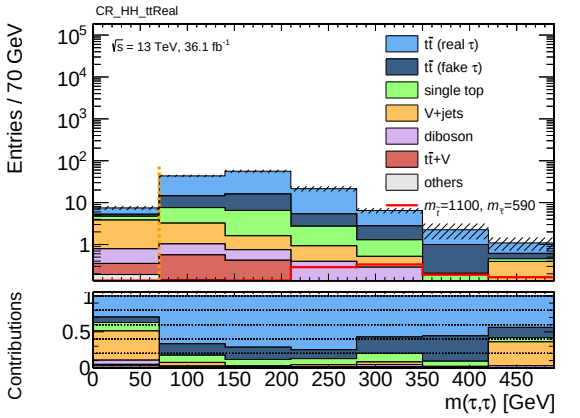

(b) $m(\tau_1, \tau_2)$ distribution.

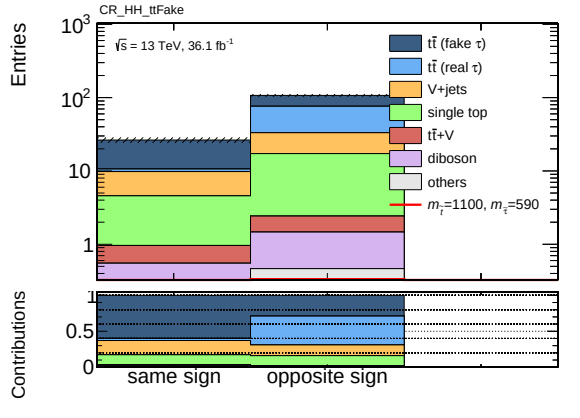

(c) Opposite-sign selection.

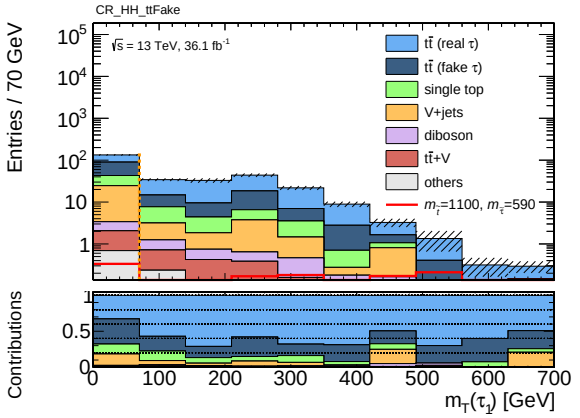

(d) $m_{\mathrm{T}}(\tau_1)$ distribution.

Figure 5.14.: N-1 plots for the had-had $t\bar{t}$ CR with real (top) and fake (bottom) τ_{had}. All processes are scaled to the collected integrated luminosity of 36.1 fb^{-1}. The relative contribution of each SM process per bin is given in the bottom pad. The normalisations of the processes are taken directly from theory. Fake contributions are taken from simulation and explicitly shown for the $t\bar{t}$ process. The hatched band indicates the statistical uncertainty of the MC estimation.

CR for real τ_{had}. To increase the contribution of events with fake τ_{had}, the opposite-sign requirement is lifted (cf. Figure 5.14 (c)). The other cuts are kept at the same values as in the CR for the $t\bar{t}$ process with real τ_{had}. The purity of $t\bar{t}$ events with fake τ_{had} is at about 35 %, with the main contamination being $t\bar{t}$ events with real τ_{had}. This is mostly due to the previously discussed, deteriorated performance of $m_{\mathrm{T}}(\tau_1)$ (cf. Figure 5.14 (d)) with respect to the lep-had channel. An important cause of the deterioration is the ambiguity in the selected τ_{had}: In the target case where one of the W bosons of the $t\bar{t}$ process decays to quarks, one of the jets gives rise to the fake τ_{had} and the other W boson decays to a real τ_{had}. Choosing the real τ_{had} for the calculation of $m_{\mathrm{T}}(\tau_1)$ yields the discussed cut-off at m_W. Choosing the fake τ_{had} on the other hand, gives a smeared out value similar to the case of events with two real τ_{had}. Since $m_{\mathrm{T}}(\tau_1)$ is defined as using the leading τ_{had} of the event, which can be either the true or the fake

Table 5.11.: Expected yields of the had-had VRs for $t\bar{t}$ events with real (left) and fake (right) τ_{had}. All processes are scaled to the collected integrated luminosity of 36.1 fb^{-1}. The normalisations of the processes are taken directly from theory. Only the statistical uncertainties from the MC estimation are quoted here.

	VR_HH_ttReal		VR_HH_ttFake	
	exp. events	(contr.)	exp. events	(contr.)
$m_{\tilde{t}} = 1100, m_{\tilde{\tau}} = 590$	0.55 ± 0.08	2.00 %	0.052 ± 0.023	0.16 %
diboson	0.29 ± 0.08	1.04 %	0.32 ± 0.06	1.01 %
V+jets	2.2 ± 0.8	7.9 %	3.4 ± 1.0	10.9 %
others	0.04 ± 0.07	0.13 %	0.07 ± 0.07	0.24 %
single top	1.6 ± 0.4	5.6 %	4.4 ± 0.7	13.9 %
$t\bar{t} + V$	0.31 ± 0.06	1.12 %	0.31 ± 0.07	0.99 %
$t\bar{t}$ (fake τ)	8.9 ± 1.5	32 %	12.9 ± 3.1	41 %
$t\bar{t}$ (real τ)	14.5 ± 1.8	52 %	10.0 ± 1.7	32 %
total background	27.8 ± 2.5		31 ± 4	

τ_{had}, the efficiency of the selection of events with fake τ_{had} is reduced.

Both CRs show cross-contamination of the real and fake contributions to the $t\bar{t}$ process. Since both processes are normalised in a simultaneous fit (cf. Section 5.8), the cross-contamination is exploited by the fit, as long as there is a sufficiently large difference in the relative contributions. In the CR for real τ_{had}, there are about 4.2 times more events with real τ_{had} than with fake τ_{had}, while in the CR for fake τ_{had} there are slightly more events with fake τ_{had} than there are events with real τ_{had}. This allows the fit to constrain both normalisation factors.

Validation Regions

The VRs in the had-had selection are set into the window between 30 and 80 GeV of $m_{\text{T2}}(\tau_1, \tau_2)$ to be able to validate the extrapolation. They are split by a $m_{\text{T}}(\tau_1)$ cut at 100 GeV, which is raised with respect to the CRs to compensate the increased $m_{\text{T2}}(\tau_1, \tau_2)$ requirement. Furthermore, they share a tightened cut on $E_{\text{T}}^{\text{miss}} > 160$ GeV in order to get closer to the SR and the requirement on $m(\tau_1, \tau_2)$ is lifted.

The VR for events with real τ_{had} (VR HH $t\bar{t}$-real) shares the opposite sign criterion with the corresponding CR. The purity in $t\bar{t}$ events with real τ_{had} of the VR is about 52 % with about 15 events expected in the target process. Contributions from all processes are summarised in the left column of Table 5.11 as expected by MC simulation. The distribution of $m_{\text{T2}}(\tau_1, \tau_2)$ is shown in Figure 5.15 (a).

The VR for events with fake τ_{had} (VR HH $t\bar{t}$-fake) at lower $m_{\text{T}}(\tau_1)$ has no requirement on the mutual sign of the charges of the τ_{had} and shares the remaining cuts with the real-τ_{had} VR. The contributions from all processes are listed in the right column of Table 5.11, showing a purity of 41 % in the target process. Figure 5.15 (b) shows the $m_{\text{T2}}(\tau_1, \tau_2)$ distribution with all other cuts applied. Due to the upper cut on $m_{\text{T}}(\tau_1)$ there are no events left at $m_{\text{T2}}(\tau_1, \tau_2) > 100$ GeV.

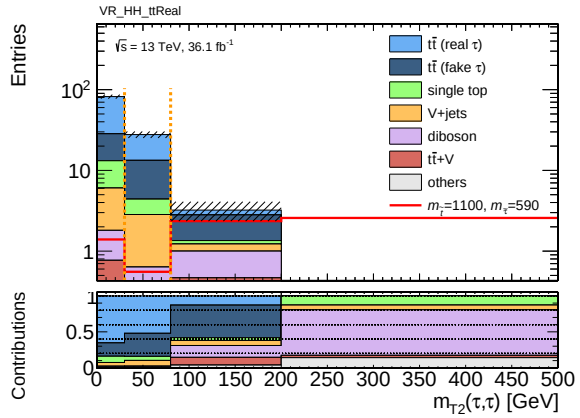

(a) $m_{\mathrm{T2}}(\tau_1, \tau_2)$ distribution.

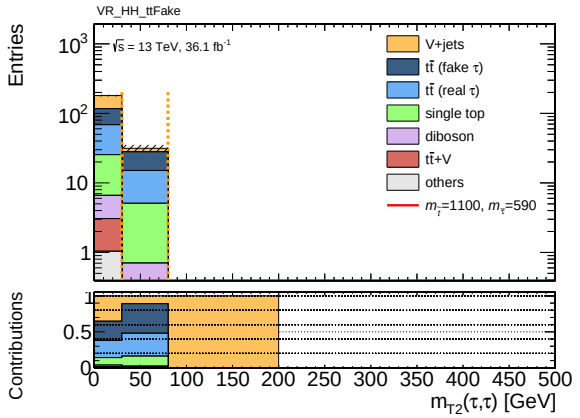

(b) $m_{\mathrm{T2}}(\tau_1, \tau_2)$ distribution.

Figure 5.15.: N-1 plots for the had-had $t\bar{t}$ VRs with real (left) and fake (right) τ_{had}. All processes are scaled to the collected integrated luminosity of 36.1 fb^{-1}. The relative contribution of each SM process per bin is given in the bottom pad. The normalisations of the processes are taken directly from theory. Fake contributions are taken from simulation and explicitly shown for the $t\bar{t}$ process. The hatched band indicates the statistical uncertainty of the MC estimation.

Table 5.12.: Selection criteria of the common CRs.

selection	CR VV	CR $t\bar{t}+V$
n_{SFOS}	≥ 1	≥ 1
m_Z^{closest}	[80,100] GeV	[80,100] GeV
$n_{b\text{-jets}}$	0	≥ 2
n_{lep}	≥ 2	≥ 3
$n_{\mathrm{lep}}+n_{\mathrm{jets}}$	—	≥ 6
$E_{\mathrm{T}}^{\mathrm{miss,\,sig}}$	$> 15\ \sqrt{\mathrm{GeV}}$	—
$m_{\mathrm{T2}}(\ell_1, \ell_2)$	> 120 GeV	—

5.6.5. Common Control Regions

Two CRs are used to normalise the VV (CR VV) and the $t\bar{t}+V$ (CR $t\bar{t}+Z$) processes. Both CRs build on the dedicated leptonic selection described above. The selection criteria are summarised in Table 5.12.

Diboson Control Region

As described in Section 5.5.3, there are non-negligible contributions of the VV process to the SRs. This motivates a dedicated CR to normalise the contribution of the VV process. Most VV events in the SRs have either two or three charged leptons, therefore the CR was designed to be enriched in these final states.

Early studies on the VV process showed that finding a CR of decent purity in the lep-had or had-had channel is difficult to achieve. Especially the contributions from

events with fake τ_{had} contaminate the selections. Also the variables to select massive vector bosons, as invariant masses or m_{T}, are deteriorated by the additional neutrino(s) from the tau-lepton decays. Therefore, the requirements on τ_{had} are lifted. Light leptons of signal quality and τ_{had} are used democratically and referred to as leptons.

In order to reject contributions from SM processes involving top-quarks, events with b-jets are vetoed. Events need to have at least two leptons, in order to select the targeted final states.

The SRs mostly contain events with Z bosons, e.g. $ZZ \to \ell^+\ell^-\,\nu\bar{\nu}$ in case of two charged leptons and $ZW \to \ell^+\ell^-\,\ell\nu$ for three charged leptons. Therefore, the invariant mass of the same-flavour opposite-sign pair closest to m_Z (m_Z^{closest}) as defined in Section 5.4 is used. A window cut between 80 and 100 GeV is used, efficiently rejecting all events without Z bosons. This enriches the contribution of light leptons, since for one thing tau leptons also decay to mixed-flavour states, e.g. $Z \to e\nu_e\mu\nu_\mu$, but more importantly the invariant mass of τ_{had} pairs is smaller than m_Z, due to the escaping neutrinos, and has a much broader distribution worsening the discrimination power with respect to other background processes. Figure 5.16 (a) shows the distribution after applying all other CR cuts.

The Z boson selection in combination with the b-jet veto enriches the CR with events from the Z+jets process. The main difference between the targeted VV final states and the Z+jets process are the additional neutrinos. As discussed, the $Z \to \tau\tau$ contribution is small. Most of the Z+jets events contain prompt decays to light leptons and therefore no neutrinos which could give genuine $E_{\text{T}}^{\text{miss}}$, as opposed to events from VV, where most of the time at least one neutrino is involved. Figure 5.16 (c) shows the $E_{\text{T}}^{\text{miss}}$ distribution in the selection of the CR for the VV process without cuts on $E_{\text{T}}^{\text{miss}}$-related variables. The accumulation of Z+jets events at low $E_{\text{T}}^{\text{miss}}$ is clearly visible, but there is still a contribution of roughly 10 % at high values. As discussed in Section 5.4, $E_{\text{T}}^{\text{miss, sig}}$ can be used to suppress $E_{\text{T}}^{\text{miss}}$ from jet mismeasurements. Figure 5.16 (d) show $E_{\text{T}}^{\text{miss, sig}}$, where the contribution of Z+jets for high values is suppressed to virtually zero. The separation of the bulk of Z+jets and VV events is also better for $E_{\text{T}}^{\text{miss, sig}}$, motivating a cut at 15 $\sqrt{\text{GeV}}$.

Finally, a cut on $m_{\text{T2}}(\ell_1, \ell_2)$, where m_{T2} is calculated from the two leptons with highest p_{T}, is applied to suppress the remaining contribution from processes involving W bosons. Figure 5.16 (b) shows the $m_{\text{T2}}(\ell_1, \ell_2)$ distribution before applying a cut at 120 GeV, rejecting mostly contributions from the V+jets and $t\bar{t}$ processes.

The overall performance of the CR for VV is very good and summarised in Table 5.13. The purity of the targeted VV process is over 90 %. The final state with two charged leptons has a relative contribution of about 45 % and the final state with three charged leptons of about 55 % of the VV process in this CR.

$t\bar{t} + V$ Control Region

The last CR targets $t\bar{t} + Z$. As described in Section 5.5.3, the main contribution to the $t\bar{t} + V$ process are events where a Z boson decays to a pair of neutrinos. These events are intrinsically hard to separate, since they share the final state with the $t\bar{t}$ process, the only difference being the two additional neutrinos giving rise to more $E_{\text{T}}^{\text{miss}}$. The

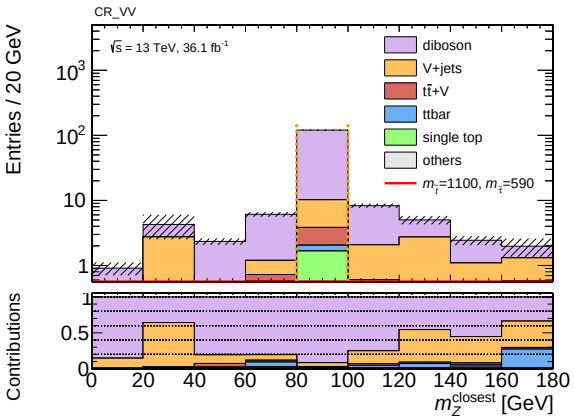

(a) m_Z^{closest} distribution.

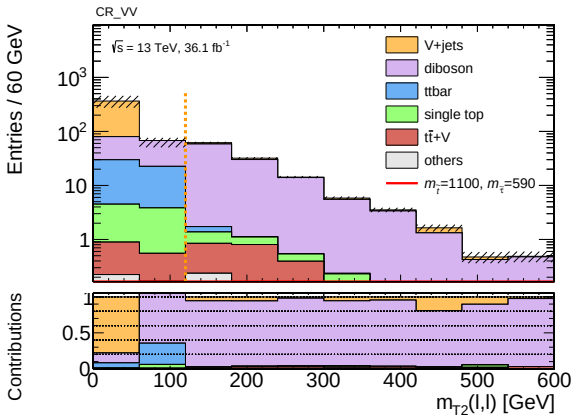

(b) $m_{\text{T2}}(\ell_1, \ell_2)$ distribution.

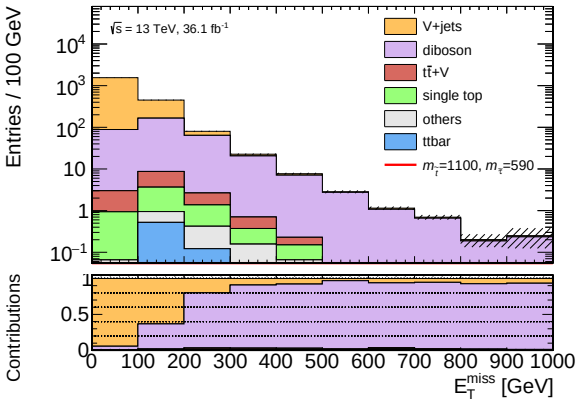

(c) $E_{\text{T}}^{\text{miss}}$ distribution (no cut on $E_{\text{T}}^{\text{miss, sig}}$ applied).

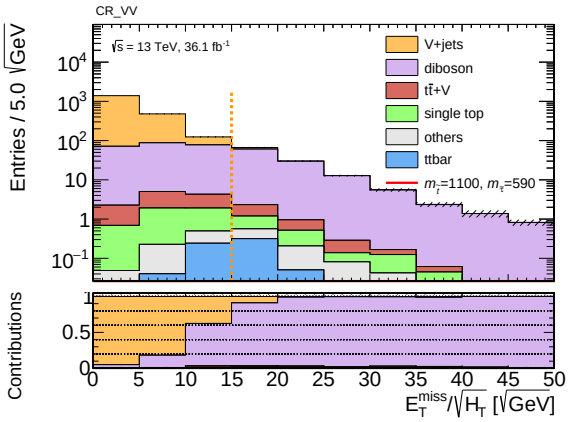

(d) $E_{\text{T}}^{\text{miss, sig}}$ distribution.

Figure 5.16.: N-1 plots for the CR for the VV process. All processes are scaled to the collected integrated luminosity of 36.1 fb^{-1}. The relative contribution of each SM process per bin is given in the bottom pad. The normalisations of the processes are taken directly from theory. The hatched band indicates the statistical uncertainty of the MC estimation.

Table 5.13.: Expected yields of the common CRs for the VV (left) and $t\bar{t}+V$ (right) process. All processes are scaled to the collected integrated luminosity of 36.1 fb^{-1}. The normalisations of the processes are taken directly from theory. Only the statistical uncertainties from the MC estimation are quoted here.

	CR_VV		CR_ttZ	
	exp. events	(contr.)	exp. events	(contr.)
$m_{\tilde{t}} = 1100, m_{\tilde{\tau}} = 590$	0.0 ± 0	0.0 %	0.0 ± 0	0.0 %
data	117 ± 11	97 %	148 ± 12	128 %
diboson	110.3 ± 2.2	91.5 %	11.91 ± 0.28	10.30 %
V+jets	6.4 ± 1.5	5.3 %	0.24 ± 0.27	0.20 %
others	0.569 ± 0.023	0.472 %	2.44 ± 0.19	2.11 %
single top	1.10 ± 0.11	0.91 %	16.1 ± 0.5	13.9 %
$t\bar{t}+V$	1.80 ± 0.10	1.49 %	84.4 ± 0.7	73.0 %
ttbar	0.38 ± 0.25	0.31 %	0.56 ± 0.26	0.49 %
total background	120.5 ± 2.7		115.6 ± 1.0	

idea of the CR defined here is to exploit the charged leptonic decay channels of the Z boson to select events with a $t\bar{t}+Z$ signature and to normalise the $t\bar{t}+V$ process in this region. The main advantage is that the relative difference between $t\bar{t}+[Z\to\ell\ell]$ and $t\bar{t}+[Z\to\nu\nu]$ can be obtained directly from the well-known Z boson branching fractions, therefore there are no additional extrapolation uncertainties to be considered. The main disadvantage is that different types of particles are used in the determination of the normalisation. There is no direct cancellation of the uncertainties related to the reconstruction and identification of the Z boson decay products.

The $t\bar{t}+Z$ CR shares the leptonic baseline selection with the VV CR as described above. As in the CR for the VV process, a requirement on m_Z^{closest} to be in the window of 80–100 GeV is employed. Figure 5.17 (a) shows this distribution before applying the requirement.

The two top-quarks are targeted with a requirement of at least two b-jets. As Figure 5.17 (b) illustrates, requiring one b-jet rejects VV and V+jets, which is efficiently selected due to the m_Z^{closest} requirement, but due to the high overall contribution, even events with one fake b-jet can compete with the $t\bar{t}+Z$ process.

Another significant feature of the $t\bar{t}+[Z\to\ell\ell]$ process is the high number of final state objects. As shown in Figure 5.17 (c), requiring at least three leptons efficiently rejects contributions from remaining $t\bar{t}$ and V+jets events, which both have at most two leptons from the hard process.

A slight improvement of the purity can be made using a requirement on the total number of final-state objects (n_{obj}) defined as the sum of the numbers of e, μ, τ_{had}, and jets. While the hard process of $t\bar{t}+[Z\to\ell\ell]$ contains six objects, processes like VV and single top require additional initial- or final-state jets to fulfil this criterion (cf. Figure 5.17 (d)).

The performance of the CR for $t\bar{t}+Z$ is summarised in the right column of Table 5.13.

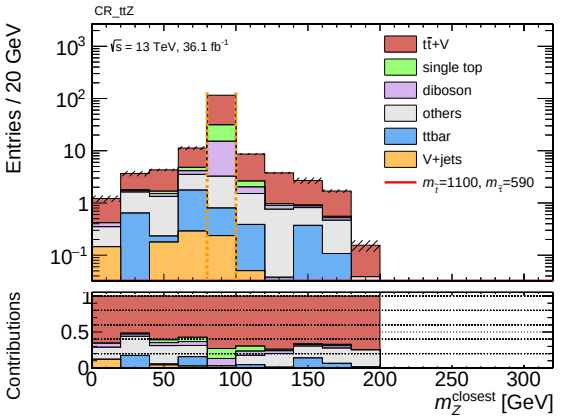

(a) m_Z^{closest} distribution.

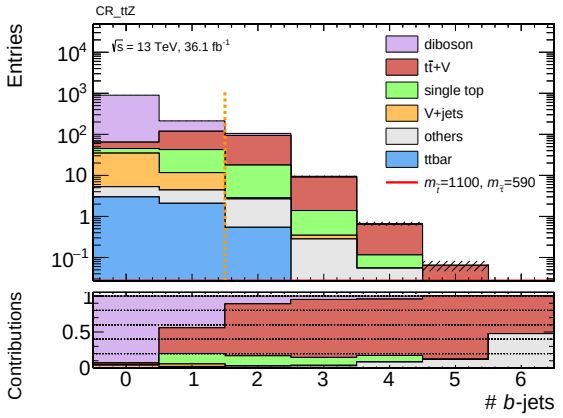

(b) $n_{b\text{-jets}}$ distribution.

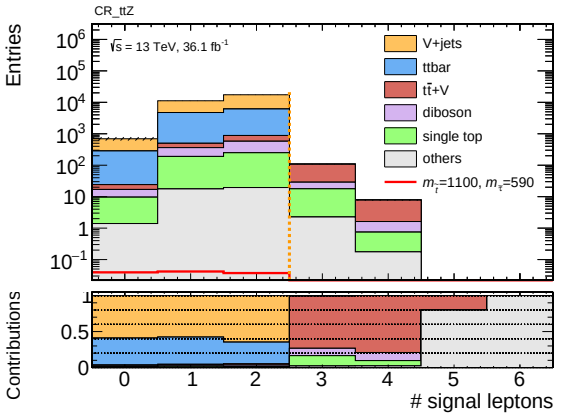

(c) n_{lep} distribution.

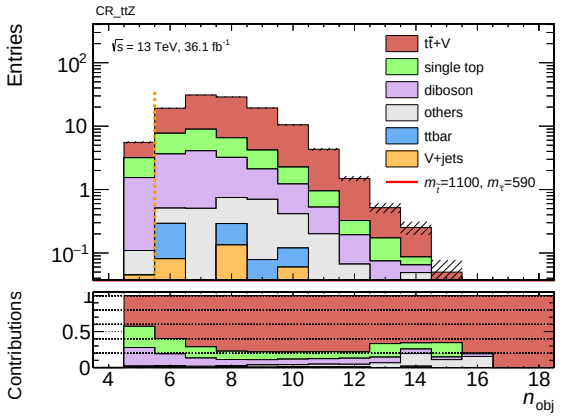

(d) n_{obj} distribution.

Figure 5.17.: N-1 plots for the CR for the $t\bar{t}+V$ process. All processes are scaled to the collected integrated luminosity of 36.1 fb^{-1}. The relative contribution of each SM process per bin is given in the bottom pad. The normalisations of the processes are taken directly from theory. The hatched band indicates the statistical uncertainty of the MC estimation.

The normalised process contributes about 73 % to the CR with an expectation from simulation of about 84 events. Main contaminations arise from the VV and single-top processes, where events from VV are normalised in a dedicated region. The $t\bar{t}+[Z \to \ell\ell]$ final states contribute more than 98 % to the $t\bar{t}+V$ yield listed in the table.

5.6.6. Fake-Factor Method

A significant contribution to the background processes in the SRs are SM processes where the τ_{had} is faked from jets. In the preliminary analysis of a partial dataset [2], the fake contribution for the lep-had channel was estimated directly from MC simulation.

Unfortunately, the nominal normalisation factor (NF) on the $t\bar{t}$ process with fake τ_{had}, determined in an opposite-sign selection, was found to be large (2.22). To cross-check this result, a second NF was determined by replacing the opposite-sign CR with a CR with a same-sign selection and keeping the remaining statistical setup the same. The second NF was determined to be much lower (1.33 ± 0.29). Since the NF from the same-sign selection was not used in the background estimation strategy, an additional uncertainty of 40 % was introduced on the NF from the opposite-sign CR to account for the differences of the NFs. The resulting NF was given as 2.22 ± 1.11 and had a large uncertainty. Studies of the had-had channel in the fake selection show much better agreement of the MC simulation with the observed data, allowing the direct normalisation of the fake contribution in the dedicated CR. Therefore, the dedicated fake estimation procedure is used only for the lep-had channel.

In order to estimate the contribution of events with fake τ_{had} in all regions of the lep-had selection, a so-called fake-factor method is employed in this analysis. Instead of using the normalised estimation from MC, the fake contributions are now determined on data. The basic idea of the FFM is to estimate the fake contribution not in a phase space different from the target selection, but by using events with similar kinematics. To get an independent sample of events with the same kinematics, events with tau-like jets failing one of the τ_{had} identification criteria are studied. The probability of a τ_{had}-like jet to pass or fail the chosen τ_{had}-identification WP is assumed to be independent of the kinematics of the event, but a dependence on certain jet properties is accounted for. These assumptions allow to measure the corresponding fake probabilities in a statistically independent region and to apply them in the regions of interest.

The ingredients for the FFM are discussed in the following. The selection of the tau-like jets and the measurement of the fake efficiencies are discussed. At the end of the section, the fake estimation itself is described.

Anti-ID Tau Selection

The FFM explicitly defines a sample of tau-like jets (called $\tau_{\text{had}}^{\text{Anti-ID}}$ in the following). Only the requirements on the τ_{had} candidate are changed, while the remaining selection criteria remain untouched. $\tau_{\text{had}}^{\text{Anti-ID}}$ are defined by loosening the BDT requirement of $\tau_{\text{had-vis}}$ candidates (cf. Section 5.3) down to 0.2 and explicitly vetoing $\tau_{\text{had-vis}}$ of medium quality ($\tau_{\text{had}}^{\text{ID}}$ in the following). This ensures that the $\tau_{\text{had}}^{\text{Anti-ID}}$ candidates fulfil the same geometrical requirements, as well as the requirement on the charge (one or three charged tracks) as the $\tau_{\text{had}}^{\text{ID}}$.

The anti-ID sample is constructed from events which do not contain $\tau_{\text{had}}^{\text{ID}}$, but at least one $\tau_{\text{had}}^{\text{Anti-ID}}$. In case of multiple $\tau_{\text{had}}^{\text{Anti-ID}}$ candidates, the candidate with the largest p_{T} is selected as $\tau_{\text{had}}^{\text{Anti-ID}}$ candidate. This increases the contribution of events with $p_{\text{T}}(\tau_{\text{had}}^{\text{Anti-ID}}) > 70$ GeV, which are events of interest for the lep-had selection.

The anti-ID sample uses a special overlap removal procedure. It performs the baseline OR procedure (as described in Section 5.3) but treats the $\tau_{\text{had}}^{\text{Anti-ID}}$ like an $\tau_{\text{had}}^{\text{ID}}$ instead of as a jet. All variables used for the kinematic selections are then recalculated using the $\tau_{\text{had}}^{\text{Anti-ID}}$, where the $\tau_{\text{had}}^{\text{ID}}$ would usually enter.

Measurement

A dedicated, statistically independent, region is used to measure the rate of fake $\tau_{\text{had}}^{\text{ID}}$ in dependence of the corresponding $\tau_{\text{had}}^{\text{Anti-ID}}$ sample. The measurement region uses a same-sign selection in order to increase the contribution of fake τ_{had}. In combination with an upper cut on $m_{\text{T2}}(\ell, \tau)$ of 60 GeV, the same-sign requirement provides a selection mutually disjoint to the SR and all other control and validation regions, which are discussed above. As the lep-had selection prescribes, at least one b-jet and $p_{\text{T}}(\tau_{\text{had-vis}}) > 70$ GeV are required. In order to obtain a more SR-like selection and to reject potential remaining multi-jet contributions, a cut on $E_{\text{T}}^{\text{miss}} > 100$ GeV is introduced. The requirements are listed in Table 5.14. Figure 5.18 shows the distribution of $p_{\text{T}}(\tau)$ in the measurement region, where the individual contributions of $\tau_{\text{had}}^{\text{ID}}$ as well as $\tau_{\text{had}}^{\text{Anti-ID}}$ are split up by their origin from real τ_{had} or other sources (fake). Figure 5.10 shows the measurement region in the lower left in the context of the lep-had selection.

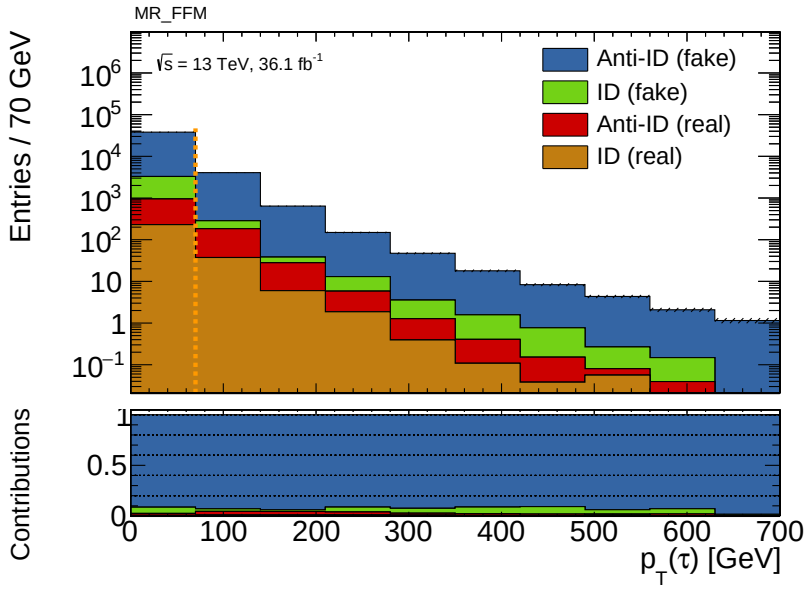

Figure 5.18.: $p_{\text{T}}(\tau_{\text{had-vis}})$ distribution in the measurement region. Events are split up according to their origin (real/fake) and their quality (ID/Anti-ID). The relative contribution of each category per bin is given in bottom pad. The nominal expectation from MC simulation is shown.

Table 5.14.: Selection criteria of the lep-had FFM measurement region applied on top of the lep-had selection.

same sign between ℓ, τ_{had}
$E_{\text{T}}^{\text{miss}} > 100$ GeV
$m_{\text{T2}}(\ell, \tau) < 60$ GeV

The measurement region is used to determine the transfer rate from events with $\tau_{\text{had}}^{\text{Anti-ID}}$ to events with an $\tau_{\text{had}}^{\text{ID}}$. The transfer rate is called fake-factor and measured in dependence of p_{T} and the prongness of the τ_{had} candidate.

While the measurement region is chosen to have a very low contribution of SM processes containing real τ_{had}, the application regions (AR) can exhibit a significant amount of events with real τ_{had}. The discrimination between real and fake τ_{had} is only possible on simulated samples. Therefore, the number of events with real $\tau_{\text{had}}^{\text{ID}}$ ($N_{\text{real}}^{\text{ID}}$(MC, AR)) and the number of events with real $\tau_{\text{had}}^{\text{Anti-ID}}$ ($N_{\text{real}}^{\text{Anti-ID}}$(MC, AR)) is evaluated on the simulated samples. These contributions are then subtracted from the observation in the $\tau_{\text{had}}^{\text{ID}}$ and $\tau_{\text{had}}^{\text{Anti-ID}}$ samples yielding the respective expected fake contributions. Given the observations of the number of events in the measurement region with $\tau_{\text{had}}^{\text{ID}}$ (N^{ID}(data, MR)) and $\tau_{\text{had}}^{\text{Anti-ID}}$ ($N^{\text{Anti-ID}}$(data, MR)), respectively, the fake factor (FF) can then be calculated for each p_{T} bin and for the cases of 1- or 3-prong as

$$FF = \frac{N^{\text{ID}}(\text{data, MR}) - N_{\text{real}}^{\text{ID}}(\text{MC, MR})}{N^{\text{Anti-ID}}(\text{data, MR}) - N_{\text{real}}^{\text{Anti-ID}}(\text{MC, MR})}. \tag{5.8}$$

The resulting fake factors are shown in Figure 5.19. In the measurement region the contamination of events with real τ_{had} is about 1 % (10 %) for $\tau_{\text{had}}^{\text{Anti-ID}}$ ($\tau_{\text{had}}^{\text{ID}}$).

Fake-Factor Estimate

Given the measurement of the fake factors, the fake estimate for a given region AR and a bin in $p_{\text{T}}(\tau)$ and 1- or 3-prong is obtained as

$$N_{\text{fakes}}(\text{AR}) = \left[N^{\text{Anti-ID}}(\text{data, AR}) - N_{\text{real}}^{\text{Anti-ID}}(\text{data, AR})\right] \times FF. \tag{5.9}$$

The total fake estimate is given by the sum over all bins in $p_{\text{T}}(\tau)$ and 1- and 3-prong. Since this FFM is inclusively estimating all fake contributions to an AR by construction, the fake contribution predicted by simulation has to be subtracted for all SM processes. In the following, in all plots and tables showing the estimate from the FFM, the contributions from the SM processes will have the subtraction applied and only contain the events with real τ_{had}.

5.7. Systematic Uncertainties

Given the complex experimental setup, several sources of systematic uncertainties are considered in this analysis. In the following, they are divided into uncertainties on the

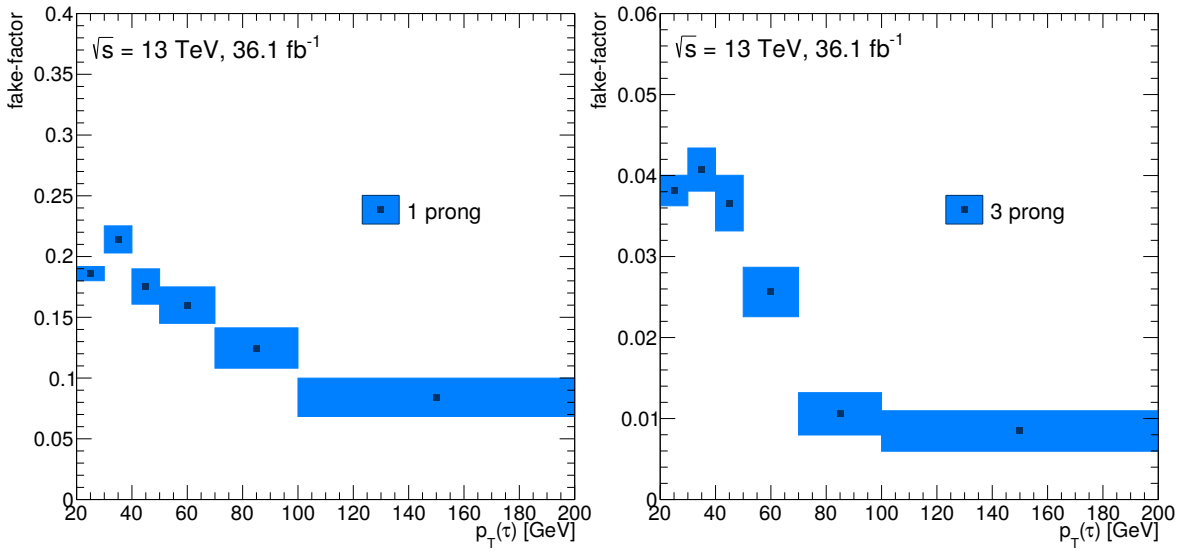

Figure 5.19.: Fake factors in the measurement region. The dependence of $p_{\mathrm{T}}(\tau_{\text{had-vis}})$ is shown, but only the last two bin are actually used in the analysis due to the requirement of $p_{\mathrm{T}}(\tau_{\text{had-vis}}) > 70$ GeV in the lep-had selection. The last bin of $p_{\mathrm{T}}(\tau_{\text{had-vis}})$ is inclusive with respect to all events above 200 GeV.

detector response and uncertainties from the theoretical prediction of the MC simulation. Additional uncertainties for the FFM are considered as well. The uncertainties from the limited MC statistics are treated within the statistical evaluation described in Section 5.8.

All systematic uncertainties described here are implemented as variations of the nominal prediction. The treatment of the variations will be described in Section 5.8 as well. Table 5.15 gives an overview of the relative systematic uncertainties as obtained by the final statistical evaluation.

5.7.1. Detector-Response Uncertainties

The uncertainties on the detector response are provided by the combined performance groups of the ATLAS collaboration. They are applied to all simulated samples, including the signal samples.

Electrons

For samples containing electrons, variations of the energy scale and resolution are applied [100]. Reduced sets of variations are provided for the reconstruction efficiency of electrons, as well as for their identification and isolation efficiencies [98].

Muons

Samples containing muons consider variations of the scale factors for the reconstruction and isolation efficiencies. Furthermore systematic variations are derived from smearing the tracks in the ID and the MS and varying the momentum scale of the muons [101].

Table 5.15.: Overview over the relative systematic uncertainties [3]. The top row shows the total systematic uncertainties for the two channels, while below a break-down into categories is given. The experimental uncertainties with small contributions are collected into "Other experimental".

	SR LH	SR HH
Total systematic uncertainty	± 29 %	± 53 %
Fake-factor method	± 23 %	—
Jet-related	± 9.3 %	± 36 %
Tau-related	± 7.2 %	± 32 %
Other experimental	± 6.1 %	± 12 %
Theory modelling	± 8.3 %	± 20 %
MC statistics	± 7.5 %	± 17 %
Normalization factors	± 4.8 %	± 14 %
Luminosity	± 0.3 %	± 0.8 %

Dedicated uncertainties on the efficiency scale factor for variations of the TTVA cuts described in Section 5.3 are included.

Taus

For the $\tau_{\text{had-vis}}$, systematic variations for reconstruction and identification efficiencies, as well as the energy scale and the electron rejection efficiency are used. Simulated samples with variations of the settings impacting $\tau_{\text{had-vis}}$ were used [68]. These include variations of the underlying event tune, the hadronic showering model in GEANT4, the prediction of the ATLAS geometry and its material budget, and the noise thresholds in the calorimeter clustering. Since the signal samples use the fast detector simulation, additional systematic uncertainties are used.

Jets

Uncertainties on the jet energy scale and resolution are used. They are derived with alternative samples varying the detector response, changes to the topo-clustering, and the event generator [66].

Uncertainties on the pile-up subtraction as described in Section 4.6 are considered as well. They account for the fit uncertainties of the parameters α and β used in the N_{PV} and $\langle\mu\rangle$ terms, and residual effects of the uncertainty of the p_{T} and ρ determination.

For light jets, two additional sources of uncertainty are taken into account, the variation of the composition of light-quark- with respect to gluon-initiated jets and the variation of the gluon energy scale.

Uncertainties for the inter-calibration in η are derived from simulation [118]. The efficiency scale factors for the JVT requirement introduce another uncertainty [103].

For the global sequential correction scheme, the potential mismodelling of jet deposits in the MS is considered [67].

B-Jets

Uncertainties on the b-tagging-efficiency scale factors are taken into account, as well as the rejection of charm and light jets [119, 120]. In the determination of the c-jet efficiency, the extrapolation uncertainty from the D^{*+} measurement to the inclusive c-jet processes is considered separately.

Missing Transverse Energy

The effect of the uncertainties on the calibrated objects to $E_{\mathrm{T}}^{\mathrm{miss}}$ is incorporated by a recalculation of $E_{\mathrm{T}}^{\mathrm{miss}}$ for every systematic variation. Additional uncertainties for the resolution and the energy scale of the soft-term contributions are employed [109].

Pile-Up Reweighting

A variation of the scale factor applied in the pile-up reweighting, as described in Section 5.2, is used for the estimation of the uncertainty of this method.

Luminosity

The luminosity-measurement uncertainty for the data-taking periods 2015 and 2016 is 3.2 %. Main sources of uncertainty are the calibration in vdM runs and the modelling of the transfer of the calibration to high-μ conditions. The drift of the calibration of the instrumentation used for the luminosity determination is considered, but does not have a significant impact on the total systematic uncertainty.

Trigger Scale-Factor Uncertainties

The trigger efficiency measurements by the CP groups provide scale factors with associated uncertainties [114]. These are included for the light-lepton and τ_{had} triggers. For the $E_{\mathrm{T}}^{\mathrm{miss}}$ trigger no dedicated uncertainties are used.

5.7.2. Uncertainties on the Fake-Factor Estimate

Several sources of systematic uncertainties are considered for the FFM and implemented as uncorrelated systematic variations. Statistical uncertainties from the measurement of the fake factors as well as the limited statistics of the application regions are taken into account. Variations of the subtraction of events with real τ_{had} are performed and the resulting effect on the fake factors is of the order of 10 %.

Since the measurement region is in a very loose kinematic regime and extends to low values of $E_{\mathrm{T}}^{\mathrm{miss}}$, a potential contamination with multi-jet events is studied through variations of the $E_{\mathrm{T}}^{\mathrm{miss}}$ cut. The influence on the fake factors is low and mostly compatible within statistical uncertainties. Therefore, a conservative uncertainty of 10 % is applied.

The influence of the $\tau_{\text{had}}^{\text{Anti-ID}}$ definition is investigated using a variation of the BDT requirement. The resulting uncertainty is estimated with 10 %.

The measurement region for the fake factors is located at low $m_{\text{T2}}(\ell, \tau)$ values. An extrapolation uncertainty is derived on the simulated sample of the $t\bar{t}$ process. The fake factors are calculated for the nominal case $m_{\text{T2}}(\ell, \tau) < 60$ GeV and the inverted cut $m_{\text{T2}}(\ell, \tau) > 60$ GeV as well as for variations of this threshold. The discrepancy of low- and high-$m_{\text{T2}}(\ell, \tau)$ gives rise to a 20 % uncertainty.

5.7.3. Theory Uncertainties

For the simulated samples, uncertainties on the theory and hadronisation modelling are included. Each generator uses an individual implementation of the matrix element calculation and the approximations and cut-offs of calculations therein. Most generator setups also provide the possibility to vary internal parameters sensitive to the additional radiation produced. Therefore, the uncertainties are estimated by comparing simulated samples with the different variations in the generator setups.

For the $t\bar{t}$ and single-top processes, several sources of uncertainties were considered. The modelling of the hard-scattering event is varied by comparing two samples, where the nominal matrix element generator Powheg-Box is compared to MadGraph5_aMC@NLO. The fragmentation and hadronisation uncertainties are evaluated by comparing the nominal showering program Pythia to the alternative program Herwig++, while keeping the matrix element generator the same. Finally, dedicated samples using the rad_{Hi}, rad_{Lo} variation of the Perugia 2012 tune of the parton shower [85, 87] are taken into account. These variations increase and decrease the additional initial- and final-state radiation respectively.

The $t\bar{t}$ and single-top processes are simulated separately, which does not take into account potential interferences at NLO. As discussed in Section 3.2, for the MC@NLO method there are two schemes available to handle the interference. As an estimate of the uncertainty on the interference handling, the variation between the nominal diagram-removal and the alternative diagram-subtraction scheme is evaluated [46, 47]. Since the single-top process is not normalised in a control region, a conservative uncertainty of 5 % is applied on the cross section.

For the $t\bar{t} + V$ process, the uncertainty on the matrix-element generation and the shower development is estimated by comparing the nominal Sherpa samples with sample generated with MadGraph5_aMC@NLO interfaced with Pythia. Furthermore, variations of the generator settings for the factorisation and renormalisation scale are taken into account.

In the VV process, the generator settings for the factorisation and renormalisation scales are varied. An uncertainty for the matrix-element generation and the hadronisation shower is estimated from a comparison of the nominal Sherpa to alternative Powheg samples.

For the V+jets processes, the nominal Sherpa samples are compared with alternative MadGraph samples interfaced with Pythia. Also here, generator-setting variations for the renormalisation and factorisation scales are taken into account. Since the V+jets processes are not normalised in data, a conservative uncertainty of 5 % is applied on the cross section.

5.8. Statistical Evaluation

In order to get an objective assessment of the data observed, a statistical procedure following current conventions in particle physics is adopted. The technical implementation uses the *HistFitter* package [121], which in turn is relying on functionality provided by the *HistFactory* package [122].

In the following, an overview over the most important procedures used in this analysis is given. The mathematical formulation closely follows [123].

5.8.1. Likelihood

The Poisson probability to observe k events, given the expectation of n_{exp} is

$$\mathcal{P}(k) = \frac{n_{\text{exp}}^k}{k!}\, \mathrm{e}^{-n_{\text{exp}}}. \tag{5.10}$$

The expectation can be parameterised by introducing the signal strength μ, such that n_{exp} reads:

$$n_{\text{exp}} = \mu\, s + b, \tag{5.11}$$

where s is the number of expected signal events and b the number of expected events from all SM background processes. This opens the possibility to fit μ as a free parameter. Setting $\mu = 0$ yields a SM-like description, while $\mu = 1$ describes the signal-plus-background expectation at the predicted cross section. Also limits of different strength can be set on the cross sections by using arbitrary values of μ.

The expected event yields s and b themselves can depend on a set of nuisance parameters $\boldsymbol{\theta}$ and may be constructed from several separate bins. The nuisance parameters can be uncertainties to be determined externally, as most of the systematic uncertainties of detector effects are. Nuisance parameters can also be normalisation factors on the background processes, to be constrained in control regions. In principle, one formulates a likelihood like this

$$L_{pois}(\mu, \boldsymbol{\theta}) = \prod_{j=1}^{N} \frac{(\mu\, s_j + b_j)^{n_j}}{n_j!}\, \mathrm{e}^{-(\mu\, s_j + b_j)}, \tag{5.12}$$

where the indices j are used for numbering the (in total N) bins, and therefore s_j (b_j) corresponds to the expected number of signal (background) events in bin j, and n_j is the observed number of events in bin j for data.

Equation (5.12) can be extended with M additional constraint terms with an expected number of events u_k and an observation of m_k:

$$L(\mu, \boldsymbol{\theta}) = L_{pois}(\mu, \boldsymbol{\theta}) \prod_{k=1}^{M} \frac{u_k^{m_k}}{m_k!}\, \mathrm{e}^{-u_k} \tag{5.13}$$

Additionally, terms for luminosity and MC statistics are introduced, which is described in detail in the paper describing the technical implementation of *HistFactory* [122].

A single likelihood is built for the full set of control and signal regions as described in Sections 5.6.3, 5.6.4, and 5.5.3. Using this likelihood, the combined statistical power of both signal regions is used and a common signal-strength parameter can be fitted in both channels simultaneously.

5.8.2. Test Statistics

Test statistics are a tool to evaluate hypotheses. The test statistics used in this analysis are defined such that they have low values in case of high agreement with the hypothesis and high values in case of large disagreement with the hypothesis tested. The distribution of each of the defined test statistics will be evaluated assuming the null hypothesis H_{null} and alternative hypothesis H_{alt}, either by sampling it with pseudo-data generated for the respective hypothesis or by using the asymptotic formulae described in [123].

In the following, the profile likelihood ratio and the test statistics for exclusion and discovery will be introduced.

Profile Likelihood Ratio

The profile likelihood ratio is defined as:

$$\lambda(\mu) = \frac{L\left(\mu, \hat{\hat{\boldsymbol{\theta}}}\right)}{L\left(\hat{\mu}, \hat{\boldsymbol{\theta}}\right)} \tag{5.14}$$

It is a function of the signal strength μ. The denominator contains the value of the maximised likelihood, where no additional constraints are put to μ or $\boldsymbol{\theta}$, $\hat{\mu}$ and $\hat{\boldsymbol{\theta}}$ are the corresponding values at which the likelihood takes the global maximum value. In the numerator the likelihood is maximised for the given value of μ, $\hat{\hat{\boldsymbol{\theta}}}$ is the set of parameters maximising the likelihood for this fixed value of μ.

Since the denominator contains the unconditionally maximised value of the likelihood, λ will always be in the range $0 \leq \lambda \leq 1$. In order to get the desired properties of the test statistic, test statistics will be formulated in terms of $-2\ln(\lambda)$, ensuring that high values of the test statistic will correspond to increasing disagreement with the hypothesis to be tested. It should be noted that $\hat{\mu}$ can a priori also take negative values which, given our expectation of positive signal contributions to the background, will be reflected in the construction of the test statistics.

Test Statistic For Discovery

The goal of the analysis is the observation of a new signal, therefore H_{null} to be excluded is the SM-only expectation and H_{alt} will be signal-plus-background expectation. The test statistic is therefore defined in terms of the profile likelihood at $\mu = 0$:

$$q_0 = \begin{cases} -2\ln\lambda(0), & \hat{\mu} \geq 0 \\ 0, & \hat{\mu} < 0 \end{cases} \tag{5.15}$$

In principle $\hat{\mu}$ can be smaller than zero if the data fluctuates below the background expectation. In order to not to disfavour H_{null} in the case of an underfluctuation, the test statistic is set to 0 in these cases.

Test Statistic For Upper Limits

In case that no significant excess of the SM expectation is observed, limits on the signal strength (or correspondingly the signal cross section) are set. For upper limits, the test statistic is formulated in the opposite way as for the discovery case. The signal-plus-background expectation represents now H_{null}, while the SM-only expectation is H_{alt}. The likelihood ratio now depends on the μ of interest, making a certain expectation of μ[7] the null hypothesis:

$$\tilde{q}_\mu = \begin{cases} -2\ln \frac{L\left(\mu, \hat{\hat{\boldsymbol{\theta}}}(\mu)\right)}{L\left(0, \hat{\hat{\boldsymbol{\theta}}}(0)\right)}, & \hat{\mu} < 0 \\ -2\ln \frac{L\left(\mu, \hat{\hat{\boldsymbol{\theta}}}(\mu)\right)}{L\left(\hat{\mu}, \hat{\boldsymbol{\theta}}\right)}, & 0 < \hat{\mu} < \mu \\ 0, & \hat{\mu} > \mu \end{cases} \tag{5.16}$$

Here, values of $\hat{\mu} > \mu$ are set to zero to not disfavour H_{null} in case of an overfluctuation of the signal-plus-background estimation. If the best-fit signal strength parameter $\hat{\mu}$ is smaller than zero, the denominator of the profile likelihood ratio is set to the value of the likelihood maximised at the SM expectation.

5.8.3. *P*-Values

Given the discovery test statistic, the probability to encounter a fluctuation at least as extreme as the observation given the null hypothesis of the SM expectation is called p-value (p_0)

$$p_0 = \int_{q_{0,\text{obs}}}^{\infty} f(q_0|0)\mathrm{d}q_0, \tag{5.17}$$

where $f(q_0|0)$ is the distribution of the test statistic q_0, assuming a SM hypothesis of $\mu = 0$. In the frequentist interpretation, the p-value corresponds to the fraction of experiments which are expected to observe a fluctuation at least as extreme as $q_{0,\text{obs}}$ if H_{null} is true.

p-values are also expressed in terms of Gaussian standard deviations: the so-called significance Z is then given as

$$Z = \Phi^{-1}(1-p), \tag{5.18}$$

where Φ^{-1} is the inverse of the cumulative Gaussian distribution. E.g. $Z = 5\sigma$ corresponds to a p-value of 2.87×10^{-7}, which is the threshold, commonly agreed on in high-energy particle physics, to claim the discovery of a new signal.

5.8.4. CLs

In case of the absence of an excess of observed events, upper limits on the signal strength can be set. The incompatibility of the observation with the null hypothesis (signal-plus-

[7] As discussed above the nominal signal expectation can be tested with $\mu = 1$. But also variations of μ can be tested, e.g. the signal expectation of the up- or down-variation of the expected signal cross section by one standard deviation.

background expectation) can be expressed as the p-value p_{s+b}, calculated with Equation (5.17), but with the test statistic $\tilde{q}_\mu$ instead of q_0 and the distribution for the hypothesis $\mu = 1$.

In case of small signal expectations with respect to the background expectation, it might happen that strong downwards-fluctuations would suggest that a signal model should be excluded even though there is no sensitivity. In order to not exclude signals incompatible with H_{s+b}, which at the same time are incompatible with H_b, $\mathrm{CL_s}$ (first introduced in [124]) is used

$$\mathrm{CL_s} = \frac{p_{s+b}}{p_b}, \tag{5.19}$$

suppressing p_{s+b} with p_b.

5.8.5. Systematic Uncertainties

Systematic uncertainties are put into the likelihood as nuisance parameters and parametrised in terms of Gaussian normal distributions with a width corresponding to the standard deviation of the systematic uncertainty. The uncertainties from the limited statistics of the CRs and the extrapolation between CR and SR are obtained from the simultaneous fit. Details on the implementation are given in [121, 122].

5.8.6. Fit Setup

The total likelihood is built for the regions described in the previous sections. As described, the background processes of interest are normalised by introducing a normalisation factor into the fit setup, which can float freely. In total four NFs are introduced for this analysis: the $t\bar{t}$ process has two NFs, one for events with only real τ_{had}, with CRs in the lep-had as well as the had-had channel, and the other one for events with at least one fake τ_{had}, with only a CR in the had-had channel, since the lep-had channel has a separate fake estimation. The other two NFs are applied to $t\bar{t}+V$ and VV events with their respective CRs.

In general, the normalisation factors are fitted in all regions (except for the VRs) in a combined simultaneous fit and the constraining power comes from the different relative contributions of the backgrounds. An exception is done for the combined CRs: in the light-leptonic selection of the common CRs the notion of "fake" τ_{had} is not well-defined any more. Since the contribution of the $t\bar{t}$ process is in any case small, the nominal prediction of the $t\bar{t}$ process is used in these two CRs.

The contribution of the signal process to all control and validation regions has to be assessed. The corresponding plots are shown in Section A.1. The signal contamination should be as low as possible, to not artificially increase the normalisation factors, which then would absorb some of the signal. High signal contamination in the VRs on the one hand leads to unwanted unblinding and on the other hand will decrease the validation power of the region in case of an excess, since it can be attributed to either signal or mismodelling. For the regions presented here, the signal contamination for the mass points not yet excluded is at an acceptable level, if the preliminary exclusion limits from the ICHEP 2016 conference are taken into account [2].

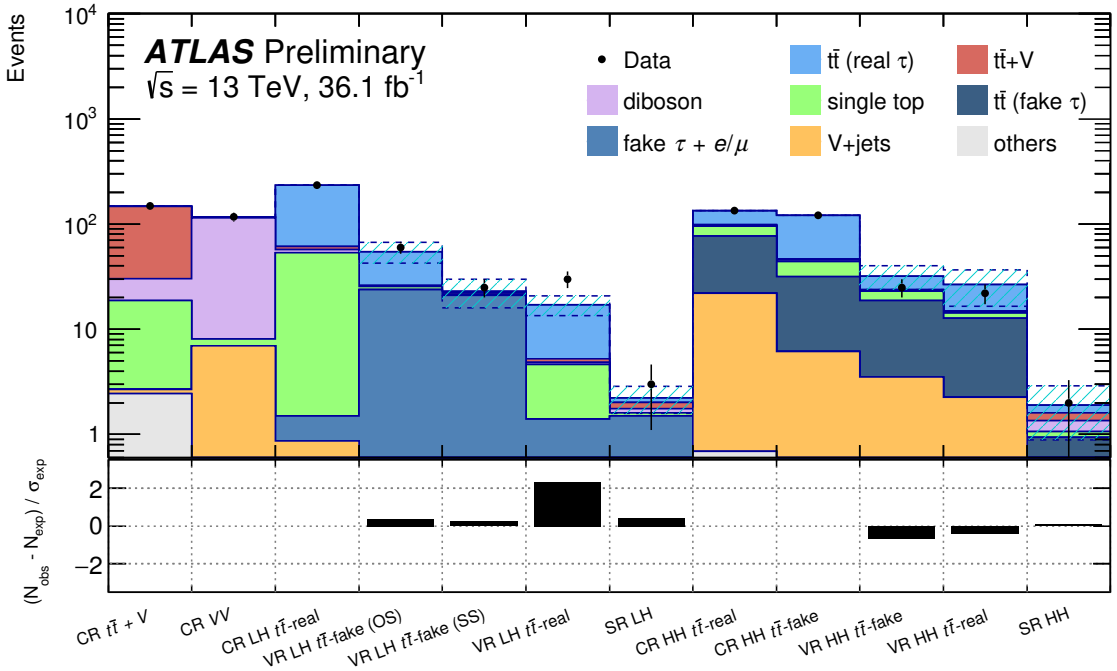

Figure 5.20.: Overview over all regions considered in this analysis [3]. The final background estimate is included and the observations are shown. The bottom pad shows the relative deviation of observation and expectation in units of standard deviations on the SM expectation including the full set of uncertainties.

5.9. Results

After finalising the full setup of the background estimation and validation- and signal-region definition, the regions can be unblinded. First, the results of the background estimations will be summarised and the validation regions discussed. Finally, the observations in the SRs will be interpreted in the context of model-dependent and -independent limits.

5.9.1. Observation

As described in the previous sections, the regions have been unblinded one by one. The results of the final background estimation are summarised in Table 5.16. Due to the NFs being free parameters in the combined fit, the observations in the CRs match the predictions in the background estimation. The validation regions mostly agree with the observation within the uncertainties. The plot in Figure 5.20 visualises the estimation of the individual background processes as well as the observations.

The resulting distributions of various important variables from the fully fitted background estimation can be seen in Figure 5.21 (a) for the CR LH $t\bar{t}$-real and for the CR HH $t\bar{t}$-real in Figure 5.22 (a) and for CR HH $t\bar{t}$-fake in Figure 5.22 (b). The fitted con-

Table 5.16.: Observed numbers of events in the CRs and VRs with the final background estimate from the simultaneous fit.

	CR LH $t\bar{t}$-real	CR HH $t\bar{t}$-real	CR HH $t\bar{t}$-fake	
observation	235	121	134	
background estimation	235 ± 15	121 ± 9	134 ± 11	
	VR LH $t\bar{t}$-real	VR HH $t\bar{t}$-real	VR HH $t\bar{t}$-fake	
observation	30	25	22	
background estimation	17 ± 4	32 ± 8	27 ± 10	
	VR LH $t\bar{t}$-fake (OS)	VR LH $t\bar{t}$-fake (SS)	CR $t\bar{t} + Z$	CR VV
observation	60	25	147	117
background estimation	55 ± 12	23 ± 7	148 ± 13	117 ± 14

Table 5.17.: Normalisation factors and their uncertainties as obtained from the simultaneous fit.

Process	Normalisation factor
VV	$1.0\ ^{+0.6}_{-0.3}$
$t\bar{t} + V$	$1.39^{+0.23}_{-0.23}$
$t\bar{t}$ with fake τ_{had}	$1.2\ ^{+0.4}_{-0.4}$
$t\bar{t}$ with real τ_{had}	$0.81^{+0.20}_{-0.19}$

tributions for the combined CRs are shown in Figure 5.23 (a) (VV) and Figure 5.23 (b) ($t\bar{t} + Z$). The final NFs with their respective uncertainties are listed in Table 5.17. The NFs are mostly compatible with one within their uncertainties, where the largest deviation is found for the $t\bar{t} + V$ background process.

The largest difference between expectation and observation is found in the VR for $t\bar{t}$ events with real τ_{had} in the lep-had selection. It amounts to more than 2 standard deviations (cf. Figure 5.20), but is not of concern for the analysis. Careful checks of the corresponding distributions of relevant variables did not reveal a systematic mismodelling. Figure 5.21 (b) shows the location of the excess in $E_{\text{T}}^{\text{miss}}$, but this excess is not found in the $E_{\text{T}}^{\text{miss}}$ distributions of other regions.

There is also the VR enriched in $t\bar{t}$ events with fake τ_{had} in the opposite-sign lep-had selection. Given that this VR was designed to target events with fake τ_{had}, it still has a large contribution of $t\bar{t}$ events with only real τ_{had}. If there were a systematic mismodelling of this process, this VR should also have a significant excess of observed events. Finally, the component of the $t\bar{t}$ process with real τ_{had} has only a minor contribution to the lep-had SR in comparison to the fake τ_{had} contributions. Therefore, the excess is considered to be a statistical fluctuation and does not prohibit the unblinding of the SRs.

The other VRs show very good agreement within the uncertainties and the correspond-

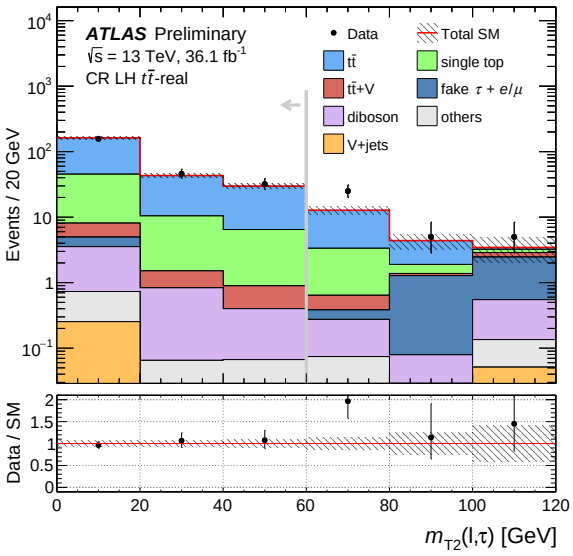

(a) $m_{\mathrm{T2}}(\ell,\tau)$ distribution in the lep-had CR.

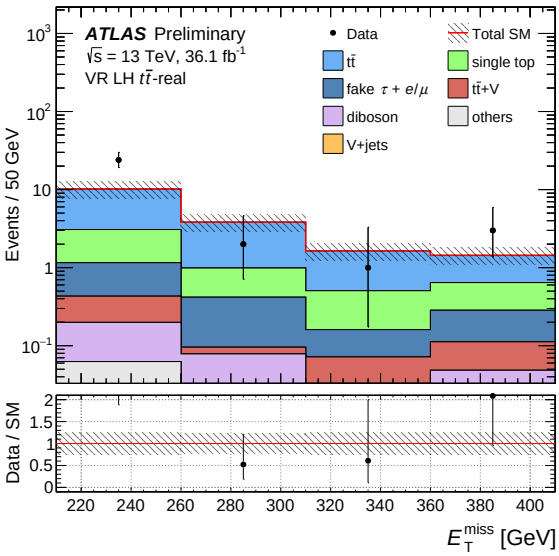

(b) $E_{\mathrm{T}}^{\mathrm{miss}}$ distribution in the lep-had VR.

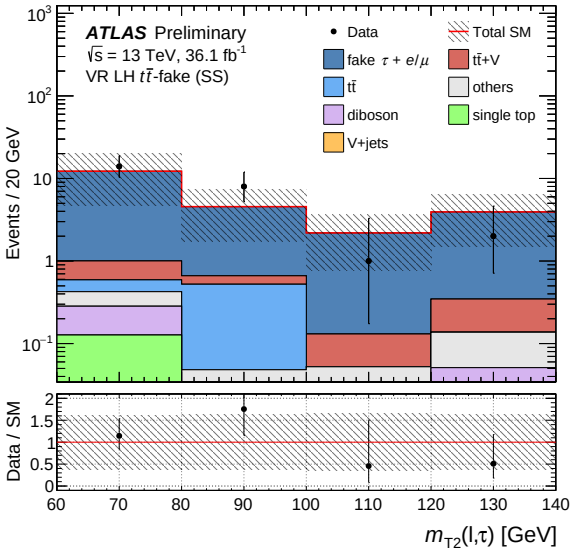

(c) $m_{\mathrm{T2}}(\ell,\tau)$ distribution in the lep-had VR (same-sign selection).

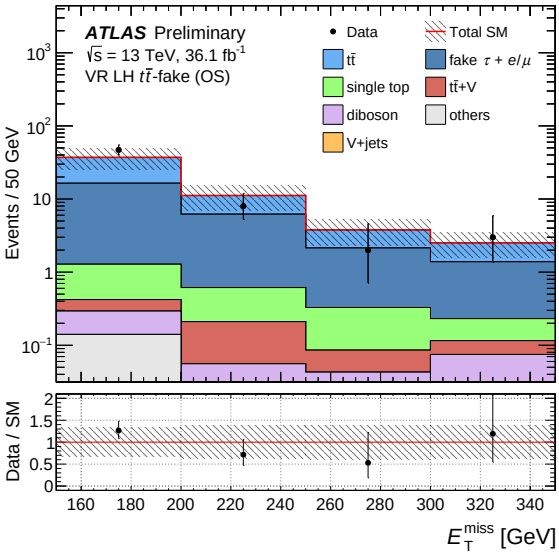

(d) $E_{\mathrm{T}}^{\mathrm{miss}}$ distribution in the lep-had VR (opposite-sign selection).

Figure 5.21.: N-1 plots for the lep-had CR and VRs (top row: events with real τ_{had}; bottom row: events with fake τ_{had}) [3]. All processes are scaled to the collected integrated luminosity of 36.1 fb^{-1}. The ratio of the observed data to the total SM expectation is given. The normalisations of the processes are taken from the final fit result. Fake contributions (fake $\tau + e/\mu$) are estimated using the FFM, only the real τ_{had} component of the other SM processes is included in the other background processes. The hatched band indicates the total statistical and systematic uncertainty on the SM-background estimation.

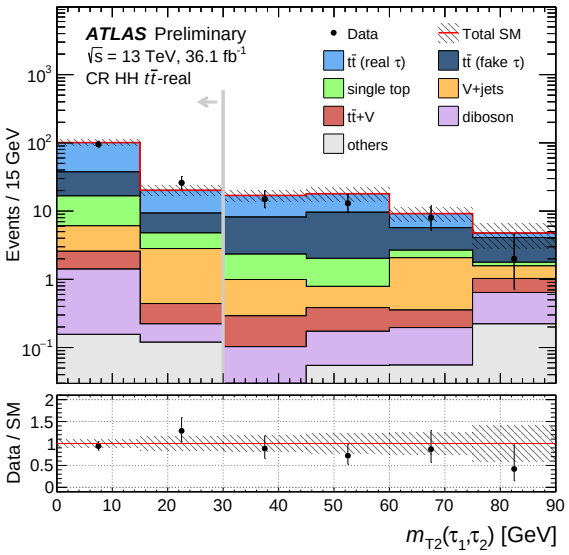

(a) $m_{\mathrm{T2}}(\ell,\tau)$ distribution in the had-had CR.

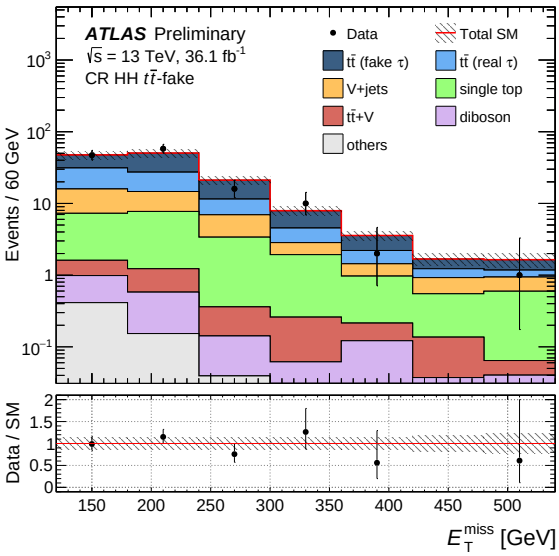

(b) $E_{\mathrm{T}}^{\mathrm{miss}}$ distribution in the had-had CR.

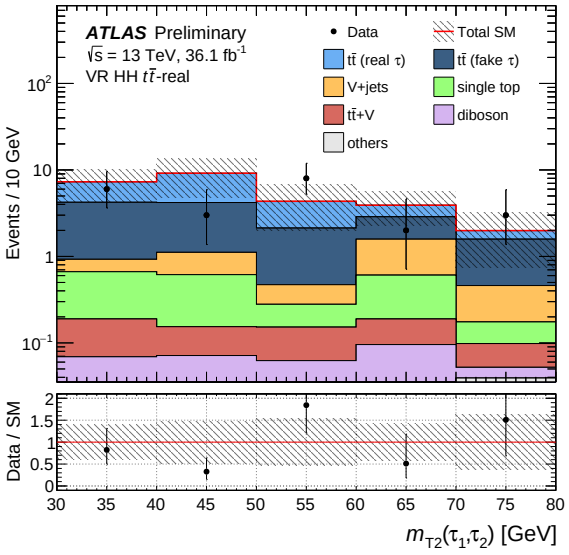

(c) $m_{\mathrm{T2}}(\tau_1,\tau_2)$ distribution in the had-had VR.

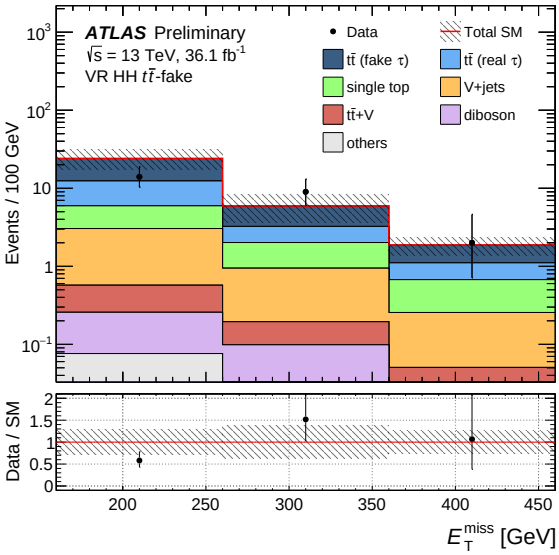

(d) $E_{\mathrm{T}}^{\mathrm{miss}}$ distribution in the had-had VR.

Figure 5.22.: N-1 plots for the had-had CRs and VRs [3]. Left column shows the regions for $t\bar{t}$ events with real τ_{had}, right column the regions for $t\bar{t}$ events with fake τ_{had}. All processes are scaled to the collected integrated luminosity of 36.1 fb^{-1}. The ratio of the observed data to the total SM expectation is given. The normalisations of the processes are taken from the final fit result. The $t\bar{t}$ process is split into events with real and fake τ_{had}. Both are separately normalized in dedicated CRs. The hatched band indicates the total statistical and systematic uncertainty on the SM-background estimation.

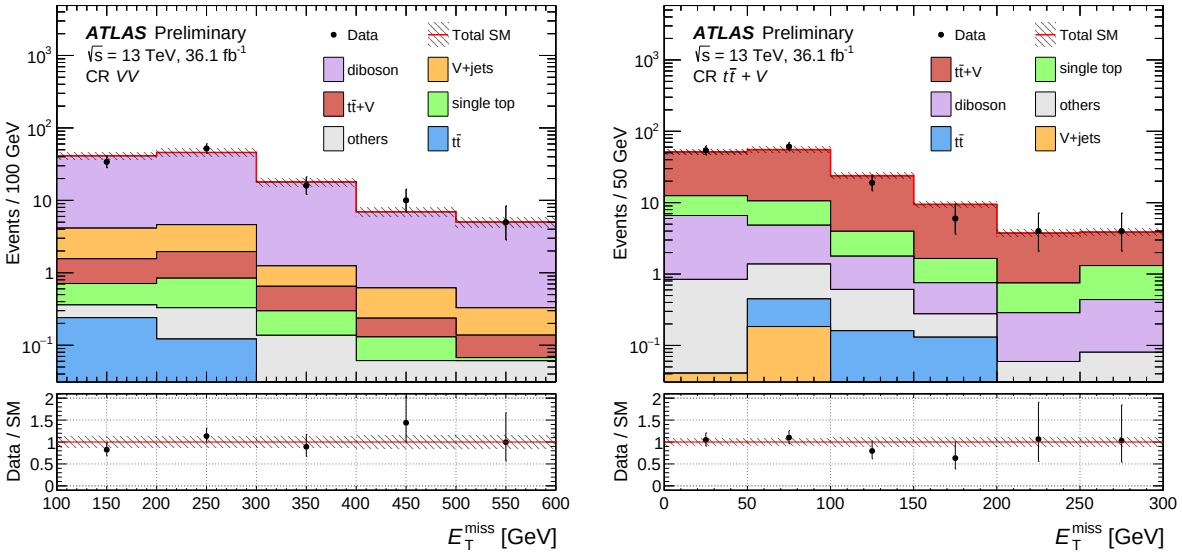

(a) $E_{\mathrm{T}}^{\mathrm{miss}}$ distribution in the CR for the VV process.

(b) $E_{\mathrm{T}}^{\mathrm{miss}}$ distribution in the CR for the $t\bar{t} + Z$ process.

Figure 5.23.: N-1 plots for the common CRs [3]. All processes are scaled to the collected integrated luminosity of 36.1 fb^{-1}. The ratio of the observed data to the total SM expectation is given. The normalisations of the processes are taken from the final fit result, the $t\bar{t}$ process has a normalisation of 1. The hatched band indicates the total statistical and systematic uncertainty on the SM-background estimation.

Table 5.18.: Observations in the SRs with the final background estimation from the simultaneous fit.

	SR LH	SR HH
Observed events	3	2
Total background	2.2 ± 0.6	1.9 ± 1.0
fake $\tau_{\text{had}} + e/\mu$	1.4 ± 0.5	—
$t\bar{t}$ with fake τ_{had}	—	$0.6 \pm {}^{0.7}_{0.6}$
$t\bar{t}$ with real τ_{had}	0.22 ± 0.12	$0.28 \pm {}^{0.30}_{0.28}$
$t\bar{t} + V$	0.25 ± 0.14	0.26 ± 0.12
diboson	0.15 ± 0.11	0.28 ± 0.13
single-top	$0.10 \pm {}^{0.24}_{0.10}$	0.13 ± 0.11
V+jets	0.033 ± 0.011	0.26 ± 0.06
others	0.082 ± 0.020	0.09 ± 0.04
signal	3.3 ± 0.7	4.7 ± 1.2
($m(\tilde{t}_1) = 1100$ GeV, $m(\tilde{\tau}_1) = 590$ GeV)		

ing distributions are shown in Figure 5.21 (c) for the same-sign VR and Figure 5.21 (d) for the opposite-sign VR in the lep-had selection. In the had-had selection, the VR for the real τ_{had} component is shown in Figure 5.22 (c), and the VR for the fake τ_{had} component is shown in Figure 5.22 (d).

Finally, the observed and expected event yields in the SRs are shown in Table 5.18. There is no significant excess over the SM expectation, therefore limits on the signal expectations will be set. Figure 5.24 shows kinematical distributions of $E_{\text{T}}^{\text{miss}}$ and $m_{\text{T2}}(\ell, \tau)$ in the SRs with the final background process estimation.

5.9.2. Exclusion Limits

The lack of an excess in both of the SRs is translated into exclusion limits on the signal model. As discussed in Section 5.8.4, the CL_s prescription is used. Figure 5.25 shows the expected and observed exclusion contours at 95 % confidence level (CL) in the $m_{\tilde{\tau}_1}$-$m_{\tilde{t}_1}$ plane from the combination of both SRs. The expected limit is given with the corresponding uncertainties. It is calculated from the expected SR yields when assuming the SM-only hypothesis. The yellow uncertainty band corresponds to the up- and down-variation of the SM expectation by $\pm 1\sigma$. The red line corresponds to the observed exclusion limit. Since the observation is slightly higher than the nominal background expectation in both channels, the observed exclusion is weaker than the expected one. The uncertainty band for the observed limit has a width that is different from the expected one, due to its inherently different origin. The uncertainty on the observed exclusion limit is obtained by varying the signal expectation up and down by 1σ of the theory uncertainty of the expected cross section. For reference, the results from previous analyses, as discussed in Section 2.3.2, are included.

The observed limit on the simplified signal reaches up to 1.16 TeV for $m_{\tilde{t}_1}$ and up to

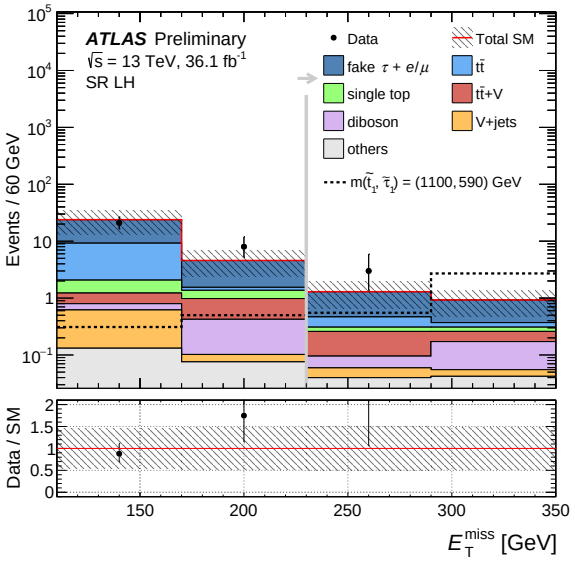

(a) $E_{\mathrm{T}}^{\mathrm{miss}}$ distribution in the lep-had SR.

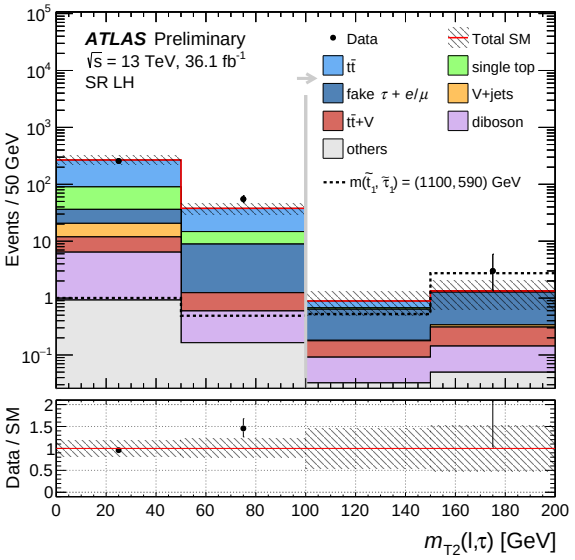

(b) $m_{\mathrm{T2}}(\ell, \tau)$ distribution in the lep-had SR.

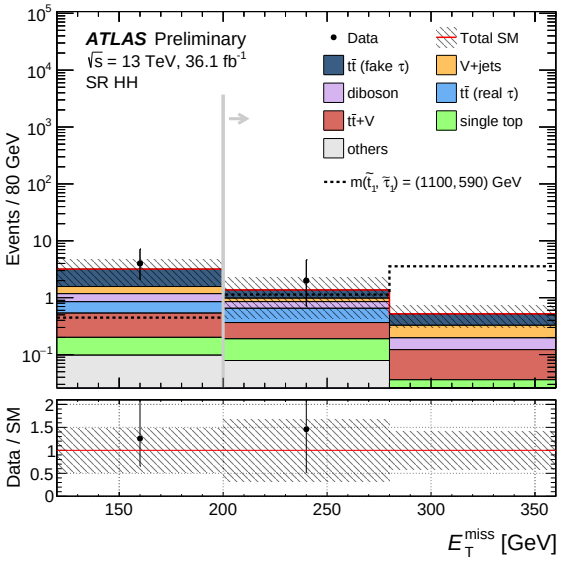

(c) $E_{\mathrm{T}}^{\mathrm{miss}}$ distribution in the had-had SR.

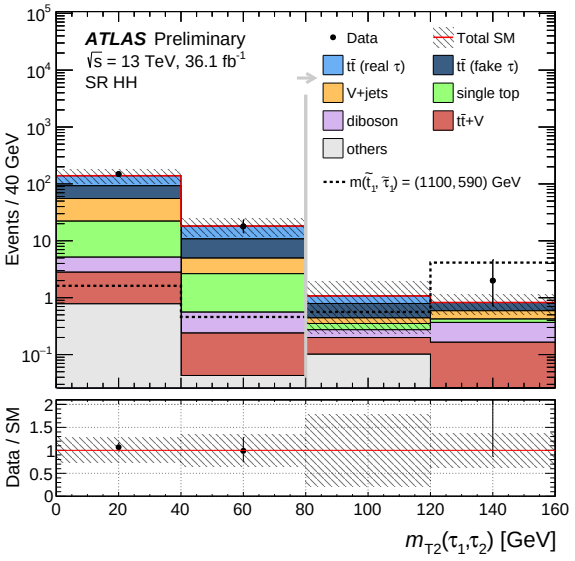

(d) $m_{\mathrm{T2}}(\tau_1, \tau_2)$ distribution in the had-had SR.

Figure 5.24.: N-1 plots for the SRs [3]. All processes are scaled to the collected integrated luminosity of 36.1 fb^{-1}. The ratio of the observed data to the total SM expectation is given. The normalisations of the processes are taken from the final fit result. Fake contributions to the lep-had selection (fake $\tau + e/\mu$) are estimated using the FFM, only the real τ_{had} component of the other SM processes is included in the other background processes. In the had-had selection, the $t\bar{t}$ process is split into events with real and fake τ_{had}. Both are separately normalized in dedicated CRs. The hatched band indicates the total statistical and systematic uncertainty on the SM-background estimation.

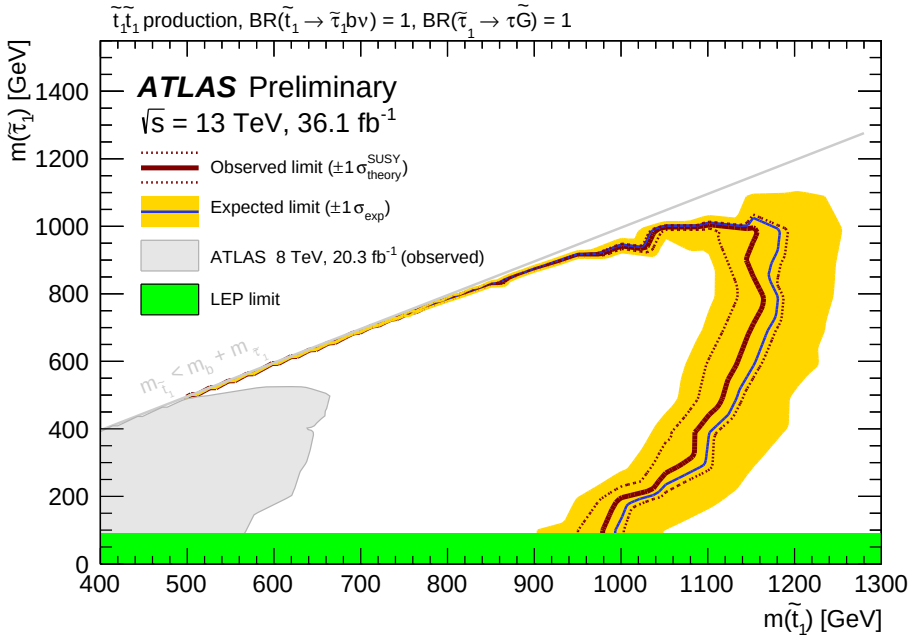

Figure 5.25.: Expected and observed exclusion at 95 % CL with 36.1 fb^{-1} of data at 13 TeV of centre-of-mass energy [3]. The calculation of the uncertainty bands is described in the text. Previous results of the LEP experiments and the analysis at a centre-of-mass energy of 8 TeV are included.

1.00 TeV for $m_{\tilde{\tau}_1}$. The CL$_s$ calculation uses the asymptotic approximation as described in Section 5.8.2. When sampling the distributions of the test statistics with pseudo-experiments, the observed limits are reduced with respect to the asymptotic calculation by up to 40 GeV in $m_{\tilde{t}_1}$.

Figure 5.26 shows the individual expected and observed exclusion limits for the lep-had and the had-had SRs. The individual limits are obtained by using only the respective SR in the simultaneous fit. As discussed throughout this thesis, the had-had SR has, due to the lower contribution from SM background processes, a higher overall sensitivity. The expected exclusion from the lep-had SR is smaller, but still improves the combined limit compared to the limit provided by the had-had SR alone. Finally, the small excess in the lep-had SR and the almost spot-on observation in the had-had SR can be seen in the difference of the expected and observed exclusion contours.

5.9.3. Model-Independent Limits

Table 5.19 summarises the model-independent limits derived from the observations in the SRs. In this context, independence of a model means to dismiss the simplified model and to assume a general signal which would give rise to additional events in the SRs. Since assuming a relation between the lep-had and had-had SRs would introduce a model dependence, both SRs are evaluated independently. Any model can be interpreted in context of these limits as long as interference with the SM is small or correctly determined.

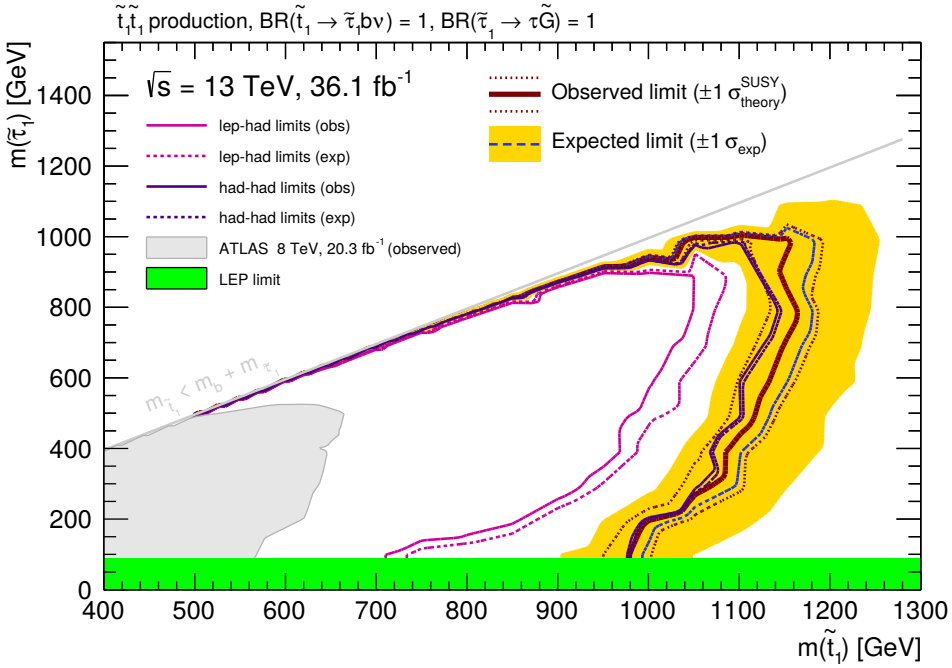

Figure 5.26.: Same plot as Figure 5.25, but with separate observed and expected limits for the lep-had (rose) and the had-had (indigo) SRs overlayed.

Table 5.19.: Model-independent limits from the two SRs. The individual columns are explained in the text (Section 5.9.3).

Signal channel	$\langle \epsilon A \sigma \rangle^{95}_{\text{obs}}$[fb]	S^{95}_{obs}	S^{95}_{exp}	$p(s=0)$ (Z)
SR LH	0.15	5.4	$4.5^{+2.6}_{-1.5}$	0.32 (0.47)
SR HH	0.13	4.7	$4.6^{+2.5}_{-1.5}$	0.48 (0.05)

First of all, the maximum number of additional events in each SR can be determined. Using the simple signal model of additional events in each SR, a scan of the signal strength parameter μ is performed, evaluating $\mathrm{CL_s}$ for each SR. From the $\mathrm{CL_s}$ scan, the expected (observed) maximum number of additional signal events S^{95}_{exp} (S^{95}_{obs}) at 95 % CL is obtained by evaluating μ at the point where $\mathrm{CL_s}$ crosses 0.05 from above. The uncertainty on the number of expected events is, as in the case of the model-dependent limits, determined by the $\pm 1\sigma$ variations of the SM background expectation. Since there is no intrinsic theory uncertainty on the signal expectation, no uncertainty is quoted.

Using the S^{95}_{obs} and the measured integrated luminosity L, a limit on the visible cross section $\langle \epsilon A \sigma \rangle^{95}_{\mathrm{obs}}$ at 95 % CL can be determined:

$$\langle \epsilon A \sigma \rangle^{95}_{\mathrm{obs}} = \frac{S^{95}_{\mathrm{obs}}}{L} \tag{5.20}$$

The visible cross section is defined as the product of the cross section of the process considered σ, the acceptance of the detector A, and the product of all reconstruction efficiencies ϵ. Only the visible cross section can be determined, since the detector acceptance and the reconstruction efficiencies typically are model-dependent. For the benchmark point at $m_{\tilde{t}_1} = 1100$ GeV and $m_{\tilde{\tau}_1} = 590$ GeV, the product $\epsilon \times A$ is $24.03\% \times 12.23\%$ for the lep-had SR and $21.38\% \times 19.82\%$ for the had-had SR.

Finally, the simple model assumption is dropped and only the incompatibility with the SM prediction is quantified. As it would be done in the case of a discovery, the p-value with the corresponding Gaussian significance $p(s = 0)$ (Z) is quoted. The p-value describes the probability to observe a fluctuation over the SM at least as extreme as the actual observation.

6. Conclusion

An analysis targeting a simplified supersymmetric signal model was presented. The implications of supersymmetric models were explained, building on an introduction of the mathematical description of the SM. The signal model assumes direct pair production of top-squark ($\tilde{t}_1$) pairs, where the $\tilde{t}_1$ always decays via a virtual chargino to a b-quark, a neutrino and a tau-slepton ($\widetilde{\tau}_1$) . The $\widetilde{\tau}_1$ finally decays to a tau lepton and a gravitino. This model has a rich final state with two b-quarks, two tau leptons and several sources of missing transverse energy. The analysis focuses on the two channels with the highest overall branching fraction, the lep-had and the had-had channel.

The dataset collected by ATLAS in the years 2015 and 2016 was used for this analysis. All relevant background processes expected from the SM were introduced and their simulation described. The reduced contribution of background events in the had-had selection was discussed.

In order to maximise the sensitivity reach, the two channels were optimised independently. The design was chosen to implement statistically independent selections, therefore both signal regions could be combined in a simultaneous fit. The sensitivity of the analysis was shown to be driven by the had-had channel, but the combination with the lep-had channel improves the sensitivity further and gives the possibility for an independent validation of the results.

A detailed background strategy was developed for both channels. All background processes with significant contributions were normalised in respective control regions and a dedicated fake-estimation strategy was employed in the lep-had channel. The contributions of the $t\bar{t}$ process, as well as the fake estimations were validated in dedicated regions. The mild excess in the opposite-sign region for the $t\bar{t}$ process with fake τ_{had} was studied. No systematic mismodelling was found and the excess not corroborated by other observations within this analysis.

The statistical evaluation of the observations with respect to the expectations was introduced and the relevant systematic uncertainties were described. Both channels consistently show an observation compatible with the SM expectation. Combined exclusion limits using the CL_s procedure were presented as contour plots in the $m_{\widetilde{\tau}_1}$–$m_{\tilde{t}_1}$ plane. The limit reaches at 95 % CL up to 1.00 TeV for $m_{\widetilde{\tau}_1}$ and up to 1.16 TeV for $m_{\tilde{t}_1}$. Model-independent limits were calculated for both channels, showing that a signal process can, at 95 % CL, at most contribute 5.4 (4.7) additional events to the lep-had (had-had) signal region to be consistent with the observation.

Limits of previous analyses, which are applicable to the signal model presented here, were introduced in Section 2.3.2. The limits are also included in the final plot of the exclusion reach (Figure 5.25). The limit from the Run 1 analysis at 8 TeV is easily surpassed due to higher production cross-section, but also due to the increased integrated luminosity and the improvements of the particle identification. The limits of the LEP experiments are interpreted independently of $m_{\tilde{t}_1}$ and are consistent with the findings

presented here.

While the interpretation of exclusion limits in the simplified model provides a tangible interpretation, the lack of observation of an excess of events in both channels has impact on other theories as well. Since the main discriminating cuts used in this analysis are $E_{\mathrm{T}}^{\mathrm{miss}}$, m_{T2}, and $p_{\mathrm{T}}(\tau_{\text{had-vis}})$ requirements, this analysis is potentially sensitive to many other signal models with b-quarks and tau leptons in the final state and can put constraints to these models.

Nevertheless, measurements from B-hadron physics deviate from the SM expectation up to almost 4σ in the case of the measurement of $\mathcal{R}(D)$ and $\mathcal{R}(D^*)$ [125]. $\mathcal{R}(X)$ describes the ratio of branching fractions $\mathcal{B}(B \to X\tau\nu_\tau)/\mathcal{B}(B \to X\ell\nu_\ell)$, suggesting to pursue dedicated searches with final states including tau leptons, because of the potential violation of the lepton-flavour universality. For example leptoquarks at the TeV scale could explain the deviations [8], especially the decay mode to a top-quark and a tau lepton gives rise to a similar final state as the simplified model discussed here and could therefore be an interesting extension to this analysis.

A future analysis, targeting the simplified signal model presented here, will be able to extend the sensitivity to higher masses. Not only is LHC planned to deliver significantly more data, but also direct improvements to the analysis would be possible. The additional dataset will allow to study the smaller cross-sections at higher $m_{\tilde{t}_1}$ with their even more pronounced kinematic distributions, but also some of the systematic uncertainties can be reduced and the data-driven background estimations improved. The use of the m_{T2} variable could be revisited, since it is known to have configurations minimising trivially to 0, leading to a small signal efficiency.

The reconciliation of astrophysical observations with laboratory experiments is still an interesting question. Within the framework of SUSY, many viable models are still not covered by current analyses. Models with higher mass scales or difficult topologies, as well as models with lightest supersymmetric particles with small mass differences could evade detection. Any of the individual approaches could provide hints to the new phenomena going beyond the SM, but which one it will be stays an open question. Therefore, the next discovery in one of these fields will most probably cause a revolution in our understanding of particle physics, which is what makes this turning point exciting.

A. Appendix

A.1. Signal-Contamination Plots

Figures A.1–A.2 show the relative signal contributions to the control and validation regions defined above. Especially in the VRs and at low $m_{\tilde{t}_1}$, high signal contaminations can arise, due to their closeness to the SRs. At low values of $m_{\tilde{t}_1}$ are mass points, which were already excluded in the analysis with Run 1 data. These points are of no concern for the analysis presented.

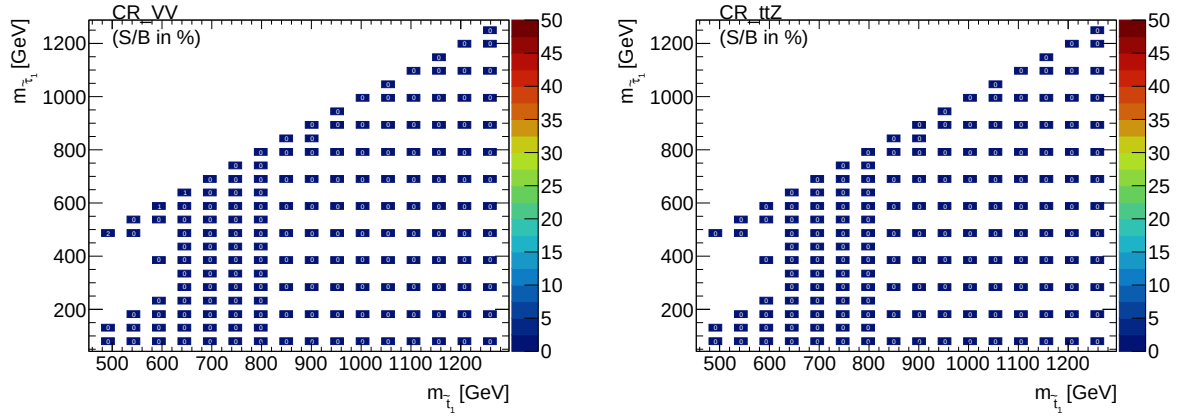

(a) CR for the VV process.

(b) CR for the $t\bar{t} + Z$ process.

Figure A.1.: Signal contamination of the common control regions. The colour scale shows the fraction of signal events with respect to the background expectation in percentages.

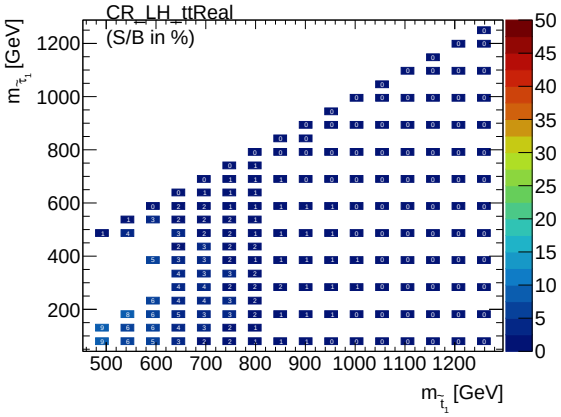

(a) CR for the $t\bar{t}$ process with real τ_{had}.

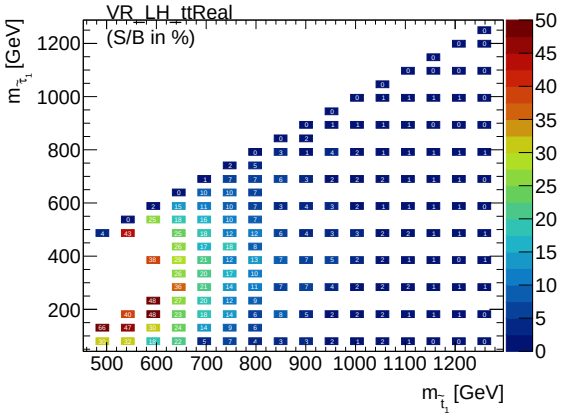

(b) VR for the $t\bar{t}$ process with real τ_{had}.

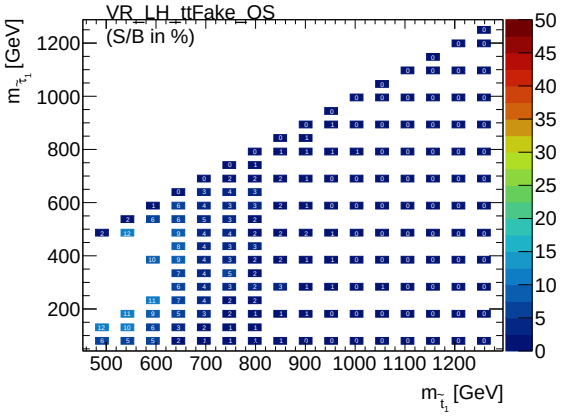

(c) VR for the $t\bar{t}$ process with fake τ_{had} and opposite-sign requirement.

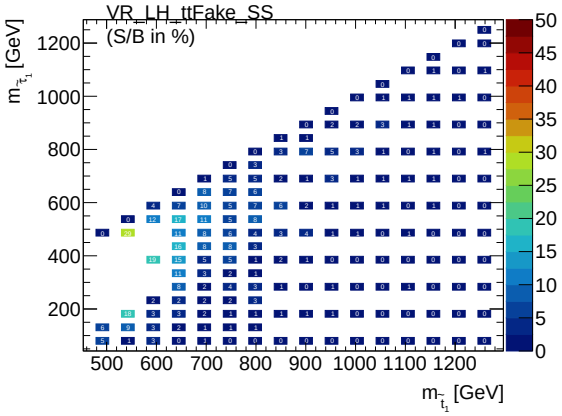

(d) VR for the $t\bar{t}$ process with fake τ_{had} and same-sign requirement.

Figure A.2.: Signal contamination in the regions of the lep-had selection. The colour scale shows the fraction of signal events with respect to the background expectation in percentages.

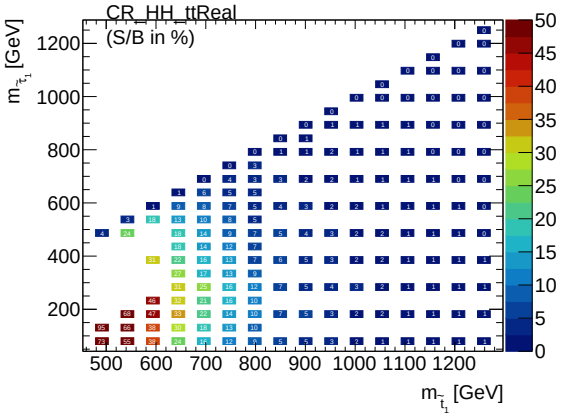

(a) CR for the $t\bar{t}$ process with real τ_{had}.

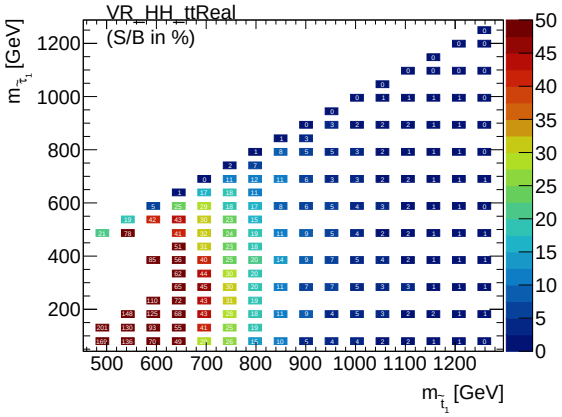

(b) VR for the $t\bar{t}$ process with real τ_{had}.

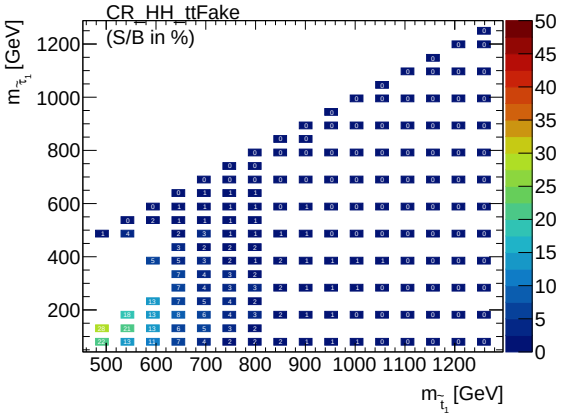

(c) CR for the $t\bar{t}$ process with fake τ_{had}.

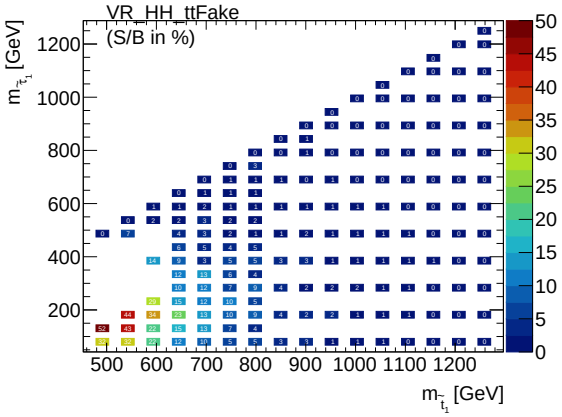

(d) VR for the $t\bar{t}$ process with fake τ_{had}.

Figure A.3.: Signal contamination in the regions of the had-had selection. The colour scale shows the fraction of signal events with respect to the background expectation in percentages.

A.2. Mt2 Examples

The two example configurations shown in Figure 5.7 were calculated from real values (using arbitrary units). The lengths and angles of the vectors shown in the graphics correspond to their values and are included explicitly in Figure A.4.

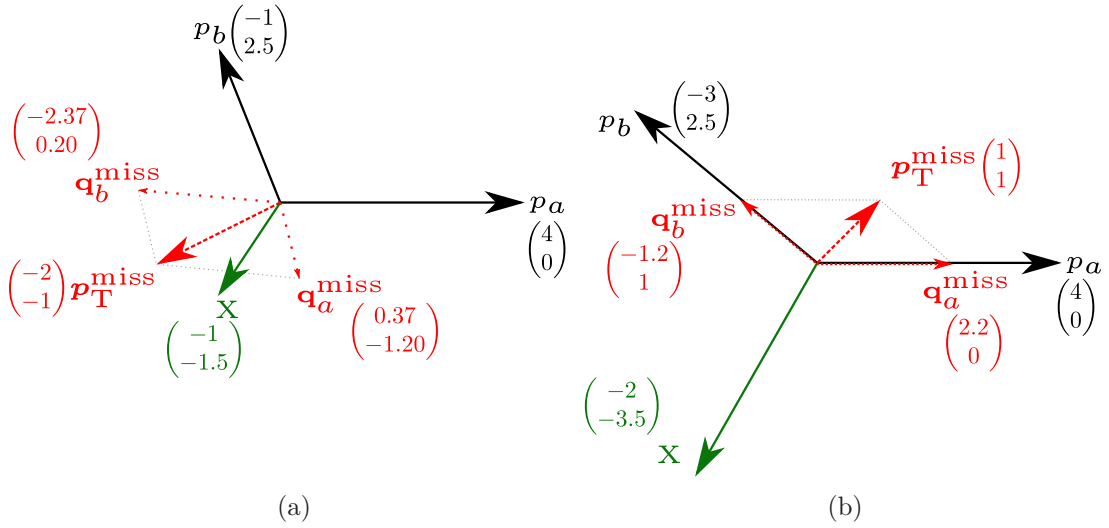

Figure A.4.: Plots shown in Figure 5.7 with values of the vectors given explicitly.

The first setup (Figure A.4 (a)) uses this set of vectors:

$$p_a = \begin{pmatrix}4\\0\end{pmatrix}, p_b = \begin{pmatrix}-1\\2.5\end{pmatrix}, \boldsymbol{p}_{\text{T}}^{\text{miss}} = \begin{pmatrix}-2\\-1\end{pmatrix}, X = \begin{pmatrix}-1\\-1.5\end{pmatrix} \tag{A.1}$$

The minimisation procedure of m_{T2} results in this splitting of $\boldsymbol{p}_{\text{T}}^{\text{miss}}$:

$$\boldsymbol{q}_a^{\text{miss}} = \begin{pmatrix}0.37\\-1.20\end{pmatrix}, \boldsymbol{q}_b^{\text{miss}} = \begin{pmatrix}-2.37\\0.20\end{pmatrix}, \tag{A.2}$$

yielding these values: $m_{\text{T}a} = m_{\text{T}b} = m_{\text{T2}} = 2.66$. Since $|p_a| + |p_b| + |\boldsymbol{p}_{\text{T}}^{\text{miss}}| \approx 6.69$, the relative contribution of m_{T2} to the effective mass $\left(\frac{m_{\text{T2}}}{|p_a|+|p_b|+|\boldsymbol{p}_{\text{T}}^{\text{miss}}|}\right)$ is about 30 %.

The values obtained for the second setup (Figure A.4 (b)) is given by:

$$p_a = \begin{pmatrix}4\\0\end{pmatrix}, p_b = \begin{pmatrix}-3\\2.5\end{pmatrix}, E_{\text{T}}^{\text{miss}} = \begin{pmatrix}1\\1\end{pmatrix}, X = \begin{pmatrix}-2\\-3.5\end{pmatrix} \tag{A.3}$$

with the $\boldsymbol{p}_{\text{T}}^{\text{miss}}$ splitting:

$$\boldsymbol{q}_a^{\text{miss}} = \begin{pmatrix}2.2\\0.00\end{pmatrix}, \boldsymbol{q}_b^{\text{miss}} = \begin{pmatrix}-1.2\\1\end{pmatrix}, \tag{A.4}$$

yielding $m_{\text{T}a} = m_{\text{T}b} = m_{\text{T2}} = 0$.

Bibliography

[1] ATLAS Collaboration. "Search for direct top squark pair production in final states with two tau leptons in pp collisions at $\sqrt{s} = 8$ TeV with the ATLAS detector". In: *Eur. Phys. J. C* 76 (2016), p. 81. DOI: 10.1140/epjc/s10052-016-3897-z. arXiv: 1509.04976 [hep-ex].

[2] ATLAS Collaboration. *Search for top-squark pair production in final states with two tau leptons, jets, and missing transverse momentum in $\sqrt{s} = 13$ TeV pp collisions with the ATLAS detector*. ATLAS-CONF-2016-048. 2016. URL: https://cds.cern.ch/record/2206130.

[3] ATLAS Collaboration. *Search for top squarks decaying to tau sleptons in pp collisions at $\sqrt{s} = 13$ TeV with the ATLAS detector*. ATLAS-CONF-2017-079. 2017. URL: https://cds.cern.ch/record/2297260.

[4] Peskin, M. and Schroeder, D. *An Introduction to Quantum Field Theory*. Westview Press, 1995.

[5] Baer, H. and Tata, X. *Weak Scale Supersymmetry*. Cambridge University Press, 2006.

[6] Peter J. Mohr, David B. Newell, and Barry N. Taylor. "CODATA recommended values of the fundamental physical constants: 2014". In: *Rev. Mod. Phys.* 88 (3 2016), p. 035009. DOI: 10.1103/RevModPhys.88.035009. URL: https://link.aps.org/doi/10.1103/RevModPhys.88.035009.

[7] Griffiths, D. *Introduction to elementary particles*. WILEY-VCH, 2008.

[8] C. Patrignani et al. "Review of Particle Physics". In: *Chin. Phys.* C40.10 (2016), p. 100001. DOI: 10.1088/1674-1137/40/10/100001.

[9] Y. Fukuda et al. "Evidence for Oscillation of Atmospheric Neutrinos". In: *Phys. Rev. Lett.* 81 (8 1998), pp. 1562–1567. DOI: 10.1103/PhysRevLett.81.1562. URL: https://link.aps.org/doi/10.1103/PhysRevLett.81.1562.

[10] Q. R. Ahmad et al. "Measurement of the Rate of $\nu_e + d \rightarrow p + p + e^-$ Interactions Produced by ^8B Solar Neutrinos at the Sudbury Neutrino Observatory". In: *Phys. Rev. Lett.* 87 (7 2001), p. 071301. DOI: 10.1103/PhysRevLett.87.071301. URL: https://link.aps.org/doi/10.1103/PhysRevLett.87.071301.

[11] Matthew Newby (Milkyway@home). "Galaxy Rotation curve". Last accessed: 2017-12-31. URL: https://milkyway.cs.rpi.edu/download/images/gal_rotation_curve.png.

[12] Douglas Clowe et al. "A Direct Empirical Proof of the Existence of Dark Matter". In: *The Astrophysical Journal Letters* 648.2 (2006), p. L109. URL: http://stacks.iop.org/1538-4357/648/i=2/a=L109.

[13] G. 't Hooft and M. Veltman. "Regularization and renormalization of gauge fields". In: *Nuclear Physics B* 44.1 (1972), pp. 189 –213. ISSN: 0550-3213. DOI: https://doi.org/10.1016/0550-3213(72)90279-9. URL: http://www.sciencedirect.com/science/article/pii/0550321372902799.

[14] *The 2004 Nobel Prize in Physics - Popular Information*. Nobel Media AB 2014. http://www.nobelprize.org/nobel_prizes/physics/laureates/2004/popular.html. Accessed: 2018-01-02.

[15] *Interview by Jessica Griggs with Peter Higgs in the New Scientist on 10. July 2012*. https://www.newscientist.com/article/dn22033-peter-higgs-boson-discovery-like-being-hit-by-a-wave/. Accessed: 2017-12-29.

[16] S. P. Martin. "a Supersymmetry Primer". In: *Perspectives On Supersymmetry. Series: Advanced Series on Directions in High Energy Physics, ISBN: 978-981-02-3553-6. WORLD SCIENTIFIC, Edited by Gordon L Kane, vol. 18, pp. 1-98* 18 (July 1998), pp. 1–98. DOI: 10.1142/9789812839657_0001. eprint: hep-ph/9709356.

[17] Pierre Binétruy. *Supersymmetry*. Oxford University Press, 2006.

[18] Drees, M., Godbole, R.M., and Roy, P. *Theory and Phenomenology of Sparticles*. World Scientific Publishing Co. Pte. Ltd., 2004.

[19] K. Abe et al. "Search for proton decay via $p \to e^+\pi^0$ and $p \to \mu^+\pi^0$ in 0.31 megaton $\cdot$ years exposure of the Super-Kamiokande water Cherenkov detector". In: *Phys. Rev. D* 95 (1 2017), p. 012004. DOI: 10.1103/PhysRevD.95.012004. URL: https://link.aps.org/doi/10.1103/PhysRevD.95.012004.

[20] Roberto Casalbuoni. "High-energy equivalence theorems in spontaneously broken gauge theories". In: *Nuclear Physics B - Proceedings Supplements* 16 (1990), pp. 577 –578. ISSN: 0920-5632. DOI: https://doi.org/10.1016/0920-5632(90)90600-Y. URL: http://www.sciencedirect.com/science/article/pii/092056329090600Y.

[21] Antonio L. Maroto and J. R. Peláez. "The equivalence theorem and the production of gravitinos after inflation". In: *Phys. Rev. D* 62 (2 2000), p. 023518. DOI: 10.1103/PhysRevD.62.023518. URL: https://link.aps.org/doi/10.1103/PhysRevD.62.023518.

[22] S. Dimopoulos and G.F. Giudice. "Naturalness constraints in supersymmetric theories with non-universal soft terms". In: *Physics Letters B* 357.4 (1995), pp. 573 –578. ISSN: 0370-2693. DOI: https://doi.org/10.1016/0370-2693(95)00961-J. URL: http://www.sciencedirect.com/science/article/pii/037026939500961J.

[23] W. Porod. "More on higher order decays of the lighter top squark". In: *Phys. Rev. D* 59 (9 1999), p. 095009. DOI: 10.1103/PhysRevD.59.095009. URL: https://link.aps.org/doi/10.1103/PhysRevD.59.095009.

[24] Wim Beenakker et al. "Supersymmetric top and bottom squark production at hadron colliders". In: *JHEP* 08.arXiv:1006.4771. CERN-PH-TH-2010-142 (2010). Comments: 29 pages, 6 figures, 098. 29 p. URL: https://cds.cern.ch/record/1274171.

[25] Michael Krämer et al. *Supersymmetry production cross sections in pp collisions at sqrts = 7 TeV*. Tech. rep. arXiv:1206.2892. CERN-PH-TH-2012-163. 2012. URL: https://cds.cern.ch/record/1456029.

[26] Christoph Borschensky et al. "Squark and gluino production cross sections in pp collisions at $\sqrt{s}$ = 13, 14, 33 and 100 TeV". In: *Eur. Phys. J. C* 74.arXiv:1407.5066. MS-TP-14-25. CERN-PH-TH-2014-137. 12 (2014). Comments: 22 pages, 16 figures. arXiv admin note: substantial text overlap with arXiv:1206.2892, 3174. 22 p. URL: https://cds.cern.ch/record/1744356.

[27] LHC SUSY Cross Section Working Group. "stop_xsec". Last accessed: 2018-01-06. URL: https://twiki.cern.ch/twiki/pub/LHCPhysics/SUSYCrossSections/stop_xsec.pdf.

[28] The LEP2 SUSY Working Group and ALEPH, DELPHI, L3, OPAL Experiments. *Combined LEP Selectron/Smuon/Stau Results, 183-208 GeV*. http://lepsusy.web.cern.ch/lepsusy/www/sleptons_summer04/slep_final.html. 2004.

[29] CMS Collaboration. "Search for electroweak production of charginos in final states with two τ leptons in *pp* collisions at $\sqrt{s}$ = 8 TeV". In: *JHEP* 04 (2017), p. 018. DOI: 10.1007/JHEP04(2017)018. arXiv: 1610.04870 [hep-ex].

[30] *Search for supersymmetry in events with tau leptons and missing transverse momentum in proton-proton collisions at sqrt(s)=13 TeV*. Tech. rep. CMS-PAS-SUS-17-002. Geneva: CERN, 2017. URL: https://cds.cern.ch/record/2297162.

[31] *Search for pair production of tau sleptons in* $\sqrt{s}$ = 13 TeV *pp collisions in the all-hadronic final state*. Tech. rep. CMS-PAS-SUS-17-003. Geneva: CERN, 2017. URL: https://cds.cern.ch/record/2273395.

[32] ATLAS Collaboration. "Search for the electroweak production of supersymmetric particles in $\sqrt{s}$ = 8 TeV *pp* collisions with the ATLAS detector". In: *Phys. Rev. D* 93 (2016), p. 052002. DOI: 10.1103/PhysRevD.93.052002. arXiv: 1509.07152 [hep-ex].

[33] Morad Aaboud et al. "Search for dark matter and other new phenomena in events with an energetic jet and large missing transverse momentum using the ATLAS detector". In: (2017). arXiv: 1711.03301 [hep-ex].

[34] ATLAS Collaboration. "Search for a scalar partner of the top quark in the jets plus missing transverse momentum final state at $\sqrt{s}$ = 13 TeV with the ATLAS detector". In: (2017). arXiv: 1709.04183 [hep-ex].

[35] ATLAS Collaboration. "Search for supersymmetry in events with *b*-tagged jets and missing transverse momentum in *pp* collisions at $\sqrt{s}$ = 13 TeV with the ATLAS detector". In: *JHEP* 11 (2017), p. 195. DOI: 10.1007/JHEP11(2017)195. arXiv: 1708.09266 [hep-ex].

[36] ATLAS Collaboration. "Search for direct top squark pair production in final states with two leptons in $\sqrt{s}$ = 13 TeV *pp* collisions with the ATLAS detector". In: (2017). arXiv: 1708.03247 [hep-ex].

[37] CMS Collaboration. *Search for direct production of supersymmetric partners of the top quark in the all-jets final state in proton-proton collisions at* $\sqrt{s}$ = *13 TeV*. Tech. rep. CMS-SUS-16-049. CMS-SUS-16-049-003. Submitted to JHEP. All figures and tables can be found at http://cms-results.web.cern.ch/cms-results/public-results/publications/SUS-16-049. Geneva: CERN, 2017. URL: https://cds.cern.ch/record/2274031.

[38] CMS Collaboration. "Search for top squark pair production in pp collisions at $\sqrt{s}$ = 13 TeV using single lepton events. Search for top squark pair production in pp collisions at sqrt(s)=13 TeV using single lepton events". In: *JHEP* 10.CMS-SUS-16-051. CMS-SUS-16-051-004 (2017). Replaced with the published version. Added the journal reference and DOI. All the figures and tables, including additional supplemental figures and tables, can be found at http://cms-results.web.cern.ch/cms-results/public-results/publications/SUS-16-051 (CMS Public Pages), 019. 40 p. URL: https://cds.cern.ch/record/2269047.

[39] CMS Collaboration. *Search for top squarks and dark matter particles in opposite-charge dilepton final states at $\sqrt{s}$ = 13 TeV. Search for top squarks and dark matter particles in opposite-charge dilepton final states at $\sqrt{s}$ = 13 TeV*. Tech. rep. CMS-SUS-17-001. CMS-SUS-17-001-003. Submitted to Phys. Rev. D. All figures and tables can be found at http://cms-results.web.cern.ch/cms-results/public-results/publications/SUS-17-001/ (CMS Public Pages). Geneva: CERN, 2017. URL: https://cds.cern.ch/record/2291416.

[40] "LHC Guide". 2017. URL: https://cds.cern.ch/record/2255762.

[41] Lyndon Evans and Philip Bryant. "LHC Machine". In: *JINST* 3 (2008), S08001. DOI: 10.1088/1748-0221/3/08/S08001.

[42] Esma Anais Mobs. "The CERN accelerator complex. Complexe des accélérateurs du CERN". In: (2016). General Photo. URL: https://cds.cern.ch/record/2225847.

[43] H Damerau et al. "RF Manipulations for Higher Brightness LHC-Type Beams". In: CERN-ACC-2013-0210 (2013), 3 p. URL: https://cds.cern.ch/record/1595719.

[44] Richard D. Ball et al. "Parton distributions for the LHC Run II". In: *JHEP* 04 (2015), p. 040. DOI: 10.1007/JHEP04(2015)040. arXiv: 1410.8849 [hep-ph].

[45] *The ATLAS collaboration*. https://atlas.web.cern.ch/Atlas/GROUPS/PHYSICS/CombinedSummaryPlots/SM/. Accessed: 2017-10-25.

[46] Stefano Frixione et al. "Single-top hadroproduction in association with a W boson". In: *Journal of High Energy Physics* 2008.07 (2008), p. 029. URL: http://stacks.iop.org/1126-6708/2008/i=07/a=029.

[47] ATLAS Collaboration. *Simulation of top-quark production for the ATLAS experiment at $\sqrt{s}$ = 13 TeV*. ATL-PHYS-PUB-2016-004. 2016. URL: https://cds.cern.ch/record/2120417.

[48] ATLAS Collaboration. *Performance of the ATLAS Inner Detector Track and Vertex Reconstruction in High Pile-Up LHC Environment*. ATLAS-CONF-2012-042. 2012. URL: https://cds.cern.ch/record/1435196.

[49] *The ATLAS collaboration*. https://twiki.cern.ch/twiki/bin/view/AtlasPublic/LuminosityPublicResultsRun2. Accessed: 2017-10-26.

[50] ATLAS Collaboration. "Luminosity determination in *pp* collisions at $\sqrt{s} = 8$ TeV using the ATLAS detector at the LHC". In: *Eur. Phys. J. C* 76 (2016), p. 653. DOI: 10.1140/epjc/s10052-016-4466-1. arXiv: 1608.03953 [hep-ex].

[51] ATLAS Collaboration. "The ATLAS Experiment at the CERN Large Hadron Collider". In: *JINST* 3 (2008), S08003. DOI: 10.1088/1748-0221/3/08/S08003.

[52] Joao Pequenao. "Computer generated image of the whole ATLAS detector". 2008. URL: http://cds.cern.ch/record/1095924.

[53] ATLAS Collaboration. *Track Reconstruction Performance of the ATLAS Inner Detector at $\sqrt{s}$ = 13 TeV*. ATL-PHYS-PUB-2015-018. 2015. URL: https://cds.cern.ch/record/2037683.

[54] M Capeans et al. *ATLAS Insertable B-Layer Technical Design Report*. Tech. rep. CERN-LHCC-2010-013. ATLAS-TDR-19. 2010. URL: https://cds.cern.ch/record/1291633.

[55] Boris Dolgoshein. "Transition radiation detectors". In: *Nuclear Instruments and Methods in Physics Research Section A: Accelerators, Spectrometers, Detectors and Associated Equipment* 326.3 (1993), pp. 434 –469. ISSN: 0168-9002. DOI: https://doi.org/10.1016/0168-9002(93)90846-A. URL: http://www.sciencedirect.com/science/article/pii/016890029390846A.

[56] ATLAS Collaboration. "Performance of the ATLAS muon trigger in *pp* collisions at $\sqrt{s} = 8$ TeV". In: *Eur. Phys. J. C* 75 (2015), p. 120. DOI: 10.1140/epjc/s10052-015-3325-9. arXiv: 1408.3179 [hep-ex].

[57] ATLAS Collaboration. *The ATLAS Tau Trigger in Run 2*. ATLAS-CONF-2017-061. 2017. URL: https://cds.cern.ch/record/2274201.

[58] R Achenbach et al. "The ATLAS Level-1 Calorimeter Trigger". In: *Journal of Instrumentation* 3.03 (2008), P03001. URL: http://stacks.iop.org/1748-0221/3/i=03/a=P03001.

[59] Morad Aaboud et al. "Performance of the ATLAS Trigger System in 2015". In: *Eur. Phys. J.* C77.5 (2017), p. 317. DOI: 10.1140/epjc/s10052-017-4852-3. arXiv: 1611.09661 [hep-ex].

[60] ATLAS Collaboration. *Vertex Reconstruction Performance of the ATLAS Detector at$\sqrt{s}$ = 13 TeV*. ATL-PHYS-PUB-2015-026. 2015. URL: https://cds.cern.ch/record/2037717.

[61] ATLAS Collaboration. *Performance of primary vertex reconstruction in proton–proton collisions at $\sqrt{s}$ = 7 TeV in the ATLAS experiment*. ATLAS-CONF-2010-069. 2010. URL: https://cds.cern.ch/record/1281344.

[62] Matteo Cacciari, Gavin P. Salam, and Gregory Soyez. "The anti-k_t jet clustering algorithm". In: *JHEP* 04 (2008), p. 063. DOI: 10.1088/1126-6708/2008/04/063. arXiv: 0802.1189 [hep-ph].

[63] ATLAS Collaboration. *Jet energy scale and its systematic uncertainty in proton–proton collisions at $\sqrt{s} = 7$ TeV with ATLAS 2011 data*. ATLAS-CONF-2013-004. 2013. URL: https://cds.cern.ch/record/1509552.

[64] Matteo Cacciari, Gavin P. Salam, and Gregory Soyez. "The Catchment Area of Jets". In: *JHEP* 04 (2008), p. 005. DOI: 10.1088/1126-6708/2008/04/005. arXiv: 0802.1188 [hep-ph].

[65] ATLAS Collaboration. *Properties of jets and inputs to jet reconstruction and calibration with the ATLAS detector using proton–proton collisions at $\sqrt{s} = 13$ TeV*. ATL-PHYS-PUB-2015-036. 2015. URL: https://cds.cern.ch/record/2044564.

[66] ATLAS Collaboration. *Jet Calibration and Systematic Uncertainties for Jets Reconstructed in the ATLAS Detector at $\sqrt{s} = 13$ TeV*. ATL-PHYS-PUB-2015-015. 2015. URL: https://cds.cern.ch/record/2037613.

[67] ATLAS Collaboration. *Jet global sequential corrections with the ATLAS detector in proton–proton collisions at $\sqrt{s} = 8$ TeV*. ATLAS-CONF-2015-002. 2015. URL: https://cds.cern.ch/record/2001682.

[68] ATLAS Collaboration. *Reconstruction, Energy Calibration, and Identification of Hadronically Decaying Tau Leptons in the ATLAS Experiment for Run-2 of the LHC*. ATL-PHYS-PUB-2015-045. 2015. URL: https://atlas.web.cern.ch/Atlas/GROUPS/PHYSICS/PUBNOTES/ATL-PHYS-PUB-2015-045.

[69] ATLAS Collaboration. "Jet energy measurement and its systematic uncertainty in proton–proton collisions at $\sqrt{s} = 7$ TeV with the ATLAS detector". In: *Eur. Phys. J. C* 75 (2015), p. 17. DOI: 10.1140/epjc/s10052-014-3190-y. arXiv: 1406.0076 [hep-ex].

[70] ATLAS Collaboration. *Photon identification in 2015 ATLAS data*. ATL-PHYS-PUB-2016-014. 2016. URL: https://cds.cern.ch/record/2203125.

[71] ATLAS Collaboration. *Selection of jets produced in 13 TeV proton–proton collisions with the ATLAS detector*. ATLAS-CONF-2015-029. 2015. URL: https://cds.cern.ch/record/2037702.

[72] ATLAS Collaboration. "The ATLAS Simulation Infrastructure". In: *Eur. Phys. J. C* 70 (2010), p. 823. DOI: 10.1140/epjc/s10052-010-1429-9. arXiv: 1005.4568 [physics.ins-det].

[73] S. Agostinelli et al. "GEANT4: A simulation toolkit". In: *Nucl. Instrum. Meth. A* 506 (2003), p. 250. DOI: 10.1016/S0168-9002(03)01368-8.

[74] ATLAS Collaboration. *The simulation principle and performance of the ATLAS fast calorimeter simulation FastCaloSim*. ATL-PHYS-PUB-2010-013. 2010. URL: https://cds.cern.ch/record/1300517.

[75] A. D. Martin et al. "Parton distributions for the LHC". In: *The European Physical Journal C* 63.2 (2009), pp. 189–285. ISSN: 1434-6052. DOI: 10.1140/epjc/s10052-009-1072-5. URL: https://doi.org/10.1140/epjc/s10052-009-1072-5.

[76] ATLAS Collaboration. *Summary of ATLAS Pythia 8 tunes*. ATL-PHYS-PUB-2012-003. 2012. URL: https://cds.cern.ch/record/1474107.

[77] M. Aaboud et al. "Measurement of the Inelastic Proton-Proton Cross Section at $\sqrt{s} =$ 13âĂŁâĂŁTeV with the ATLAS Detector at the LHC". In: *Phys. Rev. Lett.* 117.18 (2016), p. 182002. DOI: 10.1103/PhysRevLett.117.182002. arXiv: 1606.02625 [hep-ex].

[78] J. Alwall et al. "The automated computation of tree-level and next-to-leading order differential cross sections, and their matching to parton shower simulations". In: *Journal of High Energy Physics* 2014.7 (2014), p. 79. ISSN: 1029-8479. DOI: 10.1007/JHEP07(2014)079. URL: https://doi.org/10.1007/JHEP07(2014)079.

[79] Richard D. Ball et al. “Parton distributions with LHC data”. In: *Nuclear Physics B* 867.2 (2013), pp. 244 –289. ISSN: 0550-3213. DOI: https://doi.org/10.1016/j.nuclphysb.2012.10.003. URL: http://www.sciencedirect.com/science/article/pii/S0550321312005500.

[80] TorbjÃűrn SjÃűstrand, Stephen Mrenna, and Peter Skands. “A brief introduction to PYTHIA 8.1”. In: *Computer Physics Communications* 178.11 (2008), pp. 852 –867. ISSN: 0010-4655. DOI: https://doi.org/10.1016/j.cpc.2008.01.036. URL: http://www.sciencedirect.com/science/article/pii/S0010465508000441.

[81] TorbjÃűrn SjÃűstrand et al. “An introduction to PYTHIA 8.2”. In: *Computer Physics Communications* 191.Supplement C (2015), pp. 159 –177. ISSN: 0010-4655. DOI: https://doi.org/10.1016/j.cpc.2015.01.024. URL: http://www.sciencedirect.com/science/article/pii/S0010465515000442.

[82] ATLAS Collaboration. *ATLAS Pythia 8 tunes to 7 TeV data*. ATL-PHYS-PUB-2014-021. 2014. URL: https://cds.cern.ch/record/1966419.

[83] Simone Alioli et al. “A general framework for implementing NLO calculations in shower Monte Carlo programs: the POWHEG BOX”. In: *Journal of High Energy Physics* 2010.6 (2010), p. 43. ISSN: 1029-8479. DOI: 10.1007/JHEP06(2010)043. URL: https://doi.org/10.1007/JHEP06(2010)043.

[84] Hung-Liang Lai et al. “New parton distributions for collider physics”. In: *Phys. Rev. D* 82 (7 2010), p. 074024. DOI: 10.1103/PhysRevD.82.074024. URL: https://link.aps.org/doi/10.1103/PhysRevD.82.074024.

[85] TorbjÃűrn SjÃűstrand, Stephen Mrenna, and Peter Skands. “PYTHIA 6.4 physics and manual”. In: *Journal of High Energy Physics* 2006.05 (2006), p. 026. URL: http://stacks.iop.org/1126-6708/2006/i=05/a=026.

[86] Jonathan Pumplin et al. “New Generation of Parton Distributions with Uncertainties from Global QCD Analysis”. In: *Journal of High Energy Physics* 2002.07 (2002), p. 012. URL: http://stacks.iop.org/1126-6708/2002/i=07/a=012.

[87] Peter Z. Skands. “Tuning Monte Carlo generators: The Perugia tunes”. In: *Phys. Rev. D* 82 (7 2010), p. 074018. DOI: 10.1103/PhysRevD.82.074018. URL: https://link.aps.org/doi/10.1103/PhysRevD.82.074018.

[88] Manuel Bähr et al. “Herwig++ physics and manual”. In: *The European Physical Journal C* 58.4 (2008), pp. 639–707. ISSN: 1434-6052. DOI: 10.1140/epjc/s10052-008-0798-9. URL: https://doi.org/10.1140/epjc/s10052-008-0798-9.

[89] J. Bellm et al. “Herwig++ 2.7 Release Note”. In: (2013). arXiv: 1310.6877 [hep-ph].

[90] Stefan Gieseke, Christian Röhr, and Andrzej Siódmok. “Colour reconnections in Herwig++”. In: *The European Physical Journal C* 72.11 (2012), p. 2225. ISSN: 1434-6052. DOI: 10.1140/epjc/s10052-012-2225-5. URL: https://doi.org/10.1140/epjc/s10052-012-2225-5.

[91] Richard D. Ball et al. “Parton distributions for the LHC run II”. In: *Journal of High Energy Physics* 2015.4 (2015), p. 40. ISSN: 1029-8479. DOI: 10.1007/JHEP04(2015)040. URL: https://doi.org/10.1007/JHEP04(2015)040.

[92] ATLAS Collaboration. *Modelling of the $t\bar{t}H$ and $t\bar{t}V(V = W, Z)$ processes for $\sqrt{s} =$ 13 TeV ATLAS analyses*. ATL-PHYS-PUB-2016-005. 2016. URL: https://cds.cern.ch/record/2120826.

[93] David J. Lange. "The EvtGen particle decay simulation package". In: *Nuclear Instruments and Methods in Physics Research Section A: Accelerators, Spectrometers, Detectors and Associated Equipment* 462.1 (2001). BEAUTY2000, Proceedings of the 7th Int. Conf. on B-Physics at Hadron Machines, pp. 152 –155. ISSN: 0168-9002. DOI: https://doi.org/10.1016/S0168-9002(01)00089-4. URL: http://www.sciencedirect.com/science/article/pii/S0168900201000894.

[94] T. Gleisberg et al. "Event generation with SHERPA 1.1". In: *Journal of High Energy Physics* 2009.02 (2009), p. 007. URL: http://stacks.iop.org/1126-6708/2009/i=02/a=007.

[95] S. Schumann and F. Krauss. "A parton shower algorithm based on Catani-Seymour dipole factorisation". In: *Journal of High Energy Physics* 2008.03 (2008), p. 038. URL: http://stacks.iop.org/1126-6708/2008/i=03/a=038.

[96] ATLAS Collaboration. *Monte Carlo Generators for the Production of a W or Z/γ^* Boson in Association with Jets at ATLAS in Run 2*. ATL-PHYS-PUB-2016-003. 2016. URL: https://cds.cern.ch/record/2120133.

[97] ATLAS Collaboration. *Multi-boson simulation for 13 TeV ATLAS analyses*. ATL-PHYS-PUB-2016-002. 2016. URL: https://cds.cern.ch/record/2119986.

[98] ATLAS Collaboration. *Electron efficiency measurements with the ATLAS detector using the 2015 LHC proton–proton collision data*. ATLAS-CONF-2016-024. 2016. URL: https://cds.cern.ch/record/2157687.

[99] ATLAS Collaboration. "Electron and photon energy calibration with the ATLAS detector using LHC Run 1 data". In: *Eur. Phys. J. C* 74 (2014), p. 3071. DOI: 10.1140/epjc/s10052-014-3071-4. arXiv: 1407.5063 [hep-ex].

[100] ATLAS Collaboration. *Electron and photon energy calibration with the ATLAS detector using data collected in 2015 at $\sqrt{s} = 13$ TeV*. ATL-PHYS-PUB-2016-015. 2016. URL: https://cds.cern.ch/record/2203514.

[101] ATLAS Collaboration. "Muon reconstruction performance of the ATLAS detector in proton–proton collision data at $\sqrt{s} = 13$ TeV". In: *Eur. Phys. J. C* 76 (2016), p. 292. DOI: 10.1140/epjc/s10052-016-4120-y. arXiv: 1603.05598 [hep-ex].

[102] ATLAS collaboration. *ATLAS Muon Combined Performance with the full 2016 dataset*. https://atlas.web.cern.ch/Atlas/GROUPS/PHYSICS/PLOTS/MUON-2017-001/index.html. 2017.

[103] ATLAS Collaboration. *Tagging and suppression of pileup jets with the ATLAS detector*. ATLAS-CONF-2014-018. 2014. URL: https://cds.cern.ch/record/1700870.

[104] ATLAS Collaboration. *Optimisation of the ATLAS b-tagging performance for the 2016 LHC Run*. ATL-PHYS-PUB-2016-012. 2016. URL: https://cds.cern.ch/record/2160731.

[105] ATLAS Collaboration. *Commissioning of the ATLAS high performance b-tagging algorithms in the 7 TeV collision data*. ATLAS-CONF-2011-102. 2011. URL: https://cds.cern.ch/record/1369219.

[106] Michela Paganini. *Machine Learning Algorithms for b-Jet Tagging at the ATLAS Experiment*. Tech. rep. ATL-PHYS-PROC-2017-211. Geneva: CERN, 2017. URL: https://cds.cern.ch/record/2289214.

[107] ATLAS Collaboration. *Expected performance of the ATLAS b-tagging algorithms in Run-2*. ATL-PHYS-PUB-2015-022. 2015. URL: https://cds.cern.ch/record/2037697.

[108] G Piacquadio and C Weiser. "A new inclusive secondary vertex algorithm for b-jet tagging in ATLAS". In: *Journal of Physics: Conference Series* 119.3 (2008), p. 032032. URL: http://stacks.iop.org/1742-6596/119/i=3/a=032032.

[109] ATLAS Collaboration. *Expected performance of missing transverse momentum reconstruction for the ATLAS detector at* $\sqrt{s} = 13$ *TeV*. ATL-PHYS-PUB-2015-023. 2015. URL: https://cds.cern.ch/record/2037700.

[110] G. Arnison et al. "Further evidence for charged intermediate vector bosons at the SPS collider". In: *Physics Letters B* 129.3 (1983), pp. 273 –282. ISSN: 0370-2693. DOI: https://doi.org/10.1016/0370-2693(83)90860-2. URL: http://www.sciencedirect.com/science/article/pii/0370269383908602.

[111] C. G. Lester and D. J. Summers. "Measuring masses of semiinvisibly decaying particles pair produced at hadron colliders". In: *Phys. Lett.* B463 (1999), pp. 99–103. DOI: 10.1016/S0370-2693(99)00945-4. arXiv: hep-ph/9906349 [hep-ph].

[112] Christopher G. Lester and Benjamin Nachman. "Bisection-based asymmetric M T2 computation: a higher precision calculator than existing symmetric methods". In: *Journal of High Energy Physics* 2015.3 (2015), p. 100. ISSN: 1029-8479. DOI: 10.1007/JHEP03(2015)100. URL: https://doi.org/10.1007/JHEP03(2015)100.

[113] *ATLAS tile calorimeter: Technical Design Report*. Technical Design Report ATLAS. Geneva: CERN, 1996. URL: https://cds.cern.ch/record/331062.

[114] ATLAS Collaboration. "Performance of the ATLAS Trigger System in 2015". In: *Eur. Phys. J. C* 77 (2017), p. 317. DOI: 10.1140/epjc/s10052-017-4852-3. arXiv: 1611.09661 [hep-ex].

[115] M. Holzbock. "New elements to extend the search for supersymmetric scalar top quarks with the ATLAS detector in LHC Run 2". 2016. URL: http://www.etp.physik.uni-muenchen.de/publications/theses/download/master_mholzbock.pdf. Unpublished master's thesis.

[116] F. Krieter. "Search for Scalar Top Quarks in Final States with Two Hadronically Decaying Tau Leptons". 2017. URL: http://www.etp.physik.uni-muenchen.de/publications/theses/download/master_fkrieter.pdf. Unpublished master's thesis.

[117] L. Moneta et al. "The RooStats project". In: *Proceedings of the 13th International Workshop on Advanced Computing and Analysis Techniques in Physics Research. February 22-27, 2010, Jaipur, India*. 2010, p. 57. arXiv: 1009.1003 [physics.data-an].

[118] ATLAS Collaboration. *Data-driven determination of the energy scale and resolution of jets reconstructed in the ATLAS calorimeters using dijet and multijet events at* $\sqrt{s} =$ 8 *TeV*. ATLAS-CONF-2015-017. 2015. URL: https://cds.cern.ch/record/2008678.

[119] ATLAS Collaboration. *Calibration of b-tagging using dileptonic top pair events in a combinatorial likelihood approach with the ATLAS experiment*. ATLAS-CONF-2014-004. 2014. URL: https://cds.cern.ch/record/1664335.

[120] ATLAS Collaboration. *Calibration of the performance of b-tagging for c and light-flavour jets in the 2012 ATLAS data*. ATLAS-CONF-2014-046. 2014. URL: https://cds.cern.ch/record/1741020.

[121] M. Baak et al. "HistFitter software framework for statistical data analysis". In: *Eur. Phys. J.* C75 (2015), p. 153. DOI: 10.1140/epjc/s10052-015-3327-7. arXiv: 1410.1280 [hep-ex].

[122] Kyle Cranmer et al. *HistFactory: A tool for creating statistical models for use with RooFit and RooStats*. Tech. rep. CERN-OPEN-2012-016. New York: New York U., 2012. URL: https://cds.cern.ch/record/1456844.

[123] Glen Cowan et al. "Asymptotic formulae for likelihood-based tests of new physics". In: *Eur. Phys. J.* C71 (2011). [Erratum: Eur. Phys. J.C73,2501(2013)], p. 1554. DOI: 10.1140/epjc/s10052-011-1554-0,10.1140/epjc/s10052-013-2501-z. arXiv: 1007.1727v3 [physics.data-an].

[124] A L Read. "Presentation of search results: the CL_s technique". In: *Journal of Physics G: Nuclear and Particle Physics* 28.10 (2002), p. 2693. URL: http://stacks.iop.org/0954-3899/28/i=10/a=313.

[125] Y. Amhis et al. "Averages of b-hadron, c-hadron, and τ-lepton properties as of summer 2016". In: *Eur. Phys. J.* C77.12 (2017), p. 895. DOI: 10.1140/epjc/s10052-017-5058-4. arXiv: 1612.07233 [hep-ex].

Danksagung

Am Ende dieser Arbeit möchte ich die Gelegenheit nutzen allen den herzlichsten Dank auszusprechen, die mich bei der Erstellung dieser Arbeit unterstützt haben. Insbesondere danke ich herzlich

- Prof. Dr. Dorothee Schaile für die Möglichkeit an ihrem Lehrstuhl an diesen spannenden Forschungsprojekten teilzunehmen und die Promotion durchzuführen. Vielen Dank auch für die Korrektur der Arbeit und die Erstellung des Erstgutachtens.
- Prof. Dr. Thomas Kuhr für die Erstellung des Zweitgutachtens.
- Prof. Dr. Gerhard Buchalla, Prof. Dr. Martin Fässler, Prof. Dr. Achim Weiß und Dr. Jeannine Wagner-Kuhr für die Bereitschaft im Rahmen der Promotionskommission an der Erlangung meines Doktorgrades mitzuwirken.
- Dr. Alexander Mann für die Betreuung und das Korrekturlesen der Arbeit, aber auch dafür dass er mir mit viel Geduld geholfen hat das nötige Handwerkszeug für Teilchenphysikanalysen zu erlernen und stets bereit war mir bei der Beantwortung meiner detaillierten Fragen zu helfen.
- dem gesamtem Stop-Stau Team für die großartige Zusammenarbeit und die tolle, stets unterstützende Arbeitsatmosphäre.

This list is by no means exhaustive and there are many people who supported me in various ways.[1] From inspiring talks and helpful discussions to just helping me from time to time to take the mind off and to get a different point of view on my problems. Thanks to everyone for this great and memorable time!

- Thanks to all of my friends, who were there when I needed them.
- Zuletzt gilt der Dank meiner Familie, auf deren Rückhalt ich stets vertrauen konnte.

[1] The theory part of this thesis would not have been possible without the generous gift of a coffee machine! ;)